RAdar para Detection and Avoidance em Veículos Aéreos Não Tripulados

RADAVANT
E6.7
SCIENTIFIC CONTRIBUTIONS OF THE RADAVANT PROJECT (EN)
CONTRIBUTOS CIENTÍFICOS DO PROJETO RADAVANT (PT)

Contractual Date of Delivery:	31/Dez/2020
Actual Date of Delivery:	31/Dez/2020
Editor:	João M. Gil (TWEVO)
Authors:	João M. Gil (TWEVO), Carlos Ribeiro (TWEVO)
Internal reviewers:	Carlos Ribeiro (TWEVO) João Reis, Rafael Caldeirinha (IT)
Workpackage (EN)/Atividade (PT):	6
Security:	PU
Version:	1.0
Total number of pages:	54

SUMMARY (EN):

This Deliverable lists the scientific contributions related to the work developed in the RADAVANT project. Work on the radar processing blocks and the radar antennas has been published and disseminated in several important scientific, international and national, journal and conference papers.

SUMÁRIO (PT):

Este Entregável lista os contributos científicos relativos ao trabalho desenvolvido no projeto RADAVANT. O trabalho relativo aos blocos de processamento de radar e às antenas de radar foi publicado e disseminado em várias revistas científicas e conferências, internacionais e nacionais, importantes.

Keyword list: UAV, Drones, Radar, Scientific, Communication, Dissemination

Cofinanciado por:

CENTRO 2020 PORTUGAL 2020 UNIÃO EUROPEIA Fundo Europeu de Desenvolvimento Regional

The RADAVANT project is funded under Research and Technological Development Incentive Scheme - CO-PROMOTION | Centro2020 | P2020 | European Regional Development Funds.

Table of Contents

List of Acronyms

APC	Antennas and Propagation Conference
APS	Antennas & Propagation Society
APWC	Antennas and Propagation in Wireless Communications
CSNDSP	Communication Systems, Networks and Digital Signal Processing
GASS	General Assembly and Scientific Symposium
IEEE	Institute of Electrical and Electronics Engineers
IET	Institution of Engineering and Technology
URSI	International Union of Radio Science (*Union Radio Scientifique Internationale*)

1. Scope

This Deliverable lists the scientific contributions from RADAVANT's project, during its execution. Annex I and II include their content and complete publications.

Patents and Intellectual Property, which can anyhow be considered and scientific results, are listed and summarily described in Deliverable E6.6, "IP and Patent Contributions from the RADAVANT project", specifically dedicated to such.

2. Scientific Contributions

2.1. Journal Papers

João Reis, Mário Vala and Rafael Caldeirinha, "Review paper on Transmitarray Antennas", IEEE Access, June 2019;

João Reis, Carlos Ribeiro and Rafael Caldeirinha, "A Compact 3D-printed Reflector Antenna for Radar Applications at K-band", in international journal IET Microwave, Antennas and Propagation, June 2020 (in press, at the time of this document).

2.2. Conference Papers

Rafael Caldeirinha, João Reis, André Sardo, Luís Duarte, Nuno Leonor, João Gil and Carlos Ribeiro, "Disruptive Future of Radar Based on All-Digital PN Signal Processing", IEEE-APS Topical Conference on Antennas and Propagation in Wireless Communications (APWC 2019), Granada, Spain, September 2019;

João Reis, Rafael Caldeirinha and Carlos Ribeiro, "Novel parabolic dish antenna for RADAR applications", The IET's Antennas and Propagation Conference APC 2019, Birmingham, UK, November 2019;

André Sardo, João Reis, Luis Duarte, Nuno Leonor, Carlos Ribeiro, Rafael Caldeirinha, "STDCC radar at 24 GHz: first measurement trials", XXXIII General Assembly and Scientific Symposium (GASS) of the International Union of Radio Science (*Union Radio Scientifique Internationale-URSI*), Rome, Italy, August 2020;

Luís Duarte, Carlos Ribeiro, Luís N. Alves and Rafael Caldeirinha, "All-digital reconfigurable STDCC radar baseband implementation in FPGA", 12th IEEE/IET International Symposium on Communication Systems, Networks and Digital Signal Processing - CSNDSP, Porto, Portugal, July 2020;

Luís Duarte, João R. Reis, Nuno Leonor, Carlos Ribeiro, Luís N. Alves and Rafael F. S. Caldeirinha, "Reconfigurable millimetre-wave RF front-end for radar and 5G applications", 12th Conference on Telecommunications (ConfTELE), Leiria, Portugal, Feb. 2021 (paper accepted at the time of this document, to be published later on).

3. Conclusions

This Deliverable E6.7 lists the scientific contributions, journal and conference papers, in which the work developed within RADAVANT has been presented.

Work related to RADAVANT's radar processing blocks and the radar antennas has been published and disseminated in several important scientific, international and national, journal and conference papers.

Annex I - Scientific Journal Publications

Review paper on Transmitarray Antennas

Article *in* IEEE Access · July 2019

DOI: 10.1109/ACCESS.2019.2924293

CITATIONS
0

READS
118

3 authors:

João Reis
Instituto Politécnico de Leiria
20 PUBLICATIONS **45** CITATIONS
SEE PROFILE

Mário Vala
Institute of Telecommunications
6 PUBLICATIONS **1** CITATION
SEE PROFILE

Rafael F. S. Caldeirinha
Instituto Politécnico de Leiria
180 PUBLICATIONS **648** CITATIONS
SEE PROFILE

IEEE Access
Multidisciplinary | Rapid Review | Open Access Journal

Date of publication xxxx 00, 0000, date of current version xxxx 00, 0000.

Digital Object Identifier 10.1109/ACCESS.2017.DOI

Review paper on Transmitarray Antennas

JOAO R. REIS[1,2], MARIO VALA[1,2], RAFAEL F. S. CALDEIRINHA[1,2], (Senior Member, IEEE).
[1]Instituto de Telecomunicações, Leiria, Portugal
[2]Polytechnic Institute of Leiria, Leiria, Portugal

Corresponding author: Joao R. Reis (e-mail: jvreis@co.it.pt).

This work is partially supported the European Regional Development Fund (FEDER), PO CENTRO/SI-IDT, Project RADAVANT (03/SI/2017 - Project n.º 033907) and by the Portuguese Government, Foundation for Science and Technology, FCT, through the financial support provided under: UID/EEA/50008/2019.

ABSTRACT This article presents a thorough review on transmitarray devices particularly aiming antenna beamsteering, gathering some of the most relevant solutions published by the scientific community in the field. Firstly, the background for realising one- and two-dimensional antenna beamsteering with a transmitarray is introduced. Subsequently, several examples of unit-cells for transmitarray implementation and complete transmitarray designs presented in the literature are outlined. Each solution is analyzed in detail, identifying the nature of its layout, *e.g.* based on microstrip patchs, frequency selective surfaces (FSS) or metamaterials (MM), and the method employed to enable electronic reconfigurability, *e.g.* p-i-n diodes, varactor diodes or Microelectromechanical systems (MEMS). In addition, some models with the capability of controlling the wavefront polarization modes are also included herein since these are the base of hybrid transmitarrays, *i.e.* transmitarray with both electronic beamsteering and polarization control. Finally, all the models are compared against each other in order to highlight their benefits and limitations, summarizing their main characteristics such as frequency of operation and bandwidth, insertion loss, physical dimensions and maximum beamsteering range, when available.

INDEX TERMS antenna, beamsteering, beamforming, metamaterials, polarization, transmitarray;

I. INTRODUCTION

ANTENNA beamsteering is a very useful and desirable technique in any wireless communication system since it allow to dynamically adjust the antenna pattern and consequently enhance reception [1]. Such feature is crucial to some applications that require tracking of objects and adaptation to dynamic scenarios with multi-path and moving scatterers, e.g. base-station dynamic antenna alignment, wireless backhaul links auto-alignment due to pole swaying and twisting in the wind or mobile user tracking. Since such antenna systems is focusing their energy toward the receiver, it is increasing the useful received signal level and thus, lowering the interference level. I.e. an higher Signal-to-inference Ratio increases the capacity of the system and improves range and the coverage area.

The most traditional manner of implementing beamsteering is by using arrays of antenna [1]–[3]. However, the well known design limitations particularly regarding to the feeding network implementation, lead to the introduction of alternative techniques to perform beamsteering. In 1986, *McGrath* firstly introduced in his paper [4] a microwave lens with focusing and scanning capabilities, by simply connecting two microstrip patch antennas using vias in both sides of a planar structure, forming a spatial array of microstrip patches, *i.e.* a transmitarray. Since then, transmitarray has been seen as a feasible alternative to phased antenna arrays and the focus of novel and extensive research nowadays.

Transmitarray [5]–[7] is the conventional name given to structures that can modify the original radiation pattern of a directional antenna source, *e.g.* horn antenna, when placed at a distance sufficiently away from the its aperture. To the set composed by the structure and the radiating source, it is referred as transmitarray antenna [5]–[7]. Due to their electromagnetic properties, such structures are be capable of modifying the characteristics of the incident Electromagnetic (EM) wave emitted by the source, and perform beamsteering, focusing or even polarization control, by re-transmission of the incident EM wave. Thus, one can imagine a transmitarray acting, in a sense, like a lens, allowing to pass-through the incident wave with an alteration (or not) of its direction of

This article has been accepted for publication in a future issue of this journal, but has not been fully edited. Content may change prior to final publication. Citation information: DOI 10.1109/ACCESS.2019.2924293, IEEE Access

propagation, as depicted in Fig. 1a. The direction to which the incident wave is being re-radiated depends on the design of the structure. These structures are commonly composed by several resonant unitary elements (unit-cells) with a spatial periodicity forming a planar array [5]–[7]. The unit-cells are typically based on simple microstrip patches, or inspired by metamaterials (MM) [8], [9] and frequency selective surfaces (FSS) [10]–[13]. From a practical point of view, since transmitarray structures are mostly implemented using Printed Circuit Board (PCB) technology [5]–[7], by etching the unit-cell geometries on a copper covered substrate, they benefit from being planar and thus easy to integrate with other peripherals. Furthermore, they are compatible with Surface Mount Technology (SMT) allowing to reduce the size of assemblies, and finally, since they have the electromagnetic feeding source separated from the beamsteering network, they offer higher degree of modularity to the system as opposed to traditional antenna array. Thus due to their design simplicity and, more importantly, due to the low manufacture costs, they have been extensively utilized for numerous antenna applications.

In order to achieve reconfigurability and enable features, such as electronic beamsteering, polarization control or frequency tuning, transmitarray are typically enhanced by using p-i-n diodes, varactor diodes, radio frequency (RF) or microelectromechanical-systems (MEMS) switches or manufactured using tunable substrates as liquid crystal or graphene. However, each of these methods present advantages and disadvantages, *e.g.* p-i-n and varactor diodes are widely utilized in transmitarray designs from low RF to around 30 GHz, mostly due to their size, easy integration in PCB and low cost. However, they are limited when operating at high frequencies (above 30 GHz), with insertion loss proportional to the frequency of operation that arise from their intrinsic parasitic parameters (series resistance, capacitance and inductance). RF and MEMS switches are typically more expensive than p-i-n/ varactors and prone to failure over time, due to the wear and tear of the mechanical parts. Alternatively, tunable dielectric materials, *i.e.* materials that can have their electromagnetic properties (in particular ϵ_r) manipulated by an external stimulus (bias or voltage), such as liquid crystal and graphene are also employed for transmitarray implementations [14]–[20]. Furthermore, while liquid crystal technology have been successfully employed in transmitarray designs [14], it is more commonly used in reflectarray implementations [21]–[24] or as grounded substrate for conventional microstrip antennas [25]–[27]. Graphene substrates, on the other hand, are typically used at THz frequencies due to their unique electronic properties as reported in [28], even though applications in antennas design at micro- and millimeter-wave frequencies, have already been reported in [29].

The research on transmitarray has always been paired to the one on reflectarray [30], [31]. Reflectarray, which operating principle is depicted in Fig. 1b, makes use of the reflection principle (based on Snell's law [30], [31]) to

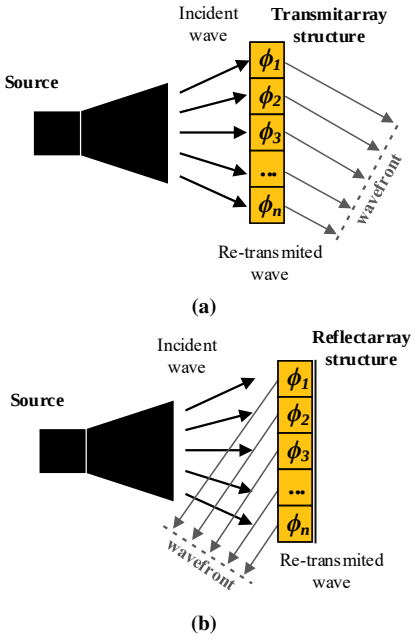

FIGURE 1: Generic model of (a) a transmitarray and (b) a reflectarray antenna.

modify the properties of the re-transmitted EM wave. In fact, the most significant difference between a transmitarray and reflectarray is that, in the latter, all power is re-radiated independent on the frequency or cell design. If the unit-cells are not matched to the frequency of operation, the elements will have small effect on the array response and the reflecting ground plane will predominate. In the worst case scenario, the reflected wave could have the same direction of the original one [30], [31]. On the other hand, for a transmitarray, if the structure is not well matched to the free-space or if the unit-cells are not adapted to the frequency of operation, the incident EM wave will be totally reflected back, resulting in no transmission through the structure [5], [6]. Therefore, a transmitarray is desirable to be the most "transparent" as possible, introducing very low loss so the EM field of the propagating wave is not severely attenuated, whereas the reflectarray is desirable to be a perfect reflecting surface so the incident wave can be entirely reflected.

However, although reflectarray have been successfully implemented in [7], [30]–[36], the feed blockage remains a challenge in implementation of such type of devices since the feeding source is on the same side of the radiated field. This may be a challenging depending on the final application that can be overcome with the use of a transmitarray.

To this extent, this paper presents an overview of the literature on transmitarray aiming antenna beamsteering. It starts by introducing the theoretical background for antenna beamsteering using a transmitarray. In particular, the mode of operation of 1 dimensional (1D) and 2 dimensional (2D) beamsteering with a transmitarray are described. Subsequently, a dedicated review based on several journal and conference publications, is presented. The overview presents

This article has been accepted for publication in a future issue of this journal, but has not been fully edited. Content may change prior to final publication. Citation information: DOI 10.1109/ACCESS.2019.2924293, IEEE Access

a critical analysis on several electronically reconfigurable transmitarrays for antenna beamsteering, based on microstrip patch, FSS or MM, employing either p-i-n diodes, varactor diodes or MEMS switched to achieve reconfigurability. In addition, several transmitarray models with polarization control capabilities are also included in this paper yielding to the introduction of hybrid transmitarray, with both electronic beamsteering and polarization control capabilities. Finally, the most relevant transmitarray designs proposed by several authors are compared against each other in order to highlight its benefits and limitations. Their main characteristics such as frequency of operation and bandwidth, insertion loss, physical dimensions and maximum beamsteering range, are then summarized.

The paper is organized as follows: section II presents the mathematical ground for beamsteering with a transmitarray; Section III outlines the state of the art on Transmitarray covering in particular transmitarray for antenna beamsteering, polarization control and hybrid transmitarray, that enable both features simultaneously. Finally, the main conclusions are drawn in section IV.

II. BEAMSTEEERING WITH A TRANSMITARRAY

A. THEORETICAL MODEL FOR 1D–BEAMSTEERING

The principle of beamsteering using a traditional transmitarray can be compared to the one using a linear antenna array. Figure 2 depicts both configurations for comparison. In a linear antenna array, the phase shifting is applied to the signal in each individual branch using a phase shifter [1]–[3], whilst in a transmitarray the phase shifting is obtained by controlling the phase delay introduced by each individual elements of the transmitarray, as reported in [5]–[7], [37]–[56].

When an incident Electromagnetic (EM) wave propagates through a transmitarray of length l, composed by N elements of periodicity p (Fig. 2b), it experiences a different phase shifting γ_n expressed by (1), after penetrating each of the elements of the array in the steering direction theta (θ),

$$\gamma_n = \frac{2\pi}{\lambda_0}.p.n.sin\theta = k_0.p.n.sin\theta, \tag{1}$$

where $k_0 = \frac{2\pi}{\lambda_0}$ is the wave number in free space.

Consequently, the transmission phase α_n in the n^{th} element, can be defined by (2),

$$\alpha_n = -\gamma_n + \alpha_0 + 2\pi i, \qquad i = 0, 1, 2, ... \tag{2}$$

where α_0 is the phase of the incident EM wave at the input of the transmitarray.

Therefore, the re-transmitted wave direction θ can be expressed as a function of the phase difference ψ between adjacent elements, *i.e.* progressive phase, using (3),

$$\begin{aligned}\psi = \alpha_n - \alpha_{n-1} = -\gamma_n + \gamma_{n-1} = \\ = -k_0.p.n.sin\theta + k_0.p.(n-1).sin\theta = \\ = -k_0.p.sin\theta.\end{aligned} \tag{3}$$

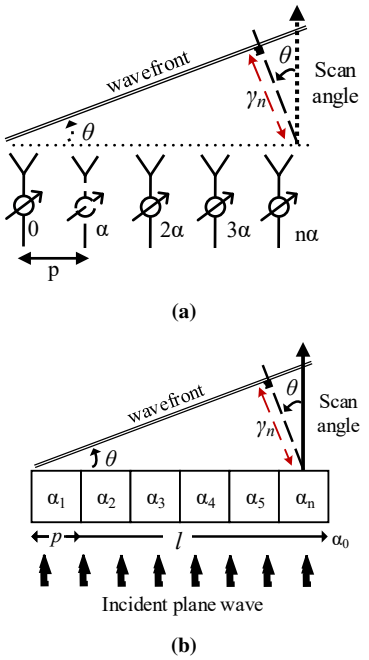

FIGURE 2: (a) Model of linear antenna array and (b) model of a transmitarray for 1D beamsteering analysis.

Thus, by varying the phase α_n of each array element in a progressive way, the incident wave can be steered to a desired direction θ relative to the normal of the structure, defined by (4),

$$\psi = -k_0.p.sin\theta \Leftrightarrow \theta = -sin^{-1}\left(\psi.\frac{\lambda}{2\pi.p}\right) \tag{4}$$

However, since the phase distribution in the array is applied along a single direction only, the model for a linear transmitarray limits its application to 1D beamsteering. Therefore, the main lobe of the radiation pattern of the original antenna in which the transmitarray is applied, only has the capability to be steered towards the output angle with θ component, as reported in some of the references included in the literature review [14], [37]–[39], [47], [48], [52], [53].

B. THEORETICAL MODEL FOR 2D–BEAMSTEERING

In order to extend the concept to 2–D beamsteering using a transmitarray, it is proposed herein to characterise the model by analogy with a planar antenna array. This vision enable the transmitarray to have the control over the two angular components theta (θ) and phi (ϕ) of the output angle direction, simultaneously, raising the limitation of 1D beamsteering of the previous model. The transmitarray model for 2D beamsteering is depicted in Fig. 3.

Built on the theory of planar antenna arrays, presented in [1] and [3], a progressive phase shift between adjacent elements should occur along the X and Y directions of the $M \times N$ array so 2D beamsteering could be enabled. Thus, by expanding from (3), the relation between the two dimensional

This article has been accepted for publication in a future issue of this journal, but has not been fully edited. Content may change prior to final publication. Citation information: DOI 10.1109/ACCESS.2019.2924293, IEEE Access

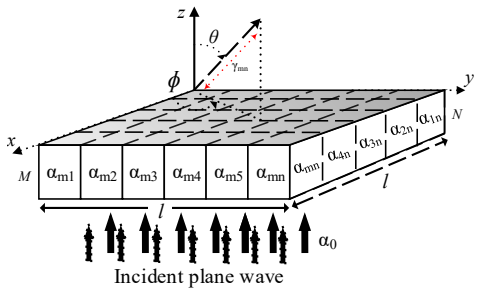

FIGURE 3: Proposed model for a transmitarray with 2D beam-steering.

output directions (θ,ϕ) and the progressive phase delay, is given by (5),

$$\begin{cases} \psi_x = -k_0.p.sin(\theta).cos(\phi) \\ \\ \psi_y = -k_0.p.sin(\theta).sin(\phi) \end{cases}, \tag{5}$$

where ψ_x and ψ_y are the progressive phase along X andY axis, respectively, and p is the periodicity of the $p \times p$ array elements.

Therefore, a $M \times N$ transmitarray would exhibit a relative phase distribution that can be represented by the matrix (6),

$$\begin{array}{c} \\ \psi_y \downarrow \end{array} \begin{array}{c} \longrightarrow \psi_x \\ \begin{bmatrix} \alpha_{1,1} & .. & .. & .. & .. & \alpha_{1,n} \\ .. & .. & .. & .. & .. & .. \\ .. & .. & .. & .. & .. & .. \\ \alpha_{m,1} & .. & .. & .. & .. & \alpha_{m,n} \end{bmatrix} \end{array} \tag{6}$$

where $\alpha_{m,n}$ is the phase delay introduced by each individual (m,n) element of the transmitarray. This representation is proposed herein to facilitate the understanding of the progressive phase along the transmitarray and will be further considered herein.

From this analysis, it can be concluded that the output steering direction (θ,ϕ) depends on the transmission phase $\alpha_{m,n}$ of each element of the 2–D transmitarray, and similarly to (2) (linear case), the phase shifting in each individual element can be described by (7),

$$\alpha_{m,n} = -\gamma_{m,n} + \alpha_0 + 2\pi i, , \qquad i = 0, 1, 2, ..., \tag{7}$$

where the phase shifting of each element $\alpha_{m,n}$ is a periodic function, and $\alpha_{m,n} \subset [0, 2\pi]$ such as in the 1-D case. Thus, each element of the transmitarray must always be capable to achieve at least 360° (2π) of transmission phase shift, to ensure a complete control of the output angle.

Notwithstanding, in order to directly match the output angle direction obtained from the theory with the output angle direction given either by simulation and experiments, it is proposed, by this work, to apply in the theoretical model a coordinate system conversion from Spherical coordinates (represented by θ and ϕ components) to *Azimuth-over-Elevation* (represented by the pair *Az/El*). Therefore, the

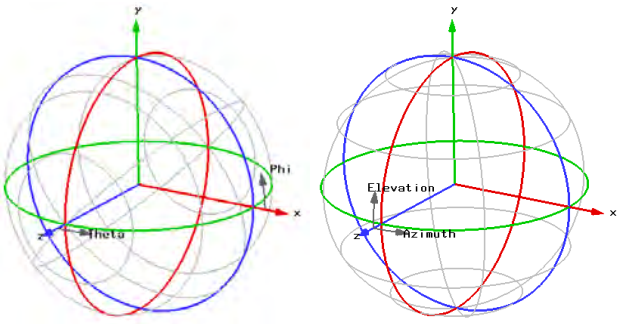

(a) **(b)**

FIGURE 4: Axial representation of the (a) spherical coordinate system (θ/ϕ) and (b) *Azimuth-over-Elevation* coordinate system (Az, El).

mathematical relation between spherical and *Az/El* coordinates well detailed in [57], given by (8), has been applied here:

$$\begin{cases} sin(\theta).cos(\phi) = cos(El).sin(Az) \\ \\ sin(\theta).sin(\phi) = sin(El) \end{cases}. \tag{8}$$

The main differences between both coordinate systems rely on the origin of the axis, as depicted in Fig. 4. From the mathematical workout resultant of replacing (8) in (5), a generic formula to calculate the output angle direction with *Az/El* components provided by a 2D transmitarray, is given by (9),

$$\begin{cases} \psi'_x = -k_0.p.cos(El).sin(Az) \\ \\ \psi'_y = -k_0.p.sin(El) \end{cases}. \tag{9}$$

III. STATE-OF-THE-ART ON TRANSMITARRAY ANTENNAS

A. TRANSMITARRAY FOR ANTENNA BEAMSTEERING

Several examples can be found in the literature for transmitarray aiming antenna beamsteering. They comprise the use of different materials, unit-cells designs and implementation approaches. However, there is one requirement that must be satisfied to use such structures to steer the main beam of an antenna radiation pattern. The unitary element that composes the transmitarray must have transmission phase that can be varied (tunable) up to 360° (as mentioned in section II-B), while the transmission magnitude (desirably) remains constant over the bandwidth,. Therefore, this section is focused on the review of transmitarray structures and unit-cell elements, with reconfigurable capabilities that enable electronic beamsteering.

1) Reconfigurable based on microstrip patches

Particularly in [37], a reconfigurable transmitarray for beam-steering is proposed. The device is composed of a set of patch antennas placed on each side of the array structure and

This article has been accepted for publication in a future issue of this journal, but has not been fully edited. Content may change prior to final publication. Citation information: DOI 10.1109/ACCESS.2019.2924293, IEEE Access

connected by an electronically tunable phase-shifter, where the innovation of the work relies on. The phase-shifter is developed in transmission line technology and consists of a microstrip directional coupler terminated with reflective LC circuits, whose capacitance (C) is controlled by a varactor diode. Consequently, by tuning the value of C, it is possible to selected whether the terminations of the coupler are open- or short- circuit and thus, control the phase-shift between the input and the output of the transmitarray. Nevertheless, this solution turned out to be limited in terms of phase range and since several couplers are cascaded together to overcome this issue, the size and complexity of the phase-shift network is consequently increased. This forced a large separation between the radiating elements, that were arranged in groups of 4 elements and separated by 1.4 wavelengths, leading to the reduction in the scan capability and to the appearing of grating lobes. Therefore, a maximum of 9° of angular shift is reported on the azimuth plane. The proposed solution presents 700 MHz of bandwidth and 3 dB of insertion losses but such values are advertised for the phase-shifter alone and not for the complete transmitarray.

Remarkably in their work, *Lau* and *Hum* [5], [38]–[41] have introduced several models of active unit-cells and of electronically controlled transmitarray. Specifically aiming antenna beamsteering, it is presented and characterized in [38] and further improved in [39] a transmitarray element (Fig. 5a) that consists of two microstrip patches on either side of a ground plane coupled to a small slot aperture. Each patch is split in half with a small gap in between, and varactor diodes inserted to connect the two halves, while another varactor diode is inserted at the center of the slot, connecting the two sides of the slot. Together, all these parts act as three coupled tunable resonators that provides a variable phase-shift over 360° with 3 dB of insertion losses, as reported in [39]. However, the losses are slightly increased to 4.8 dB (over the same bandwidth), when the proposed element is composing a 6×6 array and the biasing network to control the varactors are included, as depicted in Fig. 5b [39]. Nonetheless, the developed prototype achieved $\pm 25°$ of electronically controlled beam scanning, in azimuth and elevation planes independently, with a broadside directivity of 20.8 dBi.

As alternative, a different unitary element is proposed and characterized by the same authors in [40]. The unit-cell for transmitarray applications explores the properties of proximity-coupled feeding and aperture coupling [1]. In this solution, the array element is implemented with microstrip patches in both sides of the structure separated by a ground plane. Each patch fed a differential microstrip transmission line by mutual coupling. In one of the sides, possess a differential bridged-T phase-shifter composed by varactor diodes and DC blocking capacitors. Both sides of the structure are further interconnected also by aperture coupling through two open slots etched in the ground plane. According to experiments realized on a single unit-cell using the waveguide method, which consists of a sample of the unit-cell enclosed

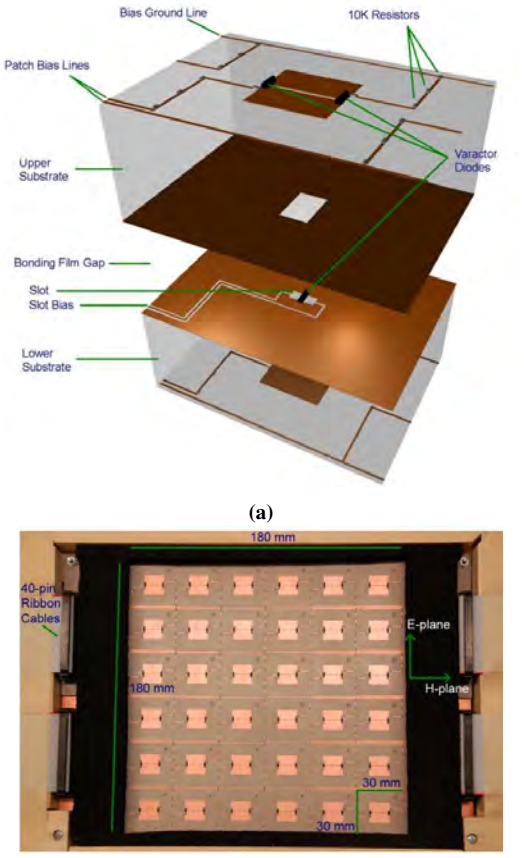

FIGURE 5: (a) Reconfigurable element (exploded-view) and (b) respective transmitarray prototype (images extracted from the work presented in [39]).

between two waveguide flanges, it is notably achieved a tunable phase range of around 425° and insertion loss in average of 3.4 dB at 4.86 GHz. This model is however limited by the narrow bandwidth of the radiating elements and such drawback is mitigated, on a final prototype by employing a stack of microstrip patches. The final array element exhibits insertion losses of around 3.6 dB with a phase range over 400°, but the bandwidth was increased from 100 to 500 MHz at the same central frequency. Subsequently, a 6×6 reconfigurable transmitarray composed of active elements of [40] is finally presented and evaluated in terms of beamsteering performance in [41]. The prototype of the transmitarray provides a scanning range of $\pm 50°$ in both elevation and azimuth planes, with 2.2 dB of insertion losses and 10% bandwidth (500 MHz) at 5 GHz.

Moreover, in [42], a novel unit-cell design is proposed and characterized for an electronic control of the wave direction using a transmitarray. It is composed of a passive microstrip patch antenna with U-shape slot etched on the reception plane, and an active patch with an etched O-shape slot in the re-transmission plane, as depicted in Fig. 6a. The active O-

This article has been accepted for publication in a future issue of this journal, but has not been fully edited. Content may change prior to final publication. Citation information: DOI 10.1109/ACCESS.2019.2924293, IEEE Access

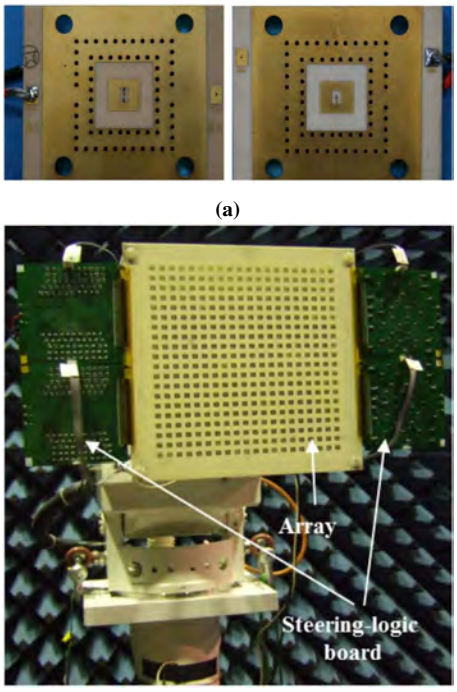

FIGURE 6: (a) Unit-cell design and (b) transmitarray prototype for antenna beamsteering (images extracted from the work presented in [42] and [44], respectively).

shape is loaded with two p-i-n diodes (and in an alternative design with RF- MEMS) that allow to control the transmission phase by alternatively activating diode states. A 15% of bandwidth and around 3 dB of insertion losses at 10 GHz are reported experimentally on a single unit-cell, evaluated using the waveguide method also employed in [40]. Later in [43], the same unit-cell design using MEMS presents a bandwidth of 16% but 4 dB of insertions losses. In [44] the authors presented a full characterization of a 20×20 transmitarray comprising 800 p-i-n diodes and the respective feeding mesh. The prototype is depicted in Fig. 6b. The authors state that the proposed transmitarray exhibits a 2D beamsteering capability with maximum ranges of $\pm 40°$ in elevation and $\pm 70°$ in azimuth.

Another unit-cell for beamsteering transmitarray at Ka-band based on p-i-n diodes is presented in [45]. The paper starts by characterizing by simulations an novel unit-cell design. In particular, this novel unit-cell design allows for a 2-bit phase resolution and has an overall size of $5.1 \times 5.1 \times 1.3mm^3$ ($\lambda/2 \times \lambda/2 \times \lambda/8$ at 29 GHz). The unit-cell is composed of six metal layers printed on three substrates as shown in Fig. 7b, of which the ones at the edges are O-slot rectangular patch antennas loaded with two p-i-n diodes for phase control. Similar to other cases already presented [42], [44], the p-i-n diodes in each of the antennas are biased in opposite states (one p-i-n diode is ON while the other is OFF). By choosing which diode is ON at a given time, a $180°$ phase-shift is achieved. Therefore, by combining the different

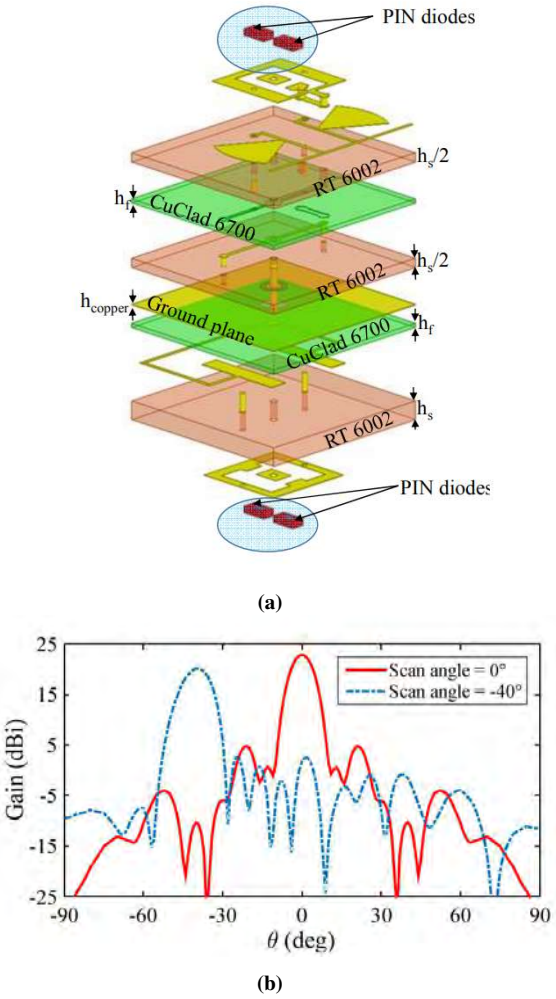

FIGURE 7: (a) Schematic view of the 2-bit unit-cell and (b) simulated radiation pattern for two angles (images extracted from the work presented in [45]).

states of the receiving and transmitting layers, a total of four phase.shifts can be achieved ($0°$, $90°$, $180°$ and $270°$). The presented unit-cell is used to implement a 14×14 element transmitarray in simulation environment whose beamsteering range is reported up to $-40°$, as shown in Fig. 7b.

More recently, in [46] a new unit-cell for a beamsteering transmitarray is presented. Each cell is comprised of four stacked Rogers RO4350B double sided layer, as depicted in Fig. 8a. Since one pair of layers (sub-element) can only achieve $180°$, this arrangement has to be replicated in order to achieve the desired $360°$ of phase shift. Varactor diodes are used in every layer to control, electronically, the element phase-shift. Although the paper reports a bandwidth of 1 GHz for the unit-cell at 24.6 GHz, this value is defined by the frequency range in which the phase-shift is above 360 degrees, and not from the S_{11}/S_{22} filtering response as normally characterized in this type of work. This unit-cell, exhibits then a total insertion loss of around -5 dB obtained

This article has been accepted for publication in a future issue of this journal, but has not been fully edited. Content may change prior to final publication. Citation information: DOI 10.1109/ACCESS.2019.2924293, IEEE Access

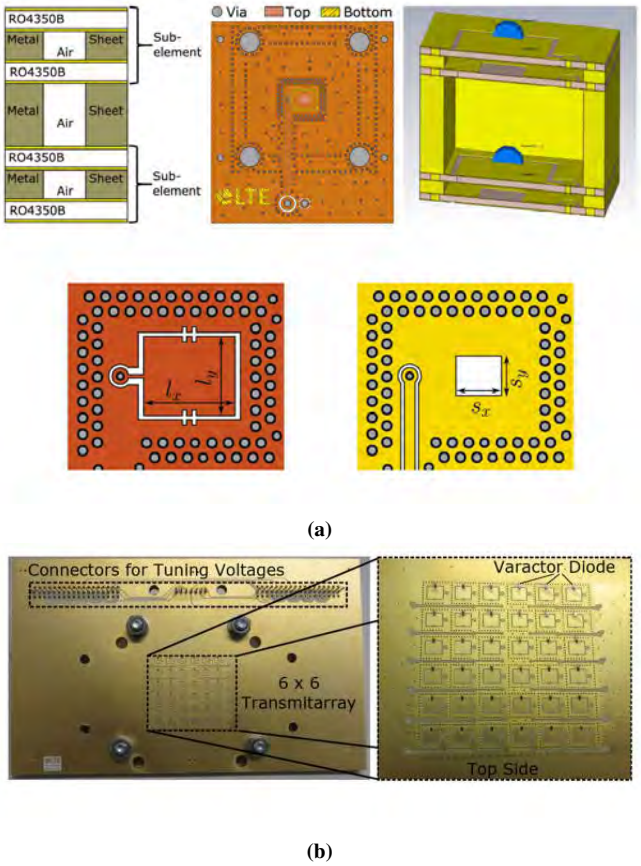

FIGURE 8: (a) Unit-cell design and (b) top view of assembled 6x6 transmitarray prototype (images extracted from the work presented in [46]).

in simulation and -12 dB obtained experimentally. Finally in [46] a 6×6 transmitarray composed of the aforementioned unit-cell has been built (Fig. 8b). This transmitarray is able to steer the main beam direction up to $\pm 50^\circ$ in both the azimuth and elevation planes, at 24.6 GHz, with a maximum attenuation of 17 dB at the extremes of the steering interval.

2) Reconfigurable based on tunable metamaterials

Transmitarray composed of metamaterials (MM) to perform antenna beamsteering are also reported in the literature. Metamaterials are artificial man-made structured materials able to produce electromagnetic properties (permittivity, permeability and refractive index) which are unusual or non-existent in nature [8], [9] and such properties can be explored for transmitarray designs.

It is the case of the work described in [14], [47] and [48], where 1D beamsteering, *i.e.* main lobe limited to steering in a single plane, is demonstrated using such type of materials. These works [14], [47], [48] suggest new steerable antennas by using controllable MM (electronically reconfigurable) to form the transmitarray. Although implemented with different resonant unit-cell designs, they all respect the same physical principle: tunable refractive index structures are utilized to electronically control the direction of the outcoming wave.

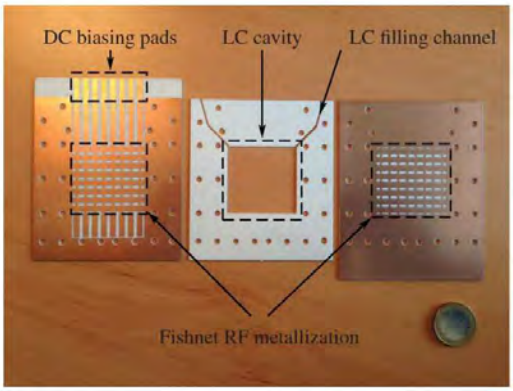

FIGURE 9: Prototype of a single opened fishnet unit-cell layer (images extracted from the work presented in [14]).

The steering is achieved when the refractive index of the MM structure is tuned, leading to a progressive phase distribution along the structure, acting as a linear phased array.

For example, in [14] the authors have developed and characterized an artificial gradient-index metamaterial by designing a fishnet structure on a liquid crystal substrate. The transmitarray was practical validated against measurements conducted at 27.5 GHz. A beamsteering angular range limited to $\pm 5^\circ$ was achieved by varying, in a gradient manner, the bias of each array column. According to the authors, the yielded angular range can be enhanced by staking more layers of the one depicted in Fig. 9.

In [47] and [48], the authors have followed an alternative approach to design their transmitarray. Both presented structures are composed of staked layers of periodically printed sub-wavelength metallic resonators with embedded microwave varactors. By adjusting the varactor diode, the resonant characteristics of the unit-cell is modified controlling, in fact, the associated phase-delay between the first and the last layer of the transmitarray. Consequently, the associated effective refractive index of a single transmitarray element is being adjusted. Accordingly, if a progressive phase between adjacent elements is applied through the array in order to perform beamsteering, the metamaterial exhibits a gradient index of refraction, when seen as an whole.

Therefore in [47], 6 stacked layers of a double-layer I-shaped unit-cell (Fig. 10a) are suggested as array element, exhibiting 360° of phase-shift at 1.6 GHz while the varactor is tuned from 0.1 pF to 1.9 pF, with insertion losses of 4 dB (averaged). Bandwidth is not referred by the authors. A continuous scanning range of $\pm 30^\circ$ in the azimuth plane is achieved using a full wave simulator. Although it is stated that experimental results obtained on a prototype are consistent with simulation ones, the paper lacks a more elaborated and physically grounded analysis of the results.

Notably in [48], a complete characterization of a metamaterial transmitarray composed by the unit cell presented in Fig. 10b was performed. In addition to the transmitarray, an array of microstrip patch antennas was also developed to

This article has been accepted for publication in a future issue of this journal, but has not been fully edited. Content may change prior to final publication. Citation information: DOI 10.1109/ACCESS.2019.2924293, IEEE Access

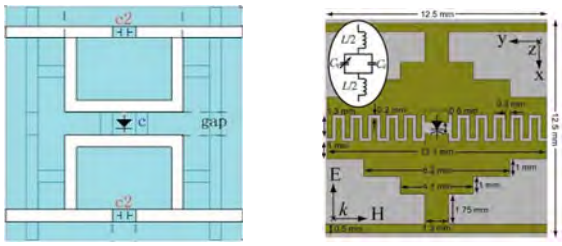

(a) **(b)**

FIGURE 10: Metamaterial unit-cells for transmitarray antennas presented by (a) *Yongzhi S. et. al.* and by (b) *Jiang T. et. al.* (images extracted from the work presented in [47] and [48], respectively).

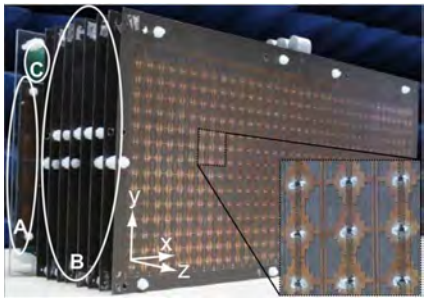

(a)

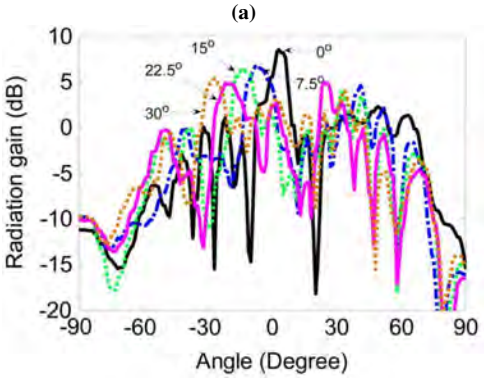

(b)

FIGURE 11: (a) Prototype of the MM beamsteering antenna and (b) measured radiation pattern for different steering angles (images extracted from the work presented in [48]).

serve as feeding source. The prototype, implemented on a stacked layer structure (Fig. 11a), presents an angular steering range of $\pm 30^\circ$ in azimuth verified under experiments at 4.7 GHz. Some samples of radiation pattern are demonstrated by the authors in their paper and illustrated in Fig. 11b.

Although introduced as metamaterials by analyzing the refractive index of the array element, it can be noticed that such structures are in fact frequency selective surfaces. While the unit-cell presented in [47] exhibits a low-pass filtering frequency response, the unit-cell of reference [48] possesses a band-pass filtering type. Herein, is when the term metamaterials could be misleading due to large ambiguity of the definition.

3) Reconfigurable based on FSS

Frequency selective surfaces [10]–[13] are, per se, a timely topic on the field of (antennas and) propagation that have been studied for years. A FSS is a spacial filter that exhibits distinct resonant filtering characteristics *e.g.*: band-pass, band-stop, high-pass or low-pass, that depend on the format and on the dimensions of periodic resonant geometries etched over a metallic coated substrate [10]–[13]. As a spacial filter, these structures are able to allow or block the propagation of an incident EM wave within a specific frequency band and even control its propagation phase.

Much of the work about FSS relies on the study and development of novel unit-cell designs for EM blockage (shielding) or radio coverage enhancement [10]–[13]. However, new applications have recently emerged by exploring the use FSS in various transmitarray implementations [49]–[56], [58] and in novel antenna designs [59]–[61].

For example in [58], a wide-band transmitarray is suggested by using a FSS of double square rings unit-cells. The authors have demonstrated that the phase-shift introduced by the transmitarray can be varied by simply modifying the physical size of the squares, and such can be further improved by stacking several layers of FSS on top of each others. In fact, the concept of stacked layers separated by an air gap is widely used for transmitarray implemented with FSS since it allows to increase both the bandwidth and the transmission phase of the structure, as thoroughly reported in [5], [51], [54], [55], [58].

In particular, some examples can be found in [49]–[53] by presenting reconfigurable transmitarray of FSS for antenna beamsteering. The majority of the work utilizes varactor diodes to electronically control the capacitance of the equivalent LC circuit that characterizes the resonant unit-cell design, as presented by *Russo et. al.* in [49]–[51]. In their work, a tunable pass-band FSS suitable for beamsteering operations is proposed. The suggested FSS, depicted in Fig. 12a, is evaluated by simulations in [49], [50] and experimentally characterized in [51], also using the waveguide method (Fig. 12b), previously described. The proposed structure is capable of bandwidths ranging from 1% to 10% (with a few modifications in original design) at 4 GHz, with a transmission amplitude that remains above 3 dB within the varactor tuning range. Although the transmission phase obtained from experiments varies by approximately 360° over the whole bandwidth, making this design suitable for beamsteering, the paper does not include the implementation of a complete transmitarray and respective beamsteering characterization.

In [52], an active FSS based on the traditional squared-slot design with band-pass filtering characteristics is implemented for antenna beamsteering, as depicted in Fig. 13. Varactor diodes are used to tune the FSS and control the phase-shift, with range up to 360°, of a structure composed of 5 stacked layers. In fact, the authors have demonstrated on a physical prototype, illustrated in Fig. 13a, that through different configurations of the bias voltages applied to the varactors, a gradient phase distribution along the transmitar-

This article has been accepted for publication in a future issue of this journal, but has not been fully edited. Content may change prior to final publication. Citation information: DOI 10.1109/ACCESS.2019.2924293, IEEE Access

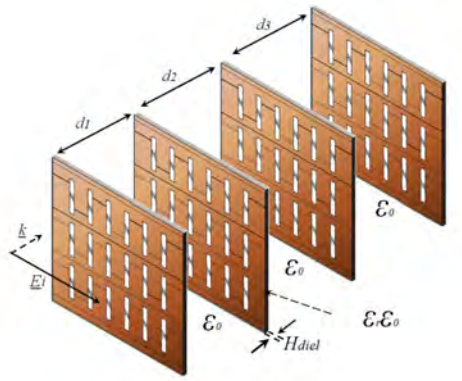

(a)

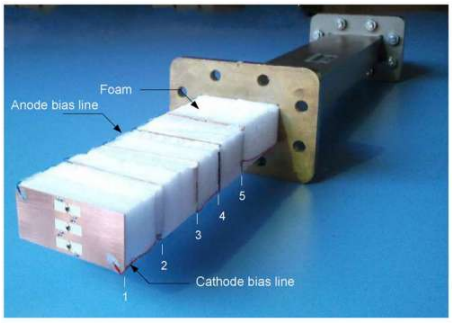

(b)

FIGURE 12: (a) FSS transmitarray model and (b) respective unit-cell prototype evaluated using the waveguide method (images extracted from the work presented in [50] and [51], respectively).

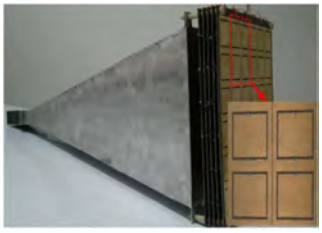

(a)

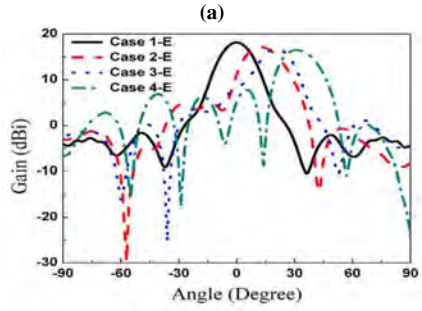

(b)

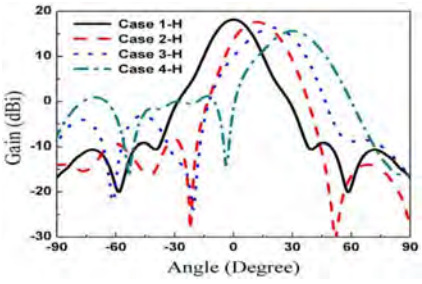

(c)

FIGURE 13: (a) 6×6 transmitarray prototype, (b,c) measured radiation pattern in azimuth and elevation planes, respectively (images extracted from the work presented in [52]).

ray can be utilized to steer the radiation pattern of a horn antenna. This corroborates with the facts presented for MM transmitarray introduced in last section. Although the work show its merits by presenting a tunable steering range of $\pm 30^{\circ}$ in both azimuth and elevation plans at 5.3 GHz, as depicted in Fig. 13b and Fig. 13c respectively, it is a fact that such scanning angle can only satisfy one steering direction at the time. Therefore, two-dimensional beamsteering, *i.e.* steer the main lobe to a direction with two spatial components as presented in Section II-B, is still unachievable with this device.

Alternatively in [53], a tunable FSS with beam steering capability is presented. The FSS is used as a transmitarray with a bandpass characteristic centered at 12 GHz. The novelty of the work relies on the FSS design which is composed of capacitive (parallel electrodes) and inductive (vertical wires) structures printed on a BST thick-film ceramic, as illustrated in Fig. 14. The tunability is performed due to the properties of the BST substrate that can be tuned by applying an external electrostatic field across the material, and not by using discrete components such varactors or p-i-n diodes. By applying a DC field between the electrodes of the capacitor, the effective permittivity is reduced resulting also in a capacitance reduction. Experiments realized on a 40×40 FSS transmitarray (Fig. 14b), report a maximum phase difference of 121° at 12 GHz when the bias voltage is ranging from 0 V (untuned state) and 120 V (maximum tuning state). Within such voltage range, the main beam of a feeding horn antenna is steered up to $\pm 10^{\circ}$ in the azimuth plane, due to the low phase-shift (121°) produced by the structure. Although showing its merits, the proposed solution is one of a type in the literature, possible due to the impractical voltage values necessary to apply for tuning the structure and perform beamsteering limited 1-Dimension, in comparison with other state-of-the-art proposals.

To withdraw such limitation, our research group has been working on a reconfigurable transmitarray model for 2D beamsteering. The transmitarray follows the phase distribution proposed by the theoretical model presented in section II-B in order to enable antenna beamsteering in two dimensional planes. With this mindset, it is presented in [54] and further in [55] the characterization of a FSS transmitarray with controlled beamsteering output direction in the two main antenna planes (azimuth and elevation). Firstly in [54], the theoretical model for 2D beamsteering has been applied

This article has been accepted for publication in a future issue of this journal, but has not been fully edited. Content may change prior to final publication. Citation information: DOI 10.1109/ACCESS.2019.2924293, IEEE Access

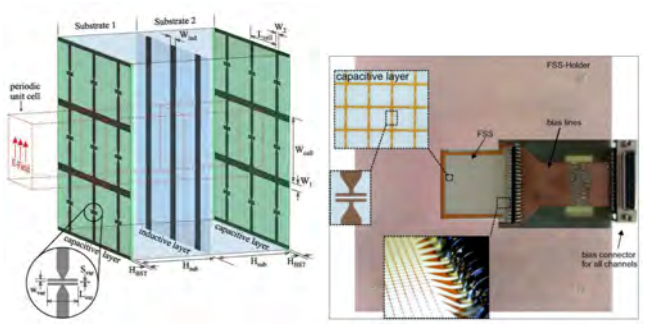

(a) **(b)**

FIGURE 14: (a) FSS transmitarray model and (b) respective transmitarray prototype (images extracted from the work presented in [53]).

on a passive stacked-layer FSS inspired transmitarray. Based on a square-slot pass-band unit-cell layout (as in [52]), the 2D beamsteering model was tested for several beamsteering angles on a 5×5 transmitarray with 5 stacked layers separated by an air gap, at 5.35 GHz. The paper, which also includes a parametric study to evaluate the ideal layer separation distance and the ideal number of layers necessary to achieve a desired phase-shift, reports beamsteering angles up to $\pm25°$ in both elevation and azimuth planes with $3°$ of error between simulation and experimental validating the theoretical 2D model. Although beamsteering is set by the value of each of the 50 discrete SMT capacitor loaded in each layer, the several output angles were achieved by hand-soldering the capacitors for each angular configuration.

Subsequently in [55], the latter model has been improved to enable electronically reconfigurable beamsteering. In the addition to through-layer *vias* per unit-cell, a sixth layer has been added to accommodate the feeding network, as depicted in Fig. 15a. Varactor diodes replaced the discrete SMT capacitors used in the passive transmitarray of [54]. A beamsteering driver has been developed to control, individually, the overall capacitance value of each of the 25 cells of the transmitarray. As result, beamsteering angles up to $\pm28°$ in azimuth and $\pm26°$ in elevation have been accomplished with the physical prototype of Fig. 15b. Two samples of measured radiation pattern are depicted in Fig 15d and Fig. 15e, for $(+15°,+15°)$ and $(+25°,+25°)$, respectively. The reconfigurable transmitarray exhibits insertion loss of 1.6 dB and 4.3 dB in simulation and experiments, respectively. This compares with the experimental results obtained in the passive model by presenting approximately 1.5dB of excess loss at 5.2GHz, due to the intrinsic parasitic effect of the selected varactor diodes.

Another design of FSS-based unit-cells for beamsteering transmitarray is presented in [56]. The unit-cell is based on a C-patch and ring slot loaded with p-i-n diodes (Fig. 16) and is composed of two identical substrates with dimensions of $14\times14\,mm^2$. The ring slot is loaded by a rectangular gap and is placed just beneath the gap of the C-patch. In this particular

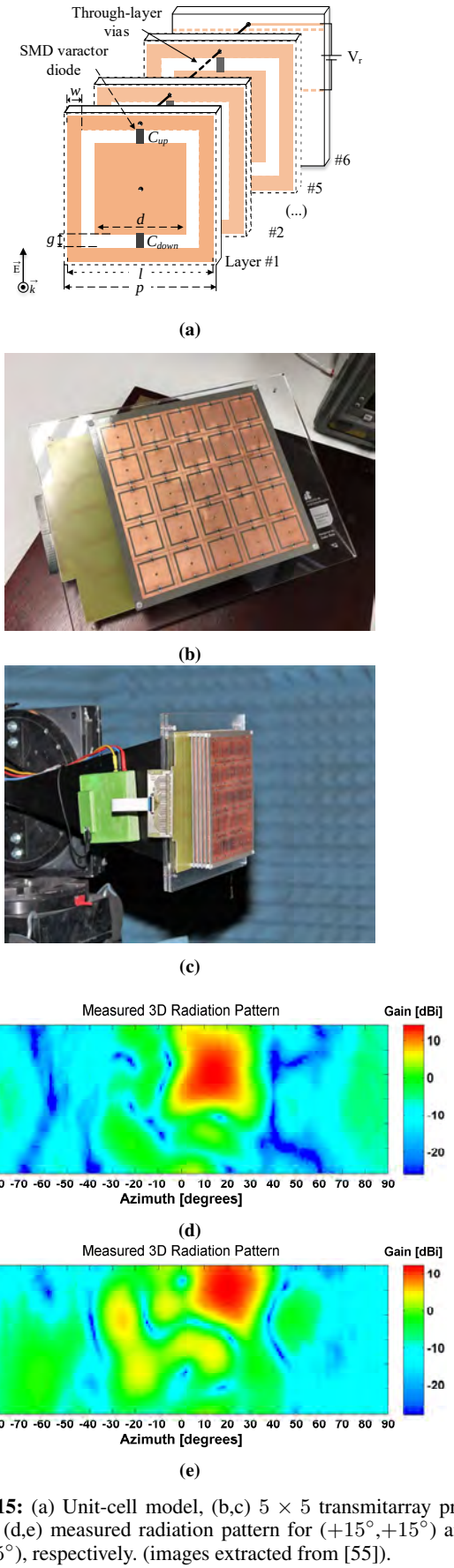

(a) **(b)** **(c)** **(d)** **(e)**

FIGURE 15: (a) Unit-cell model, (b,c) 5×5 transmitarray prototype and (d,e) measured radiation pattern for $(+15°,+15°)$ and $(+25°,+25°)$, respectively. (images extracted from [55]).

This article has been accepted for publication in a future issue of this journal, but has not been fully edited. Content may change prior to final publication. Citation information: DOI 10.1109/ACCESS.2019.2924293, IEEE Access

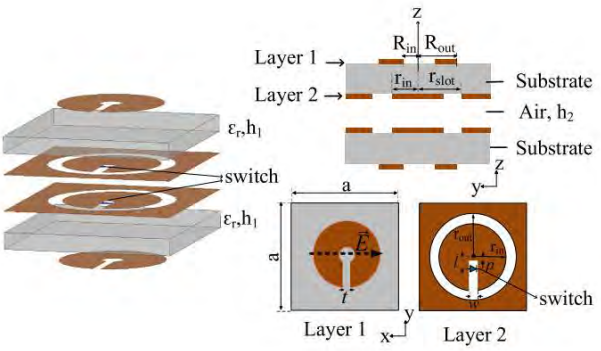

FIGURE 16: Geometry of transmitarray unit-cell (image extracted from the work presented in [56]).

unit-cell, the C-patches act as the receiver and transmitter, while the ring slots act as a phase shifter. The phase shift between the receiver and transmitter can be controlled by modifying the length of the ring slot gaps. In order to change the associated electrical length, each gap is loaded with p-i-n diodes that allow a $180°$ of phase shift at 11.5 GHz. However, since both terminals of the p-i-n diodes are short-circuited, a second rectangular gap was introduced in the cell presented in Fig. 16. This gap is 0.2 mm and is loaded with three 100 pF capacitors in order to the current flow through the gap. The first unit-cell was then simulated in a 12×12 transmitarray to verify its beamsteering capabilities. For each of the cells a single bias line is needed to control the ON/OFF state of the p-i-n diodes. Simulation results show that, at 11.5 GHz, a $\pm 40°$ in both azimuth and elevation planes is achieved. At the moment there are not experiments on this structure.

B. TRANSMITARRAY FOR POLARIZATION CONTROL

Several transmitarray have been presented in last section all aiming antenna beamsteering. However, transmitarray have also been used to control the polarization of the re-radiated EM, as the ones described as follows.

First introduced in [62] and further in [63], the authors have presented a transmitarray with the objective of controlling the polarization of the wavefront. The proposed structure is based on microstrip patch antennas, whose elements in the outer side of the structure are physically rotated ($\alpha = 0°$, $90°$, $180°$, and $270°$) relative to the patch feeding point), to tilt the polarization of the re-transmitted wave. The implemented unit-cells and the respective transmitarray are depicted in Fig. 17 [63]. The polarization of the re-radiated wave is forced by tilting mechanically of each unit-cell enabling the developed transmitarray to produce a circularly polarized wave. Since the polarization control is performed through sequential rotation and no other mechanism was implemented to automatically modify the properties of the transmitarray, rather than mechanical movement, the suggested model is considered a passive device.

Following the same approach, a novel passive transmitarray was latter introduced in [64] by the same research group.

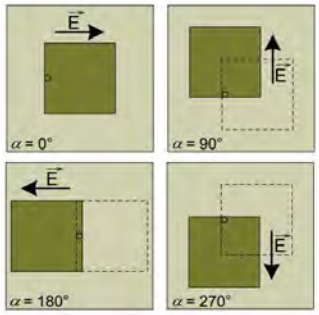

(a)

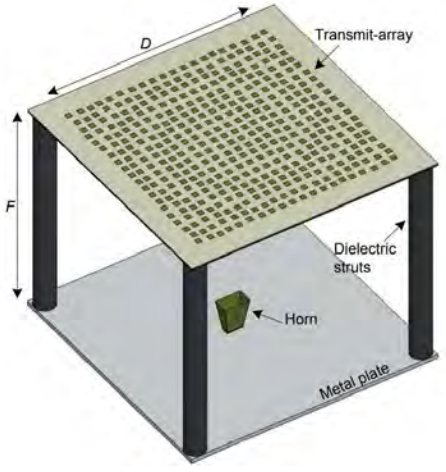

(b)

FIGURE 17: (a) Patch unit-cell and (b) transmitarray model for polarization control (images extracted from the work presented in [63]).

This particular device exhibits an enhanced unit-cell also based on microstrip patch with etched corners. A prototype of the device measured a broadside gain of 22.8 dBi at the simulated frequency with a 3 dB bandwidth of 20% in Right-hand Cross Polarization RHCP and 3 dB axial ratio with bandwidth of 24.4%.

With a novel unit-cell design and following a slightly different methodology, a novel transmitarray was introduced by *Pfeiffer* and *Grbic* in [65]. This design was implemented by using cascading metallic surfaces to provide polarization and wavefront control. Two transmitarray were developed and tested experimentally both based on a quarter-wave plate design that transforms a linearly polarized incident wave into a circularly polarized transmitted wave, by exploring the phase shift created between both faces of the structures. Since the phase difference between two orthogonal E-field components is a quarter of the wavelength ($90°$), when an incident field is linearly polarized at ($45°$) relative to its axes, the quarter-wave plate converts the transmitted field to circular polarization.

In [66] another polarization controlled transmitarray has been presented by stacking together several layers of rectangle ring slot unit-cells, separated by an air gap. Remarkably,

This article has been accepted for publication in a future issue of this journal, but has not been fully edited. Content may change prior to final publication. Citation information: DOI 10.1109/ACCESS.2019.2924293, IEEE Access

the proposed device is capable of realizing Left- and Right-hand cross polarizations (LHCP/RHCP), and linear polarization, when excited by a linearly polarized feeding source (*Vivaldi* antenna). This is achieved due to the enhanced phased control given by the stacked layers but also by varying the size of the unit-cell throughout the array. By varying the X and Y dimensions of the rectangle ring slot element, transmission magnitude and phase shift for both polarizations can be achieved. Therefore, it is possible to perform a change in polarization by adjusting the rotation angles of the feeding antenna through the phase of the linearly polarized incoming wave.

The main difference in the underlying principle between both physical rotated and phase delayed unit-cells is well detailed in [67]. The authors have presented a detailed comparison between both types of unit-cells through simulations and practical validation in two different transmitarray prototypes. Their study reveal that the transmitarray based on physically-rotated unit-cells exhibits wideband cross-polarization filtering characteristics, whereas the one with phase-shifted cells can offer polarization diversity (linear- and cross- polarization) with similar performance to the former, but limited by 3 dB axial-ratio bandwidth and magnitude of the feeding antenna [67].

After analyzing the presented examples, both loss and bandwidth may be considered the two major challenges in the design of a transmitarray. Hence, consideration to this aspect should be given at the time of selecting the design layout for a transmitarray implementation, given the project specifications. For example, in FSS-type transmitarray, bandwidth can be easily increased at the expense of using several stacked layers, as already mentioned. However, the overall insertion loss will always be proportional to the total number of layers (and on the properties of the substrate) and, thus, difficult to compensate. On the other hand, transmitarray with unit-cells composed of microstrip patches commonly exhibit limited bandwidth typically associated to such structures [1], but the insertion loss can be reduced by using amplifiers placed between the inner and the outer faces of the transmitarray. In fact, this technique has already been reported in [68]–[75], but particularly in [73], a total average gain of about 7.7 dB is reported for experiments on the unit-cell of Fig. 18, overcoming the initial insertion loss of 2.6 dB experienced without any signal amplification.

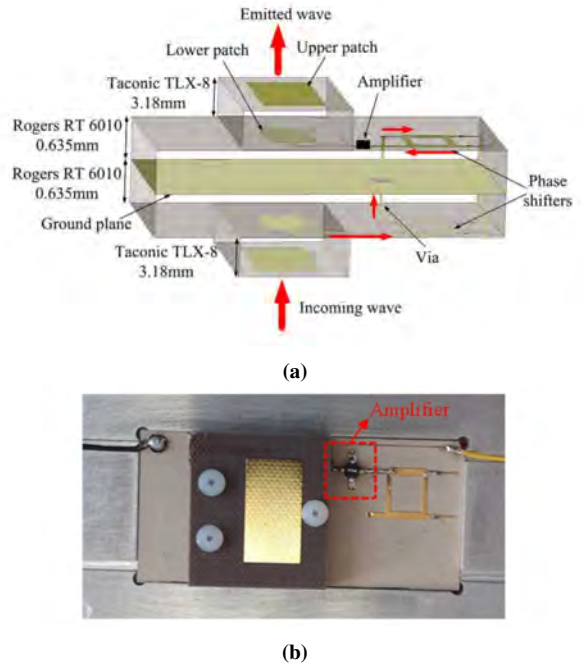

FIGURE 18: (a) Transmitarray unit-cell architecture and (b) photography of the unit-cell prototype (images extracted from the work presented in [73]).

C. HYBRID TRANSMITARRAY

Although the previous transmitarray designs [62]–[66] are not electronically reconfigurable (most are reconfigurable by mechanical rotation means), they yield to the development of hybrid reconfigurable transmitarray with both beamsteering and polarization capabilities.

It is the case of the reconfigurable transmitarray presented in [76] by *Huang, C. et. al.*. The authors have developed a transmitarray operating at 5.4 GHz with the capability of controlling electronically the polarization and direction of the re-radiated wave. Each unit-cell of the transmitarray is composed of several PCB layers separated by three different substrates, as depicted in Fig. 19. The face in which the electromagnetic wave is incident (Rx cell), a two-layer stacked patch is adopted. After being received by the Rx cell, the RF signal passes by two cascaded reflection type phase shifters and is coupled to the Transmitter cell (Tx cell) through a metallized via hole. Each of the phase shifter implemented integrate a four-port directional coupler and each port is loaded by a varactor-based tunable circuit in order to achieve the 360° phase tuning range. The Tx cell is made of a square patch with an O-slot structure loaded with two p-i-n diodes inserted along the x and y directions in order to control the polarization of the outgoing wave. According to simulations, the insertion loss of the unit-cell varies between 1.5 and 5 dB at frequencies around 5.4 GHz, and a cross-polarization ratio higher than 25 dB is obtained. The 8×8 transmitarray prototype is illustrated in Figs 19b and 19c. Experimental results demonstrate that this transmitarray is capable of achieving $\pm 60°$ in both azimuth and elevation planes, having a difference of 3.8 dB between the gain of the broadside beam and at the scan angle of 60°. Experimental results also show that this transmitarray is capable of producing an outgoing wave with circular polarization by controlling each of the p-i-n diodes independently.

In [77] yet another transmitarray with polarization control capabilities is presented by the same authors of [76], based on the unit-cell of Fig. 20. The authors have suggested two designs of unit-cells for 1-bit phase resolution transmitarray, to operate around 10 GHz. The most complete design pre-

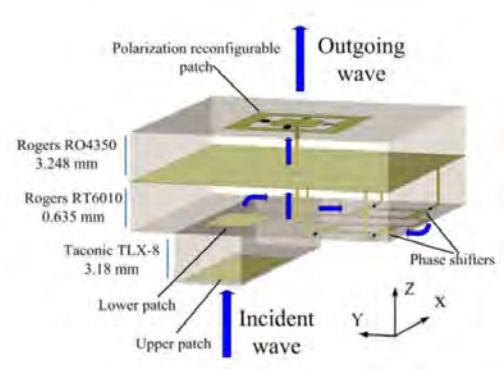

(a)

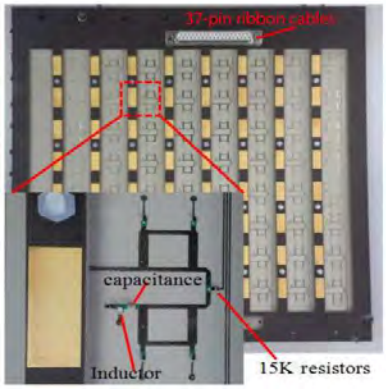

(b)

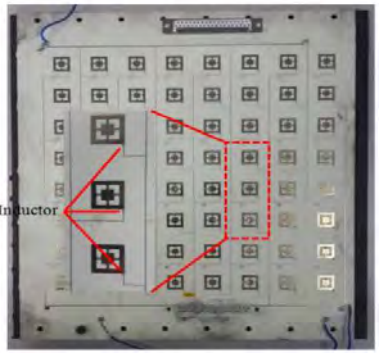

(c)

FIGURE 19: Transmitarray unit-cell architecture (image extracted from the work presented in [76]).

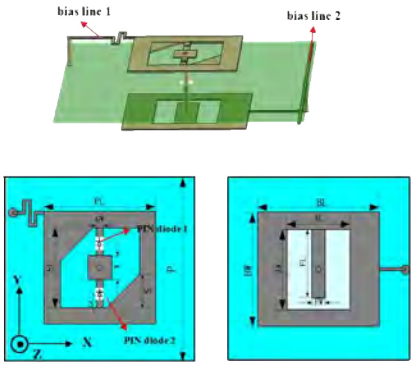

(a)

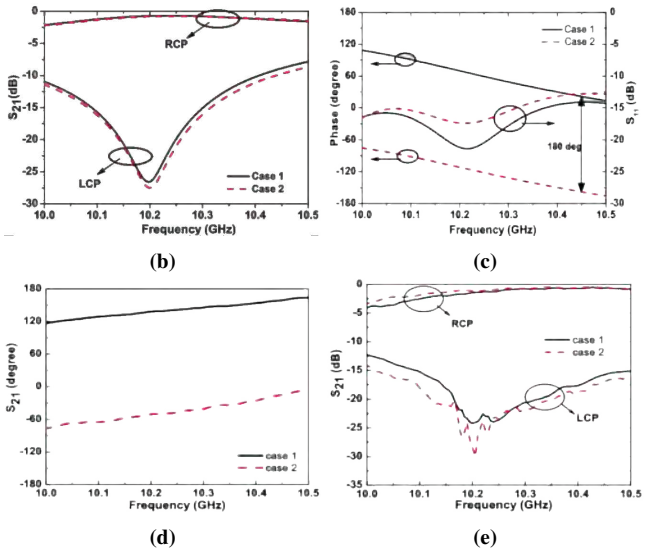

(b) (c) (d) (e)

FIGURE 20: (a) Transmitarray unit-cell design loaded with p-i-n diodes; S_{21} amplitude and phase response for: (b,c) simulated and (d,e) experimental results, respectively. (images extracted from the work presented in [77]).

sented by the authors consists of two-layer metallic patterns connected by a metallized via-hole as depicted in Fig. 20a. A U-slot rectangular patch is used in one side of the structure to receive the incident wave. On the other side, a square ring patch with two triangular corners and loaded with 2 p-i-n diodes is utilized to produce circular polarization. The p-i-n diodes were used to dynamically select between LHCP and RHCP. The unit-cell operates under two cases: case 1 - p-i-n diode 1 is switched on while 2 is off; case 2 - p-i-n diode 1 is switched off while 2 is on. Simulated results (Fig. 20b, Fig. 20c) on the unit-cell were further validated on a 8×8 transmitarray prototype against experimental results (Fig. 20d, Fig. 20e). While in case 1, the transmitarray converts a vertically polarized incident wave to RHCP, in case 2 the transmission phase of the outgoing wave is also shifted by $180°$. Based on the previous unit-cell design [77], the same research group have introduced and characterized in [78], a transmitarray with both reconfigurable polarization control and beamsteering capabilities. Besides of controlling the polarization of the re-transmitted EM wave, the proposed transmitarray also has the capability of realising beamsteering in a range of $\pm 45°$ in both elevation an azimuth planes at 4.8 GHz, exhibiting however insertion losses of 5.6 dB over a small bandwidth of 100 MHz, obtained experimentally on a manufactured prototype.

Similarly in [79], it has been presented a 20×20 element fully reconfigurable transmitarray based on a 1-bit linear polarization unit-cell model operating in the Ka-band (27-GHz). A snapshot of both unit-cells and the reconfigurable transmitarray are depicted in Fig. 21. The unit-cell is formed in a multi-layer design with a central ground plane (Fig. 21a)

This article has been accepted for publication in a future issue of this journal, but has not been fully edited. Content may change prior to final publication. Citation information: DOI 10.1109/ACCESS.2019.2924293, IEEE Access

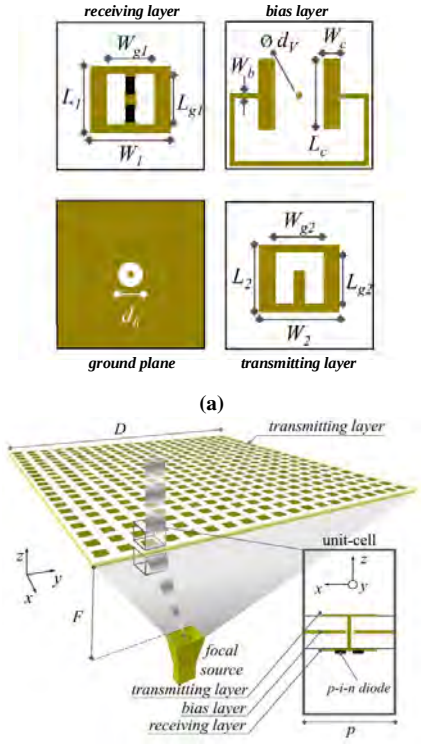

FIGURE 21: Snapshot of (a) the active unit-cell and (b) transmitarray for beamsteering and polarization control (images extracted from the work presented in [79]).

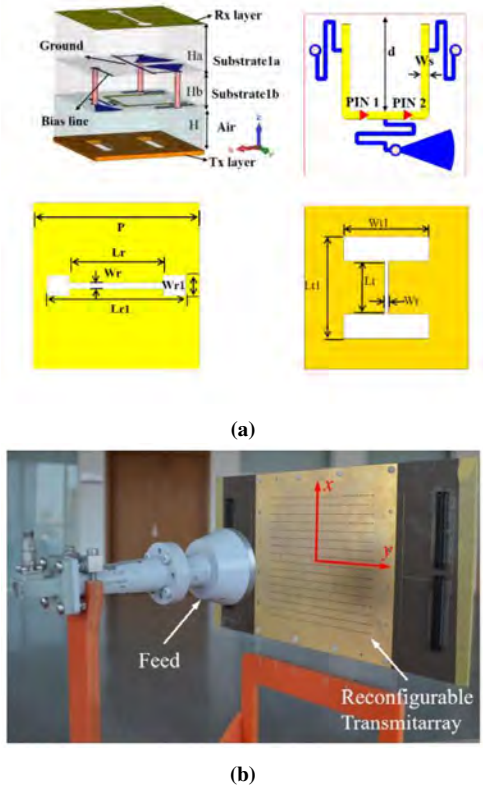

FIGURE 22: (a) Geometry of the transmitarray element and (b) reconfigurable transmitarray prototype with 16×16 elements (images extracted from the work presented in [80]).

loaded with p-i-n diodes to obtain a wide-band constant phase shift between the two phase states. Circular polarization is achieved by using the sequential rotation technique previously described, while p-i-n diodes enable LHCP / RHCP polarization switching. However, due to the control of the phase shift by switching on and off the p-i-n diodes, the control of the direction of the out-coming wave is also possible with reported steering ranges of $\pm 60^\circ$ in azimuth and elevation planes.

Finally, in [80] a 1-bit reconfigurable transmitarray that allows control of polarization as well as antenna beamsteering is presented. The unit-cell of the transmitarray is comprised of two H-shaped slots (Fig. 22a) that behave as receiving and transmitting coupled microstrip patches. The fact that they are orthogonality disposed relative to each other, it allows *X* to *Y* polarization transformation (of the incident EM wave). In between the transmitter and receiver slot patches, a feeding network that includes 2 p-i-n diodes is responsible to control the phase difference of the arrangement. When the p-i-n diode 1 is OFF and p-i-n diode 2 is ON (Fig. 22a), a total phase shift of 180° is achieved against 0° phase shift for the opposite case. The proposed unit-cell operates at a center frequency of 12.5 GHz and it has an overall dimension of $8 \times 8\ mm^2$ ($\lambda/3 \times \lambda/3$). According to simulation on the unit-cell, the -10 dB S_{11} bandwidth is of 300 MHz for both working cases, with maximum of 0.86 dB of insertion losses (for the case where D1=OFF/D2=ON). The isolation between co- and cross-polarizations is 16.5 dB for the center frequency.

Subsequent to the unit-cell characterization, a 16×16 transmitarray prototype has been fabricated and measured. It is composed of 256 individual cells leading to a total of 512 p-i-n diodes to achieve both phase and angular reconfigurability. A *x-polarized* horn feed is used to illuminate the transmitarray as shown in Fig. 22b. With the presented setup, a total of $\pm 50^\circ$ beamsteering is obtained for both elevation and azimuth planes.

It should be noted that some authors consider that the transmitarray are placed at a distance far away from the radiation source aperture (focal distance), whereas others are considered at the vicinity of the antenna source aperture. The ones that are placed at the right focal distance typically exhibit wide beamsteering ranges, since the placement at the focal distance leads to better spillover and illumination efficiencies.

In fact, this is well reported in [81] where the authors have developed a flat lens exhibiting circular polarization and wide beamsteering angular ranges (Fig. 23). In particular, the focal seems to play distance play an important role in radiation performance, since larger distances tend to reduce aberration and consequently lower beam distortions and improve side-lobe levels. To this end, the authors in [81] have

This article has been accepted for publication in a future issue of this journal, but has not been fully edited. Content may change prior to final publication. Citation information: DOI 10.1109/ACCESS.2019.2924293, IEEE Access

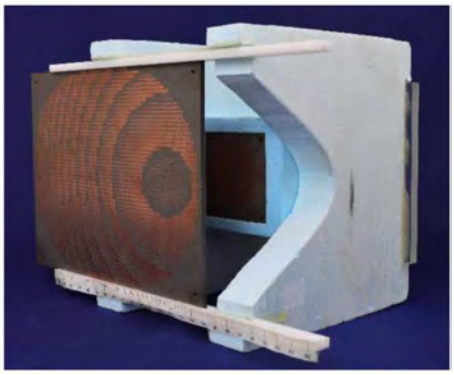

(a)

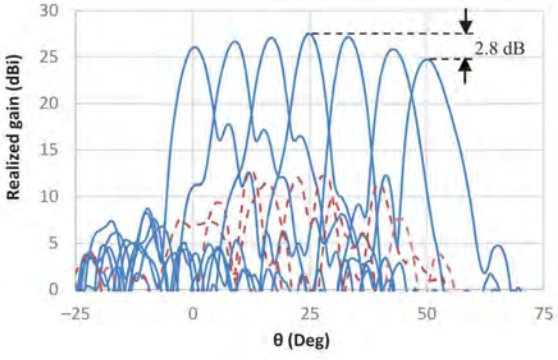

(b)

FIGURE 23: (a) Antenna prototype and (b) measured realized gain for several beamsteering angles between 0° and 50° (images extracted from the work presented in [81]).

proposed a new feeding technique by implementing a virtual focus using a dual-lens configuration, in order to reduce the overall antenna height. Remarkably, beamsteering angles up to $\pm 50^\circ$, at Ka-band (30 GHz) with an antenna height estimated to be reduced by 20%, due to the virtual focus, has been achieved. In fact, this is different technique to those previously presented, in which a lens-like phase pattern, by means of microstrip patches, is used for beamsteering.

The closer the feed, the higher the oblique incident angle, which in turn affects negatively the illumination efficiency and thus overall steering ranges.However, the transmitarray placed right next to antenna aperture also showed to processing results with the advantage of reducing the overall size of the apparatus.

The references presented in this review of the literature are summarized in Table 1, listed by their main feature (polarization control and beamsteering), mode of operation (P - passive, A - active), unit-cell (UC) design format and size, reconfigurability control mechanism, frequency of operation, bandwidth, insertion losses and beamsteering angular ranges with respective steering planes, when applicable.

IV. CONCLUSIONS

.

This paper presents an extensive literature review addressing antenna beamsteering by using transmitarray. A fundamental overview on the concept of 1D and 2D beamsteering using a transmitarray is presented. With this, it was verified that to perform beamsteering with a transmitarray, the phase in each transmitarray element must be varied, progressively and equally, throughout the entire array much like a phased antenna array. Subsequently, a dedicated literature review is outlined starting with transmitarray developed for antenna beamsteering, wavefront polarization control, and transmitarray that combine both features simultaneity. Particular emphasis is given to active/reconfigurable transmitarray, *i.e.* devices with the capability of having its characteristics electronically controlled, either by employing active mechanisms as p-i-n diodes, varactor diodes or MEMS switches. Several examples among the literature have been presented and compared, followed by a critical review. Information about unit-cell main characteristics are disseminated including, design layout, *e.g.* if based on FSS, MM or microstrip patch antennas. Finally, all this information is summarized in terms of useful technical data extracted from the literature such as, frequency of operation, bandwidth, unit/cell dimensions, insertion loss and maximum steering ranges. This review paper demonstrates that transmitarray antennas can be seen as a feasible alternative to the most traditional techniques of beamsteering, overcoming some of its limitations, e.g. it withdraws the requirements of complex beamsteering networks of phased antenna arrays. Since transmitarray are mostly employing using PCB techniques, they will significantly reduce weight, power consumption and the dimensions of assemblies, making them very attractive for inclusion in a large number of applications. Future work may address study of new methods to increase beamsteering ranges, e.g. using conformal transmitarray, while enabling finer angular resolution, polarization control (for polarimetric applications) and beam (de)focusing. New reconfigurable unit-cell designs is of paramount importance to overcome existing limitations, as outlined in this paper, in terms of bandwidth, insertion losses and phase ranges. Of utterly importance is also the extension of the supporting technology from PCB to system on chip (SoC), being one forward leap from vertical (stacked) integration of layers to save space and improve on the massive integration of active components, whilst exploring new designs based on novel electronic biasing (tunable) metamaterials. Finally, beamsteering based on transmitarray is currently well perceived as one of the most important key enabling technologies to achieve multi-gigabit/s peak data rates in mobile radio channels. Emerging 5G systems and beyond may encompass fundamentally new transmitarray designs targeting micro- and millimeter-wave frequencies, small form factors and light-weight solutions, enabling the development of new agile beamsteering and user tracking algorithms."

REFERENCES

[1] C. A. Balanis, Antenna Theory: Analysis and Design, 3rd Edition. John Wiley & Sons, 2005, vol. 72.

[2] R. J. Mailloux, Phased Array Antenna Handbook. Artech House,

TABLE 1: Summary table of references for polarization control (Pol.) and beamsteering (BS) transmitarrays

Ref.	Feature	Mode†	UC type	UC size	Control mechanism	Freq. band	Bandwidth	Loss	BS Range
[37]	BS	A	microstrip patch	n/a	varactor	12 GHz	700 MHz	3 dB	$+9°(Az\ only)$
[38], [39]		A	microstrip patch	$0.55\lambda \times 0.55\lambda$	varactor	5.7 GHz	n/a	4.8dB	$\pm 25°\star(Az\ or\ El)$
[40]		A	coupled feed patch	$0.55\lambda \times 0.55\lambda$*	varactor	5 GHz*	500 MHz*	3.6 dB*	n/a
[41]		A	coupled feed patch	$0.55\lambda \times 0.55\lambda$	varactor	5 GHz	500 MHz	2.2 dB	$\pm 50°\star(Az\ and\ El)$
[42]–[44]		A	microstrip patch	$0.5\lambda \times 0.5\lambda$	p-i-n (and MEMS)	10 GHz	1.5 GHz	3 dB	$\pm 70°(Az)\ and\ \pm 40°(El)$
[45]		A	O-slot rectangular patch	$\lambda/2 \times \lambda/2$	p-i-n	29 GHz	n/a	n/a	$\pm 40°\star(Az\ only)$
[46]		A	microstrip patch	n/a	varactor diodes	24.6 GHz	1 GHz	17 dB	$\pm 50°(Az\ and\ El)$
[14]		A	metamaterials	n/a	liquid crystal	27.5 GHz	n/a	5 dB	$\pm 5°(Az\ only)$
[47]		A	metamaterials	$0.17\lambda \times 0.17\lambda$	varactor	1.7 GHz	n/a	4 dB	$\pm 30°\star(Az\ only)$
[48]		A	metamaterials	$0.61\lambda \times 0.61\lambda$	varactor	4.7 GHz	250 MHz	n/a	$\pm 30°\star(Az\ only)$
[49]–[51]		A	freq. selective surface	$0.5\lambda \times 0.5\lambda$*	varactor	4 GHz*	400 MHz*	3 dB*	n/a
[52]		A	freq. selective surface	$0.58\lambda \times 0.58\lambda$	varactor	5.3 GHz	180 MHz	6.5 dB	$\pm 30°\star(Az\ or\ El)$
[53]		A	freq. selective surface	$\lambda/25 \times \lambda/25$	tunable ferroelectric film	12 GHz	n/a	2.9 dB	$\pm 10°(Az\ only)$
[54]		P	freq. selective surface	$0.17\lambda \times 0.17\lambda$	discrete capacitors	5.35 GHz	110 MHz	2.8 dB	$\pm 25°(Az\ and\ El)$
[55]		A	freq. selective surface	$0.17\lambda \times 0.17\lambda$	varactor	5.2 GHz	70 MHz	4.3 dB	$\pm 28°(Az)\ and\ \pm 26°(El)$
[56]		A	freq. selective surface	$0.54\lambda \times 0.54\lambda$	p-i-n	11.5 GHz	n/a	n/a	$\pm 40°(Az\ and\ El)$
[62], [63]	Pol	P	microstrip patch	$0.5\lambda \times 0.5\lambda$*	cell rotation	60 GHz*	5.6 GHz*	0.46 dB*	n/a
[64]		P	microstrip patch	$0.5\lambda \times 0.5\lambda$	cell rotation	30 GHz	6.5 GHz	n/a	n/a
[65]		P	multi-layer PCB	$0.28\lambda \times 0.28\lambda$	cascading surfaces	77 GHz	13 GHz	n/a	n/a
[66]		P	cascaded rectangle ring slot	$0.6\lambda \times 0.6\lambda$	feeding source rotation	6 GHz	1.8 GHz	n/a	n/a
[76]	Hybrid (BS & Pol)	A	square patch	$0.482\lambda \times 0.482\lambda$	varactor (and p-i-n)	5.4 GHz	450 MHz	3.8 dB	$\pm 60°(Az\ and\ El)$
[77]		A	U-slot patch	$0.47\lambda \times 0.47\lambda$	p-i-n	10 GHz	320 MHz	1.4 dB	n/a
[78]		A	U-slot coupled feed patch	$0.488\lambda \times 0.488\lambda$	p-i-n	4.8 GHz	100 MHz	5.6 dB	$\pm 45°(Az\ and\ El)$
[79]		A	rectangle ring slot	$0.46\lambda \times 0.46\lambda$	p-i-n	27 GHz	4.2 GHz	3 dB	$\pm 60°(Az\ and\ El)$
[80]		A	U-shaped microstrip line	$\lambda/3 \times \lambda/3$	p-i-n	12.5 GHz	300 MHz	5 dB	$\pm 50°(Az\ and\ El)$
[81]		P	dual layer microstrip patch	$\lambda/3 \times \lambda/3$	n/a	30 GHz	2 GHz	n/a	$\pm 50°(El)$

† modes for unit-cells: P - passive, A - active (reconfigurable);
* considering the best case of 2 proposed designs;
⋆ steering range with SLL<12dB;
n/a - not available.

Incorporated, 2005.

[3] A. Bhattacharyya, Phased Array Antennas: Floquet Analysis, Synthesis, Bfns and Active Array Systems, ser. Wiley Series in Microwave and Optical Engineering. Wiley, 2006.

[4] D. McGrath, "Planar Three-Dimensional Constrained Lenses," IEEE Transactions on Antennas and Propagation, vol. 34, no. 1, pp. 46–50, Jan 1986.

[5] J. Y. Lau, "Reconfigurable Transmitarray Antennas," Ph.D. dissertation, University of Toronto, 2012.

[6] L. D. Palma, "Reconfigurable Transmitarray Antennas at Millimeter-Wave Frequencies," Ph.D., 2015.

[7] S. Hum and J. Perruisseau-Carrier, "Reconfigurable Reflectarrays and Array Lenses for Dynamic Antenna Beam Control: A Review," IEEE Transactions on Antennas and Propagation, vol. 62, no. 1, pp. 183–198, Jan 2014.

[8] F. Capolino, Applications of Metamaterials. CRC Press, 2009.

[9] C. Balanis, Advanced Engineering Electromagnetics, ser. CourseSmart Series. Wiley, 2012.

[10] J. Vardaxoglou, Frequency Selective Surfaces: Analysis and Design. Research Studies Press, 1997.

[11] B. A. Munk, Frequency Selective Surfaces: Theory and Design. John Wiley & Sons, 2005.

[12] K. Sarabandi and N. Behdad, "A Frequency Selective Surface With Miniaturized Elements," IEEE Transactions on Antennas and Propagation, vol. 55, no. 5, pp. 1239–1245, May 2007.

[13] D. Ferreira, R. Caldeirinha, I. Cuiñas, and T. Fernandes, "Square Loop and Slot Frequency Selective Surfaces Study for Equivalent Circuit Model Optimization," IEEE Transactions on Antennas and Propagation, vol. 63, no. 9, pp. 3947–3955, Sept 2015.

[14] M. Maasch, M. Roig, C. Damm, and R. Jakoby, "Voltage-tunable artificial gradient-index lens based on a liquid crystal loaded fishnet metamaterial," IEEE Antennas and Wireless Propagation Letters, vol. 13, pp. 1581–1584, 2014.

[15] Y. Huang, L. Wu, M. Tang, and J. Mao, "Design of a Beam Reconfigurable THz Antenna With Graphene-Based Switchable High-Impedance Surface," IEEE Transactions on Nanotechnology, vol. 11, no. 4, pp. 836–842, July 2012.

[16] E. Carrasco, M. Tamagnone, and J. Perruisseau-Carrier, "Tunable Graphene-based Reflectarray Element for Reconfigurable Beams," in 2013 7th European Conference on Antennas and Propagation (EuCAP), April 2013, pp. 1779–1782.

[17] H. A. Malhat, S. H. Zainud-Deen, and S. M. Gaber, "Circularly Polarized Graphene Based Transmitarray for Terahertz Applications," in 2014 XXXIth URSI General Assembly and Scientific Symposium (URSI GASS), Aug 2014, pp. 1–4.

[18] W. M. Hassan, S. H. Zainud-Deen, and H. A. Malhat, "Compact Multifunction Single/dual-beam Graphene Lens Antenna for Terahertz Applications," in 2016 33rd National Radio Science Conference (NRSC), Feb 2016, pp. 41–48.

[19] W. M. Hassan, "Multilayer Graphene-only Transmitarray Antenna (MGOT) for Terahertz Applications," in 2017 34th National Radio Science Conference (NRSC), March 2017, pp. 43–48.

[20] W. Yao, L. Tang, J. Wang, C. Ji, X. Wei, and Y. Jiang, "Spectrally and Spatially Tunable Terahertz Metasurface Lens Based on Graphene Surface Plasmons," IEEE Photonics Journal, vol. 10, no. 4, pp. 1–8, Aug 2018.

[21] A. Moessinger, R. Marin, S. Mueller, J. Freese, and R. Jakoby, "Electronically reconfigurable reflectarrays with nematic liquid crystals," Electronics Letters, vol. 42, no. 16, pp. 899–900, August 2006.

[22] G. Perez-Palomino, J. A. Encinar, M. Barba, and E. Carrasco, "Design and Evaluation of Multi-resonant Unit Cells Based on Liquid Crystals for Reconfigurable Reflectarrays," IET Microwaves, Antennas Propagation, vol. 6, no. 3, pp. 348–354, February 2012.

[23] S. Bildik, S. Dieter, C. Fritzsch, W. Menzel, and R. Jakoby, "Reconfigurable Folded Reflectarray Antenna Based Upon Liquid Crystal Technology," IEEE Transactions on Antennas and Propagation, vol. 63, no. 1, pp. 122–132, Jan 2015.

[24] G. Perez-Palomino, M. Barba, J. A. Encinar, R. Cahill, R. Dickie, P. Baine, and M. Bain, "Design and demonstration of an electronically scanned reflectarray antenna at 100 ghz using multiresonant cells based on liquid crystals," IEEE Transactions on Antennas and Propagation, vol. 63, no. 8, pp. 3722–3727, Aug 2015.

[25] Y. Zhao, C. Huang, A. Qing, and X. Luo, "A Frequency and Pattern Reconfigurable Antenna Array Based on Liquid Crystal Technology," IEEE Photonics Journal, vol. 9, no. 3, pp. 1–7, June 2017.

[26] B. Che, T. Jin, D. Erni, F. Meng, Y. Lyu, and Q. Wu, "Electrically controllable composite right/left-handed leaky-wave antenna using liquid crystals in pcb technology," IEEE Transactions on Components, Packaging and Manufacturing Technology, vol. 7, no. 8, pp. 1331–1342, Aug 2017.

[27] S. F. Jilani, M. O. Munoz, Q. H. Abbasi, and A. Alomainy, "Millimeter-Wave Liquid Crystal Polymer Based Conformal Antenna Array for 5G Applications," IEEE Antennas and Wireless Propagation Letters, vol. 18, no. 1, pp. 84–88, Jan 2019.

[28] S. H. Lee, M. Choi, T.-T. Kim, S. Lee, M. Liu, X. Yin, H. K. Choi, S. S. Lee, C.-G. Choi, S.-Y. Choi, X. Zhang, and B. Min, "Switching terahertz waves with gate-controlled active graphene metamaterials," Nature Materials, vol. 11, pp. 936 EP –, Sep 2012. [Online]. Available: https://doi.org/10.1038/nmat3433

[29] C. Núñez Álvarez, R. Cheung, and J. S. Thompson, "Performance Analysis of Hybrid Metal–Graphene Frequency Reconfigurable Antennas in the Microwave Regime," IEEE Transactions on Antennas and Propagation, vol. 65, no. 4, pp. 1558–1569, April 2017.

[30] J. Shaker, M. R. Chaharmir, and J. Ethier, Reflectarray Antennas: Analysis, Design, Fabrication, and Measurement. Artech House, 2013, vol. 1.

[31] J. Huang and J. A. Encinar, Reflectarray Antennas. John Wiley & Sons, 2007, vol. 9.

[32] D. M. Pozar, S. D. Targonski, and H. Syrigos, "Design of Millimeter Wave Microstrip Reflectarrays," IEEE Transactions on Antennas and Propagation, vol. 45, no. 2, pp. 287–296, Feb 1997.

[33] D. Sievenpiper, J. Schaffner, R. Loo, G. Tangonan, S. Ontiveros, and R. Harold, "A Tunable Impedance Surface Performing as a Reconfigurable Beam Steering Reflector," IEEE Transactions on Antennas and Propagation, vol. 50, no. 3, pp. 384–390, Mar 2002.

[34] D. Sievenpiper and J. Schaffner, "Beam Steering Microwave Reflector Based on Electrically Tunable Impedance Surface," Electronics Letters, vol. 38, no. 21, pp. 1237–1238, Oct 2002.

[35] E. Carrasco, M. Barba, B. Reig, C. Dieppedale, and J. Encinar, "Characterization of a Reflectarray Gathered Element With Electronic Control Using Ohmic RF MEMS and Patches Aperture-Coupled to a Delay Line," IEEE Transactions on Antennas and Propagation, vol. 60, no. 9, pp. 4190–4201, Sept 2012.

[36] E. Carrasco, M. Barba, and J. Encinar, "X-Band Reflectarray Antenna With Switching-Beam Using PIN Diodes and Gathered Elements," IEEE Transactions on Antennas and Propagation, vol. 60, no. 12, pp. 5700–5708, Dec 2012.

[37] P. Padilla, A. Munoz-Acevedo, M. Sierra-Castaner, and M. Sierra-Perez, "Electronically Reconfigurable Transmitarray at Ku Band for Microwave Applications," IEEE Transactions on Antennas and Propagation, vol. 58, no. 8, pp. 2571–2579, Aug 2010.

[38] J. Y. Lau and S. V. Hum, "Analysis and Characterization of a Multipole Reconfigurable Transmitarray Element," IEEE Transactions on Antennas and Propagation, vol. 59, no. 1, pp. 70–79, Jan 2011.

[39] J. Lau and S. Hum, "A Planar Reconfigurable Aperture With Lens and Reflectarray Modes of Operation," IEEE Transactions on Microwave Theory and Techniques, vol. 58, no. 12, pp. 3547–3555, Dec 2010.

[40] ——, "A Wideband Reconfigurable Transmitarray Element," IEEE Transactions on Antennas and Propagation, vol. 60, no. 3, pp. 1303–1311, March 2012.

[41] ——, "Reconfigurable Transmitarray Design Approaches for Beamforming Applications," IEEE Transactions on Antennas and Propagation, vol. 60, no. 12, pp. 5679–5689, Dec 2012.

[42] A. Clemente, L. Dussopt, R. Sauleau, P. Potier, and P. Pouliguen, "1-bit Reconfigurable Unit Cell Based on PIN Diodes for Transmit-array Applications in X-band," IEEE Transactions on Antennas and Propagation, vol. 60, no. 5, pp. 2260–2269, May 2012.

[43] A. Clemente, L. Dussopt, B. Reig, R. Sauleau, P. Potier, and P. Pouliguen, "Reconfigurable Unit-cells for Beam-scanning Transmitarrays in X Band," in 2013 7th European Conference on Antennas and Propagation (EuCAP), April 2013, pp. 1783–1787.

[44] A. Clemente, L. Dussopt, R. Sauleau, P. Potier, and P. Pouliguen, "Wideband 400-Element Electronically Reconfigurable Transmitarray in X Band," IEEE Transactions on Antennas and Propagation, vol. 61, no. 10, pp. 5017–5027, Oct 2013.

[45] F. Diaby, A. Clemente, L. D. Palma, L. Dussopt, K. Pham, E. Fourn, and R. Sauleau, "Design of a 2-bit unit-cell for electronically reconfigurable transmitarrays at ka-band," in 2017 47th European Microwave Conference (EuMC). IEEE, oct 2017.

[46] M. Frank, F. Lurz, R. Weigel, and A. Koelpin, "Electronically reconfigurable 6 × 6 element transmitarray at k band based on unit-cells with continuous phase range," IEEE Antennas and Wireless Propagation Letters, pp. 1–1, 2019.

[47] Y. Sun, Z. Li, W. Zhu, Z. Ji, and Q. Wang, "New Steerable Antenna with Controllable Metamaterial," in EuMC 2012 European Microwave Conference, Oct 2012, pp. 936–939.

[48] T. Jiang, Z. Wang, D. Li, J. Pan, B. Zhang, J. Huangfu, Y. Salamin, C. Li, and L. Ran, "Low-DC Voltage-Controlled Steering-Antenna Radome Utilizing Tunable Active Metamaterial," IEEE Transactions on Microwave Theory and Techniques, vol. 60, no. 1, pp. 170–178, Jan. 2012.

[49] I. Russo, D. Gaetano, L. Boccia, G. Amendola, and G. Di Massa, "Investigation on the Transmission Beam-Steering Capabilities of Tunable Impedance Surfaces," in EuMC 2009 European Microwave Conference, Sept 2009, pp. 1033–1036.

[50] I. Russo, L. Boccia, G. Amendola, and G. Di Massa, "Tunable Pass-band FSS for Beam Steering Applications," in 2010 Proceedings of the Fourth European Conference on Antennas and Propagation (EuCAP), April 2010, pp. 1–4.

[51] L. Boccia, I. Russo, G. Amendola, and G. Di Massa, "Multilayer Antenna-Filter Antenna for Beam-Steering Transmit-Array Applications," IEEE Transactions on Microwave Theory and Techniques, vol. 60, no. 7, pp. 2287–2300, July 2012.

[52] W. Pan, C. Huang, P. Chen, M. Pu, X. Ma, and X. Luo, "A Beam Steering Horn Antenna Using Active Frequency Selective Surface," IEEE Transactions on Antennas and Propagation, vol. 61, no. 12, pp. 6218–6223, Dec 2013.

[53] M. Sazegar, Y. Zheng, C. Kohler, H. Maune, M. Nikfalazar, J. Binder, and R. Jakoby, "Beam Steering Transmitarray Using Tunable Frequency Selective Surface With Integrated Ferroelectric Varactors," IEEE Transactions on Antennas and Propagation, vol. 60, no. 12, pp. 5690–5699, Dec 2012.

[54] J. R. Reis, N. Copner, A. Hammoudeh, Z. M. E. Al-Daher, R. F. S. Caldeirinha, T. R. Fernandes, and R. Gomes, "FSS-Inspired Transmitarray for Two-Dimensional Antenna Beamsteering," IEEE Transactions on Antennas and Propagation, vol. 64, no. 6, pp. 2197–2206, June 2016.

[55] J. R. Reis, R. F. S. Caldeirinha, A. Hammoudeh, and N. Copner, "Electronically Reconfigurable FSS-Inspired Transmitarray for 2-D Beamsteering," IEEE Transactions on Antennas and Propagation, vol. 65, no. 9, pp. 4880–4885, Sept 2017.

[56] B. D. Nguyen and C. Pichot, "Unit-cell loaded with PIN diodes for 1-bit linearly polarized reconfigurable transmitarrays," IEEE Antennas and Wireless Propagation Letters, vol. 18, no. 1, pp. 98–102, jan 2019.

[57] G. Masters and S. Gregson, "Coordinate System Plotting for Antenna Measurements," AMTA Symposium, 2007.

[58] C. G. Ryan, M. Chaharmir, J. Shaker, J. Bray, Y. Antar, and A. Ittipiboon, "A Wideband Transmitarray Using Dual-Resonant Double Square Rings," IEEE Transactions on Antennas and Propagation, vol. 58, no. 5, pp. 1486–1493, May 2010.

[59] A. Edalati and T. Denidni, "Beam-switching Antenna Based on Active Frequency Selective Surfaces," in 2011 IEEE International Symposium on Antennas and Propagation (APSURSI), July 2011, pp. 2254–2257.

[60] H. Zhou, S. Qu, B. Lin, J. Wang, H. Ma, Z. Xu, W. Peng, and P. Bai, "Filter-Antenna Consisting of Conical FSS Radome and Monopole Antenna," IEEE Transactions on Antennas and Propagation, vol. 60, no. 6, pp. 3040–3045, June 2012.

[61] M. Niroo-Jazi and T. Denidni, "Electronically Sweeping-Beam Antenna Using a New Cylindrical Frequency-Selective Surface," IEEE Transactions on Antennas and Propagation, vol. 61, no. 2, pp. 666–676, Feb 2013.

[62] H. Kaouach, L. Dussopt, J. Lanteri, T. Koleck, and R. Sauleau, "Circularly-polarized Discrete Lens Antennas in the 60-GHz Band," in 2010 Conference Proceedings ICECom, Sept 2010, pp. 1–4.

[63] L. Dussopt, H. Kaouach, J. Lanteri, and R. Sauleau, "Circularly-polarized Discrete Lens Antennas in the 60-GHz Band," in Radio Engineering, vol. 20, Dec 2011, pp. 733–738.

[64] L. D. Palma, A. Clemente, L. Dussopt, R. Sauleau, P. Potier, and P. Pouliguen, "Circularly Polarized Transmitarray With Sequential Rotation in Ka-Band," IEEE Transactions on Antennas and Propagation, vol. 63, no. 11, pp. 5118–5124, Nov 2015.

[65] C. Pfeiffer and A. Grbic, "Millimeter-Wave Transmitarrays for Wavefront and Polarization Control," IEEE Transactions on Microwave Theory and Techniques, vol. 61, no. 12, pp. 4407–4417, Dec 2013.

[66] X. Zhong, L. Chen, Y. Shi, and X. Shi, "Design of Multiple-Polarization Transmitarray Antenna Using Rectangle Ring Slot Elements," IEEE Antennas and Wireless Propagation Letters, vol. 15, pp. 1803–1806, 2016.

[67] P. Naseri, S. A. Matos, J. R. Costa, and C. A. Fernandes, "Phase-Delay Versus Phase-Rotation Cells for Circular Polarization Transmit Arrays - Application to Satellite Ka-Band Beam Steering," IEEE Transactions on Antennas and Propagation, vol. 66, no. 3, pp. 1236–1247, March 2018.

[68] S. Hollung, A. E. Cox, and Z. B. Popovic, "A Bi-directional Quasi-optical Lens Amplifier," IEEE Transactions on Microwave Theory and Techniques, vol. 45, no. 12, pp. 2352–2357, Dec 1997.

[69] E. W. Bryerton, M. D. Weiss, and Z. Popovic, "A 10-GHz High-efficiency Lens Amplifier Array," in 1998 IEEE MTT-S International Microwave

Symposium Digest (Cat. No.98CH36192), vol. 3, June 1998, pp. 1461–1464 vol.3.

[70] S. C. Ortiz, T. Ivanov, and A. Mortazawi, "A Cpw-fed Microstrip Patch Quasi-optical Amplifier Array," IEEE Transactions on Microwave Theory and Techniques, vol. 48, no. 2, pp. 276–280, Feb 2000.

[71] H. J. Song and M. E. Bialkowski, "Transmit Array of Transistor Amplifiers Illuminated by a Patch Array in the Reactive Near-field Region," IEEE Transactions on Microwave Theory and Techniques, vol. 49, no. 3, pp. 470–475, March 2001.

[72] S. C. Ortiz, J. Hubert, L. Mirth, E. Schlecht, and A. Mortazawi, "A High-power Ka-band Quasi-optical Amplifier Array," IEEE Transactions on Microwave Theory and Techniques, vol. 50, no. 2, pp. 487–494, Feb 2002.

[73] W. Pan, C. Huang, X. Ma, and X. Luo, "An amplifying tunable transmitarray element," IEEE Antennas and Wireless Propagation Letters, vol. 13, pp. 702–705, 2014.

[74] N. Landsberg and E. Socher, "Multi-level Ask Spatial Modulators Employing a 100 GHz Lens-array Antenna and 65 nm CMOS," in 2016 46th European Microwave Conference (EuMC), Oct 2016, pp. 429–432.

[75] ——, "Design and Measurements of 100 GHz Reflectarray and Transmitarray Active Antenna Cells," IEEE Transactions on Antennas and Propagation, vol. 65, no. 12, pp. 6986–6997, Dec 2017.

[76] C. Huang, W. Pan, X. Ma, B. Zhao, J. Cui, and X. Luo, "Using Reconfigurable Transmitarray to Achieve Beam-Steering and Polarization Manipulation Applications," IEEE Transactions on Antennas and Propagation, vol. 63, no. 11, pp. 4801–4810, Nov 2015.

[77] C. Huang, W. Pan, X. Ma, and X. Luo, "1-Bit Reconfigurable Circularly Polarized Transmitarray in X-Band," IEEE Antennas and Wireless Propagation Letters, vol. 15, pp. 448–451, 2016.

[78] C. Huang, W. Pan, and X. Luo, "Low-Loss Circularly Polarized Transmitarray for Beam Steering Application," IEEE Transactions on Antennas and Propagation, vol. 64, no. 10, pp. 4471–4476, Oct 2016.

[79] L. D. Palma, A. Clemente, L. Dussopt, R. Sauleau, P. Potier, and P. Pouliguen, "Circularly-Polarized Reconfigurable Transmitarray in Ka-Band With Beam Scanning and Polarization Switching Capabilities," IEEE Transactions on Antennas and Propagation, vol. 65, no. 2, pp. 529–540, Feb 2017.

[80] M. Wang, S. Xu, F. Yang, and M. Li, "Design and measurement of a 1-bit reconfigurable transmitarray with sub-wavelength h-shaped coupling slot elements," IEEE Transactions on Antennas and Propagation, pp. 1–1, 2019.

[81] E. B. Lima, S. A. Matos, J. R. Costa, C. A. Fernandes, and N. J. G. Fonseca, "Circular polarization wide-angle beam steering at ka-band by in-plane translation of a plate lens antenna," IEEE Transactions on Antennas and Propagation, vol. 63, no. 12, pp. 5443–5455, Dec 2015.

JOAO R. REIS was born in Lisbon, Portugal, in 1987. He received the undergraduate degree in Electrical Engineering, Electronics & Telecommunications, from the School of Technology and Management (ESTG) of the Polytechnic Institute of Leiria (IPL), Portugal, in 2010. In 2018, he was awarded a Ph.D in Electrical Engineering, specialization in antennas and propagation, by the University of South Wales, Treforest, United Kingdom, for his research work on the topic: "Novel antenna beamsteering for wireless applications". Currently, he is a full-time researcher at Instituto de Telecomunicações, Portugal - research group of Antennas & Propagation - Leiria (A&P-Lr), working in project RADAVANT (FEDER/PO CENTRO/SI-IDT, 03/SI/2017 - Project n.º 033907). He is also an invited lecturer at Polytechnic Institute of Leiria, Leiria, Portugal. His current research interests include antennas and radio wave propagation, beamsteering antenna systems and RADAR, frequency selective surfaces and metamaterials.

MARIO VALA was born in Leiria, Portugal, in 1996. He received the undergraduate degree in Electrical and Computer Engineering, Electronics & Computers, from the School of Technology and Management (ESTG) of the Polytechnic Institute of Leiria (IPL), Portugal, in 2017. He is a researcher at the Antennas & Propagation (A&P-Lr) research group at Instituto de Telecomunicações, Leiria, Portugal. He is currently working towards the MsC. degree under the theme: "Transmitarray for Antenna Beamsteering at 28 GHz", at the School of Technology and Management (ESTG) of the Polytechnic Institute of Leiria (IPL), Portugal.

RAFAEL F. S. CALDEIRINHA was born in Leiria, Portugal, in 1974. He received the BEng (Hons) degree in Electronic and Communication Engineering from the University of Glamorgan, UK, in 1997. In 2001, he was awarded a Ph.D in Radiowave Propagation by the same University for his research work in vegetation studies at frequencies from 1 to 62.4 GHz. He is currently Head of the Antennas & Propagation (A&P-Lr) research group at Instituto de Telecomunicações, Leiria, Portugal, and Coordinator Professor in Mobile Communications at the School of Technology and Management (ESTG) of the Polytechnic Institute of Leiria (IPLeiria), Portugal. bHis research interests include studies of radiowave propagation through vegetation media, radio channel sounding and modeling and frequency selective surfaces, for applications at microwave and millimeter wave frequencies. Prof. Caldeirinha has authored or co-authored more than 150 papers in conferences and international journals and 4 contributions to ITU-R Study Group, which formed the basis of the ITU-R P.833-5 (2005) recommendation. He is Associate Editor of the IEEE Transactions on Antennas and Propagation journal; Associate Editor of the IET on Microwaves, Antennas and Propagation journal; Member of the editorial board of the International Journal of Communication Systems, IJCS (New York, Wiley); Program chair of WINSYS International Conference between 2006 and 2012; Appointed Officer for Awards and Recognitions of the IEEE Portugal section in 2014; Chair of the IEEE Portugal Joint Chapter on Antennas & Propagation - Electron Devices - Microwave Theory & Techniques since 2016; Regional Delegate of European Association for Antennas and Propagation (EurAAP) for Andorra, Portugal and Spain since March, 2017; and a Senior Member of IEEE and Fellow Member of IET.

ISSN 1751-8644
doi: 0000000000
www.ietdl.org

A Compact Reflector Antenna for Radar Applications at K-band

João R. Reis[1,2*], *Carlos Ribeiro*[2,3], *Rafael F. S. Caldeirinha Author*[1,2]

[1] *Instituto de Telecomunicações, Leiria, Portugal*
[2] *Polytechnic of Leiria, Leiria, Portugal*
[3] *Twevo, Lda., Coimbra, Portugal*
* *E-mail: joao.reis@ipleiria.pt*

Abstract: In this paper, a compact parabolic reflector antenna aiming radar applications in the K-band, is presented. Mainly composed of thermoplastic material and using classical additive techniques (also known as 3D printing), the proposed high-gain antenna exhibits an novel and unique form-factor, particularly of interest for applications with low payload capacity, *e.g.* unmanned aerial vehicles (UAVs). The antenna is composed of 4 parts: *i)* a paraboloid shape embodied in a supporting plastic material; *ii)* a metallic coating applied to the paraboloid surface of *i)*, in order to enable it with electromagnetic (EM) reflecting properties; *iii)* a plastic spacer that ensures the physical separation (*i.e.* focal distance) between parts *i)* and *iv)* and, finally, *iv)* a microstrip patch antenna with reduced ground plane to reduce feed blockage. Subsequently to an overview on the theoretical formulation of parabolic reflector antennas, an antenna targeting 20 dBi and a minimum bandwidth of 500 MHz operating in the 24 GHz ISM radar band, has been dimensioned, optimized in CST Microwave Studio and validated against measurements performed on a physical prototype. The simulation and experimental results are in good agreement, with the prototype yielding 18.3 dBi of gain and 2.2 GHz of useful bandwidth, clearly demonstrating the potential of the proposed antenna design.

1 Introduction

Radio Detection And Ranging (radar) technology [1–3] has been extensively used through the years, since its appearance in early 1940's [4, 5]. Since then, long range radar has been generically used in the military context, for target detection and recognition and air/space surveillance [1, 4]. However, with the continuous evolution of the digital era and chip integration, radar technology became rapidly available for smaller scale applications [6–9]. Nowadays, mid- and short- range radars are widely available in the market, typically operating at micro and millimetre wave frequencies, *e.g.* in the 24 and 77 GHz frequency bands, through commercially-of-the-shelf and system-on-chip (SoC) kits [10–12]. This integration facilitates radar deployment making this technology very attractive for the automotive [13–15] and UAV markets [16–18], in particular for object detection and collision avoidance, and to assist with autonomous safety driving.

From a practical point-of-view, radar systems benefit from having high gain antennas to increase the overall system dynamic range, and consequently the range of the radar [1–3]. Hence, typical antenna designs for radar application comprise either the use of antenna array or parabolic reflector antenna [3]. For example, parabolic reflector antennas are commonly employed in long range radars, where very high gains and large scanning volumes are required. These characteristics however are challenging to mimic with antenna array limited by the feeding network, for which complexity and cost increases with the size of the array, yet providing much limited scanning than the previous solution. Nevertheless, in mid- and short-range radars, antenna array are often preferred due to the ease of integration of microstrip technology with the printed circuit board (PCB) that holds the main radar hardware. This ensures compact and lightweight form factors as it can be seen, for example, in several Frequency-Modulated Continuous Wave (FMCW) radar kits [10–12], where simple linear arrays of microstrip patch antennas are employed.

Some examples of parabolic reflector antenna design at micro and millimetre waves can be found in the literature [5, 19–24]. In particular, the authors in [21] and further in [22] have suggested a compact parabolic reflector design, by using several layers of substrate stacked together, forming a quasi-planar parabolic dish. Even though the concept is proved successful and antenna beamsteering is also demonstrated, by displacing the feeding source from the focal point present in the top stacked layer, the antenna is cumbersome and cost ineffective, due to the excessive number of substrate layers required to form the reflector. Alternatively, in [23, 24], the authors have successfully used 3D printing techniques to produce parabolic reflector antennas and, gains up to 27.8 dBi at 30 GHz, have been reported [24]. In fact, 3D printing antennas have become, *per se*, an hot topic in antenna design and development [23–27], due vast type of printing materials, strong but light-weight mechanical properties, but mostly, due to the ease of manufacture, *i.e.* fast prototyping, and reduced cost of the materials.

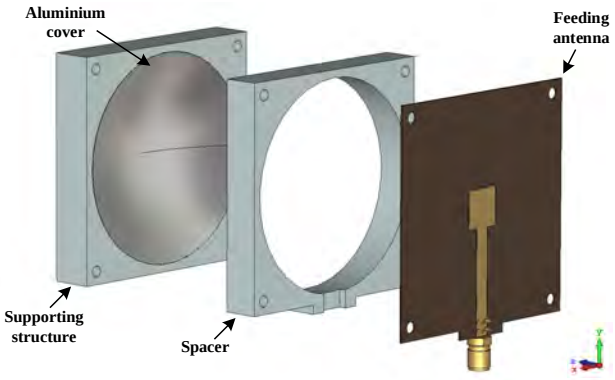

Fig. 1: Block diagram of the proposed antenna configuration.

To this extent, this paper presents a compact parabolic reflector antenna, in a monoblock format, for radar (and radio communication) applications operating in the 24 GHz ISM radar band built upon the work presented by the authors in [28]. The proposed antenna model is depicted in Fig. 1. Designed based on thermoplastic materials, this antenna exhibits a unique form factor with reduced size and light weight, ideal for applications with low payload capacity, *e.g.* in unmanned aerial vehicles (UAVs). Therefore, in this paper, an overview on the main parabolic reflector antenna parameters

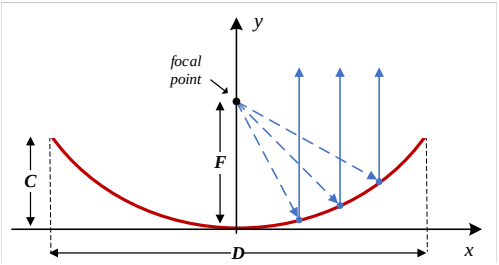

Fig. 2: Generic block diagram of a parabolic reflector antenna.

is performed, to assist with the design of the proposed antenna. Subsequent design, simulation, optimization and validation against experiments on a physical prototype, are also presented.

This paper is organized as follows: Section 2 gives an overview of the main parabolic reflector parameters, including a design guideline to assist with the antenna dimensioning. Section 3 gives details about project specification, including the target operative parameters of the antenna, supporting materials, and the techniques used in antenna manufacture. The setup used for the experimental characterization is also described in this section. In section 4, the monoblock antenna is simulated, optimized, constructed and experimentally validated. Simulation and experimental results are presented side-by-side and followed by a critical discussion. Finally, the main conclusions are drawn in Section 5.

2 Overview of parabolic reflector antenna

Despite being well documented in many textbooks [1–3], this section covers the main attributes of parabolic reflector antennas leading towards the elaboration of a design guideline and to further assist in the elaboration of a table comparing the theoretical, simulated and experimental results, presented in section 4 .

2.1 Main design parameters

The underlying principle of a parabolic reflector is depicted in Fig. 2. A feed source distanced at a focal distance F, illuminates a parabolic reflector with diameter D and depth C, which in turn redirects (reflects) the incident spherical wave (near-field interaction) to yield far-field distance immediately off the reflector, thus, improving the antenna effective aperture and consequently its gain. In fact, these are the main parameters necessary to define the shape of a parabolic reflector.

Following [29], the gain (in dB) of parabolic reflector antenna, in closed form, is expressed by (1),

$$G = 10\ log_{10}\left[\eta\left(\frac{\pi D}{\lambda}\right)^2\right], \quad where\ \eta = \eta_s\eta_t\eta_r\eta_p\eta_b, \qquad (1)$$

D is the diameter of the reflector, λ the operating wavelength and, η is the aperture efficiency. The aperture efficiency can be defined as the relation of the actual gain to the maximum theoretical gain achievable for the same aperture area [3]. Thus, it is a measure that relates the spillover efficiency – η_s, which represents the total power that is radiated by the feed and intercepted by the reflecting surface; the taper or illumination efficiency – η_t, which is the uniformity of the amplitude distribution of the feed pattern over the entire reflector surface; the radiation efficiency – η_r that takes into the ohmic loss in both feeding antenna and parabolic surface; the phase efficiency – η_p that represents the phase uniformity of the field over the aperture plane; and finally, the feed blockage efficiency – η_b, which is determined by the ration of blocked power to total power on the main reflector [1–3]. Each of the factors introduced above has significant effect on the total efficiency η and thus, in gain. Typical values for aperture efficiency vary between 0.3 and 0.7 [3], for a parabolic reflector configuration as the one represented in Fig. 2. In fact, this can be seen in Fig. 3a, where the gain of a parabolic reflector antenna is plotted against the reflector diameter (considering λ at 24.125GHz), for several aperture efficiencies η. From the figure (Fig. 3a), one can observe that the overall efficiency η has considerable impact in the gain specially for larger reflector diameters. For example, the gain for a $D = 100$ mm at 24 GHz varies from 27 to 23 dBi, when total aperture efficiency decreases from 0.7 to 0.3. However, for small dish sizes, this variation in gain is not as significant (Fig. 3a).

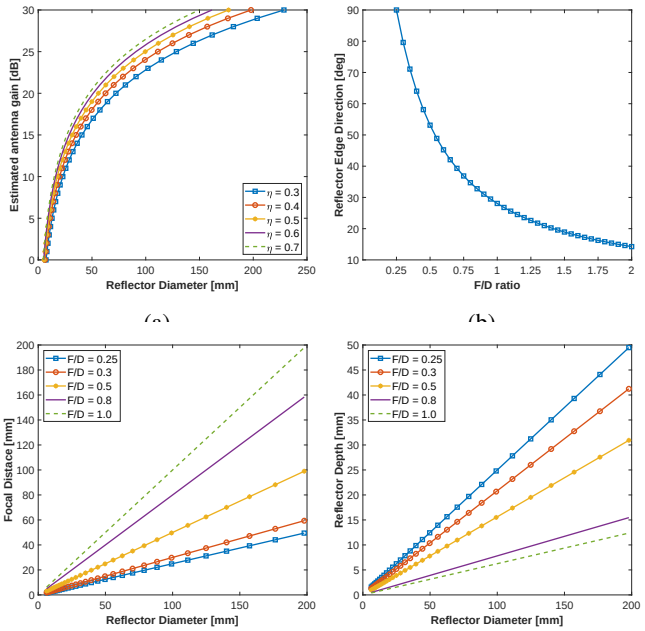

(c) (d)

Fig. 3: Parabolic reflector main parameters: (a) reflector diameter *vs.* total gain and, (b) F/D ratio *vs.* edge direction (θ_{max}), (c) focal distance and (d) reflector depth *vs.* reflector diameter, for several F/D ratio.

According to several textbooks [1, 3], not all the efficiency parameters presented above have the same weight, in global aperture efficiency η. The ones that contribute the most are spillover (η_s) and taper efficiencies (η_t), which are associated to the radiation pattern of the feeding antenna and how well it is matched to the reflector. Hence, the reflector design problem consist mostly of matching the feed antenna pattern to the reflector shape and a compromise between spillover and taper efficiency must exist. For example, very high spillover efficiency can be achieved by a narrow beam pattern with low minor lobes at the expense of a very low taper efficiency [3]. Nevertheless, the traditional rule of thumb for this trade-off is that best efficiency occurs when the illumination at the edge of the parabolic reflector is 10 dB down relative to the one at the centre [1]. However, the -10 dB rule is just a practical consideration that ultimately will depend on the directivity of the feeding source which may not be respected. For example, a dipole antenna used as feed may not be respect the suggested rule of thumb since it exhibits an omnidirectional pattern in one of its planes. Thus, to best match parabolic reflector to the feeding antenna, equation (2) relates the edge direction θ_{max}, *i.e.* direction of the feeding antenna radiation pattern in which the gain is 10 dB lower than at boresight, with the focal-length-to-diameter (F/D) ratio of the parabolic reflector.

$$\theta_{max} = 2tan^{-1}\left(\frac{1}{4(F/D)}\right) \qquad (2)$$

In fact, when analysing Fig. 3b (which plots eq. (2) for several F/D ratios), as the F/D ratio approaches to infinity, the reflector becomes planar ($\theta_{max} = +\infty$). If the F/D is set to 0.25, the focal point is in the same plane of the reflector rim ($\theta_{max} = 90^{\circ}$) [1, 3]. Furthermore, it is worth mentioning that F/D ratio also defines the physical position of the feed and the reflector depth, as it can been seen from figures 3c and 3d, respectively. While Fig. 3c traces the relation

between reflector diameter and focal distance, for several F/D ratio, in Fig. 3c is plotted the diameter depth against diameter, also for several F/D ratios, using the expression (3):

$$C = \frac{D^2}{16F} = \frac{D}{16(F/D)} \tag{3}$$

Finally, another parameter that can be estimated from the physical properties of the reflector is the HPBW. According to [29], an approximation the HPBW can be obtained using (4):

$$HPBW = 70\frac{\lambda}{D} \tag{4}$$

2.2 Design guideline

According to the considerations specified in the previous section, this paper follows the subsequent guideline, which will assist with the antenna designs being presented in section 4:

1. Obtain the reflector diameter using (1) and/ or Fig. 3a, for a desired gain. Since the efficiency is not known at this point, an initial efficiency of $\eta = 0.5$ can be considered;
2. Analyse the radiation pattern of the feeding antenna. Obtain the direction in degrees, in which its gain is 10 dB lower than at boresight. Use the angle to find the F/D ratio through (2) and/ or Fig. 3b;
3. Calculate the focal distance F through the F/D ratio (depicted in Fig. 3c) and the reflector depth C, using (3) and/ or Fig. 3d;

3 Monoblock antenna design considerations

3.1 Proposed antenna configuration

The antenna proposed in this paper has been designed to meet the following specifications requirements: i) frequency of operation at 24.125 GHz, corresponding to the central frequency of the 24 GHz ISM radar band; ii) a bandwidth of (at least) 500 MHz, to cover the entire announced frequency band and, iii) a total gain of 20 dBi, while keeping the side-lobe level below -12 dB. In order to keep the design compact, lightweight and low-cost, the monoblock configuration of Fig. 1 has been considered. The monoblock antenna is then composed of 4 parts: i) a paraboloid shape engraved in plastic material, easily produced using 3D printing techniques; ii) a metallic coating layer applied to i) in order to enable it with EM reflecting properties; iii) a spacer that ensures the distance between part i) and iv) (i.e. focal distance) and, finally, iv) an enhanced microstrip patch antenna with reduced ground planned used as feeding source. Details about design, simulation, optimization and experimental characterization are included in section 4.

3.2 Supporting structure material

In order to keep the design compact and lightweight, the supporting parts of the structure are constructed using additive manufacturing techniques (3D printing). In particular, Polylactic Acid material (PLA) has been used in the main body construction. PLA is a thermoplastic polymer derived from renewable raw materials such as corn starch and sugarcane, which are fermented to lactic acid [30] offering however comparable properties, *e.g.* stiffness, to other plastics in the industry.

Although widely available in the market, the dielectric properties of the PLA material supplied by the manufacturers are often characterized at very low frequencies (around 1 MHz) and thus, not in line with the frequency range of this work. To this end, a literature survey was performed with the aim of find the dielectric properties of the PLA material at micro/millimetre wave frequencies. According to the survey, summarized in Table 1, an ϵ_r = 2.75 and a tan(δ) = 0.02 was found to be a common value among the scientific community, for the electrical properties of this material, at microwave frequencies. This study was intentionally performed *a priori* so that realistic values of the PLA material could be taken into consideration in the electromagnetic simulations and counted the global antenna performance.

At the time of prototyping, PLA from BQ (grey colour) [31] has been extruded with a 0.4 mm nozzle at 220° (hot-end temperature), using a Creality Ender 3 printer, to produce the plastic parts of the antenna. All the parts were prototyped considering 0.2 mm of layer height and 50% infill.

3.3 Parabolic surface metallisation

To enable the imprinted paraboloid shape with electromagnetic reflecting properties, its surface was metallised with aluminium alloy. In the simulation environment, this is set by considering an extra paraboloid solid with finite thickness to represent for the metallic layer. The thickness of the solid was considered to be 20 μm, exceeding therefore the skin depth of $\delta_s = 0.55\ \mu m$ for the aluminium (for a conductivity $\sigma = 3.56 \times 10^7$ S/m). The skin depth was calculated using the generic formula that can be found e.g. in [3]. In the prototyping stage, the metallisation was done stamping two layers of aluminium foil with approximate thickness of 20 μm, to ensure good shielding, trimmed and moulded to the shape of the parabolic surface.

3.4 Experimental setup

In order to test and characterize the proposed antenna model, a prototype of the monoblock antenna has been built and evaluated inside an anechoic chamber. In particular, the antenna matching ($S_{1,1}$) and radiation patterns in the two main antenna planes, have been measured. While the $S_{1,1}$ was obtained on the bench, using a PNA-X Network Analyser (Agilent N5242A), from 22 to 26 GHz, the antenna radiation patterns were measured using the setup of Fig. 4a.

At the transmitter side, a well characterized horn antenna (Flann microwave DP241) was connected to a signal generator (R&S SMR27), producing a continuous wave (CW) signal with 10 dBm, ranging from 23.5 to 25.5GHz, with 12.5MHz steps. At the receiver end, a well characterized standard gain horn antenna (Flann microwave 20240-20) was used as reference (and latter replaced by the antenna under test (AUT)). The receiver antenna was connected to a Spectrum Analyser (Agilent E4407B) to measure the received power. Both antennas were located 1.2 m apart to ensure that the measurements are performed in the far-field region.

In order to obtain the radiation pattern in the two principal antenna planes, the transmitter antenna was kept fixed throughout the measurements, while the receiver one was made to rotate around its own axis, with the assist of motorized pan/tilt head unit. At each angular step within the range of $-180° \leq Az \leq 180°$ and $-25° \leq El \leq 25°$ (limited due to mechanical constrains), the received power was acquired and referenced to the absolute gain of the receiver standard gain horn antenna, following the gain transfer method procedure described in [37]. Prior to a measurement, antennas were aligned to the maximum power direction.

The synchronization between signal generator and spectrum analyser, data acquisition and movement control, was executed in Matlab

Table 1 Dielectric properties of PLA material

ϵ_r	tan(δ)	Freq. Range*	Reference
2,75	0,05	0 - 20 GHz	[32]
≈ 2,75	n.a.	1kHz - 3GHz	[33]
2,72	n.a.	12 - 18 GHz	[25]
2,71	0,017	1 - 10 GHz	[34]
2,57-2,72	0,01	30 - 50 GHz	[35]
2,68	0,0235	4.38 GHz	[36]
2,54	0,019	40 GHz	[30]
2.75	**0.02**	**22 - 26 GHz**	considered in this work

* - Frequency range considered in the work.

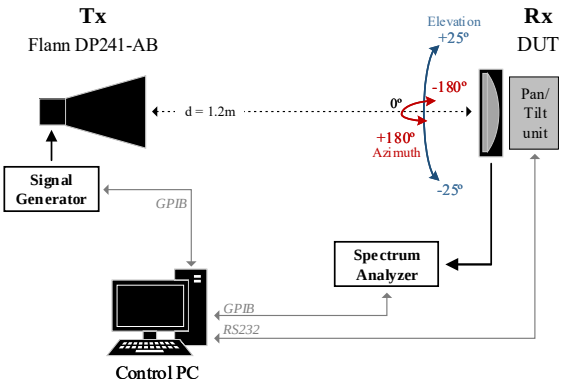

(a)

(b)

Fig. 4: Experimental setup: (a) Side-view representation and (b) photography of the setup inside the anechoic chamber.

using an in-house software routine. To avoid any external electromagnetic contamination and to obtain precise and clean measurement results, all the measurements were obtained inside an anechoic chamber (Fig.4b).

4 Simulation, prototyping and characterization

4.1 Feeding antenna

To implement the feeding element of the monoblock antenna, a microstrip patch was considered. This particular feed design was selected due to its planar form factor, simple manufacturer process and low production cost, which is in line with the concept of the proposed antenna. Moreover, since its radiating properties can be manipulated by slightly changing/ optimizing the design, *e.g.* radiation pattern shape, it can be easily adapted to the reflector shape.

Accordingly, the layout of Fig. 5 has been etched on a double sided Rogers RT5880 substrate, with $\epsilon_r = 2.2$, $tan\delta = 0.0009$ and dimensions of $60 \times 60 \times 0.508$ mm^3. The feed follows the design recommendations of [3] for a microstrip patch antenna, but optimized for a minimal ground plane, in order to reduce feed blockage of the final configuration. In the top plane (Fig. 5a), a 50Ω feed line with length F_l and width F_w, insets the top patch defined by $T_w \times T_l$ by I_l, connecting it to a SMA connector placed at the bottom edge of the substrate. In turn, a microstrip to coplanar waveguide (CPW) transition has been employed to match the feeding line to the SMA connector. In the bottom part (Fig. 5b), a trimmed ground plane defined by a $B_w \times B_l$ patch and a G_l and G_w line, has been considered. The bottom patch is vertically offset in relation to the top one that is centred with the substrate. This offset allows to compensate for the impact of the feed line design in the final radiation pattern shape.

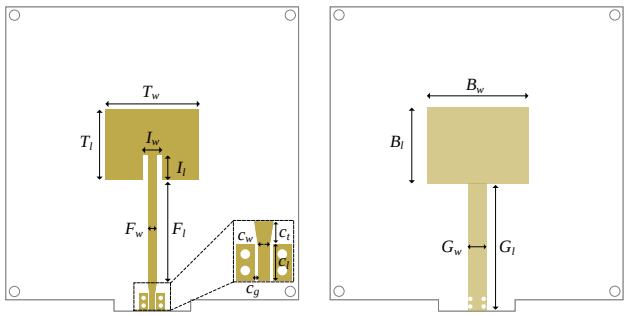

(a) (b)

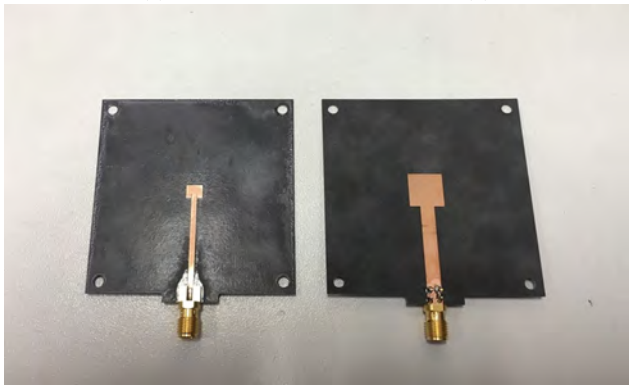

(c)

Fig. 5: Feeding microstrip patch antenna: (a) Top and (b) bottom layer representation (dimensions represented out of scale) and (c) photography of the prototyping.

For the initial set of simulations carried out in CST MWS, the following antenna dimensions were considered: $T_w = 4.92$ mm, $T_l = 3.95$ mm, $I_w = 2.06$ mm, $I_l = 1.35$ mm, $F_w = 1.56$ mm, $F_l = 24$ mm, $c_t = 1.6$ mm, $c_l = 4.7$ mm, $c_w = 1.25$ mm, $c_g = 0.2$ mm, in the top plane and, $B_w = 10$ mm, $B_l = 11$ mm, $G_w = 4$ mm, $G_l = 28$ mm, in the bottom plane and, a vertical offset of 1 mm between patches. The simulation exhibits the S_{11}-parameter depicted in Fig. 6a (blue dash curve). According to the results, the antenna is resonating at 24.125GHz, presenting a relatively good impedance matching for the frequency range defined between 23.7 and 24.55 GHz, *i.e.* $S_{11} < -10$ dB, yielding a bandwidth (BW) of approximately 850 MHz (3.5%).

However, after subsequent S_{11} optimization, this time considering the entire monoblock configuration (Fig. 1), it was found that a value of $T_w = 4.75$ mm, $I_w = 1.94$ mm, $I_w = 1.94$ mm, $F_w = 1.54$ mm and $B_l = 10$ mm, would allow for a better overall S_{11} response, as depicted in Fig. 6b. This design adjustment led to a consequent shift of +225 MHz in the resonant frequency of the feeding antenna (when analysed as individual), as it can be observed in Fig. 6a (orange circled curve). Thus, the final feeding design presents a bandwidth of 960MHz (3.9%) resonating at 24.35 GHz, which compares to the measured bandwidth of 1.37 GHz and the resonance frequency of 24.28 GHz (red filled curve), obtained on the physical prototype of Fig.5c. The minor discrepancy in S_{11}-parameter between simulations and experiments is sought to be associated to the effect of a protective anti-corrosive layer applied to the prototype not considered in simulations.

At the project frequency, *i.e.* 24.125 GHz, the feeding antenna exhibits then a maximum absolute gain of around 7.7 dBi in simulation and 7.5 dBi in experiments realized on the prototype, as it can be seen in the radiation patterns of Fig. 7. In fact, the experimental and simulated radiation patterns cuts in the main antenna planes are in relatively good agreement, although the measurement data in the elevation plane is limited to only $\pm 25^\circ$, due to physical constrains of the existing mechanical rig. Thus, in the elevation plane (Fig. 7b), while the HPBW is of 70° and θ_{max} is set at $\pm 80^\circ$, in simulations,

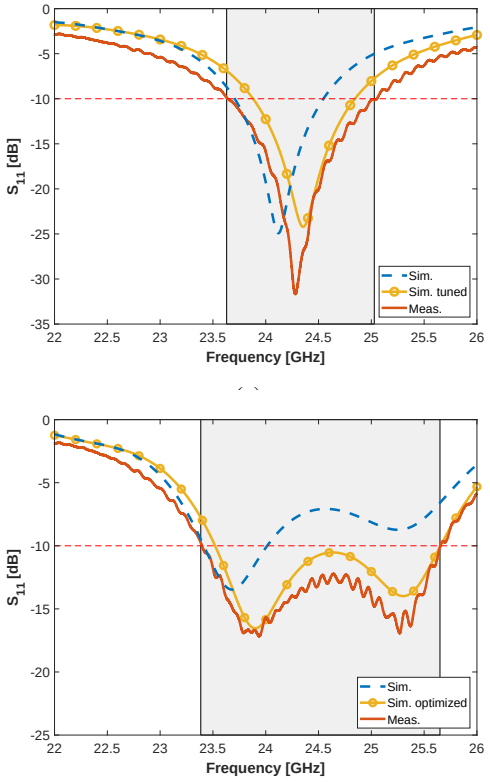

(b)

Fig. 6: Simulated and measured S_{11}-parameters for: (a) feeding antenna and (b) monoblock antenna configuration.

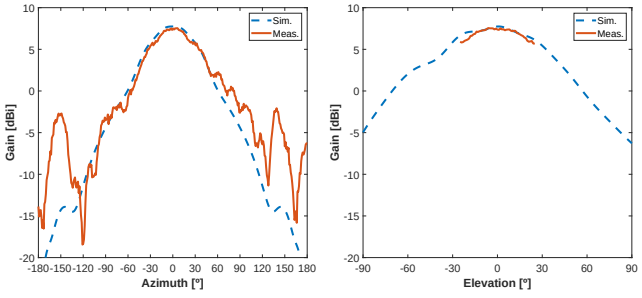

(a) (b)

Fig. 7: Simulated and measured radiation pattern for the feeding antenna, in the two main antenna planes, at 24.125 GHz.

in experiments this information is not available since it falls of the measured angular scanning range.

Nevertheless, in the azimuth plane, the half power beam width (HPBW) is 76° in both simulation and experiments, as depicted in Fig. 7a. Furthermore, the θ_{max} direction is verified at $\pm 75^{\circ}$ in simulation and at $\pm 72^{\circ}$ in experiments. For this plane in particular, the level of the higher side-lobe, *i.e.* the side-lobe level (SLL), is -22 dB verified in simulations against -10 dB obtained with measurement. This difference is sought to be caused by the mechanical rig utilized to support the patch antenna to the pan/tilt unit, not taken into account in the simulation environment.

4.2 Monoblock antenna

In order to build the monoblock antenna suggested in this paper (Fig. 1) and meet the project specifications well defined in section 3.1, a parabolic of revolution with 56 mm of diameter, has been considered. The diameter of the parabola was obtained from eq. (1) with $\eta = 0.5$ (represented in Fig. 3a), in order to achieve

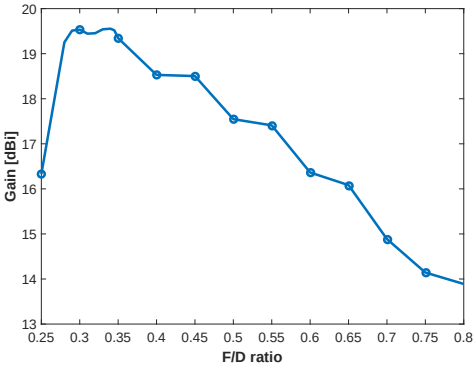

Fig. 8: Simulated F/D ratio variation for parabolic reflector with D = 56mm, at 24.125 GHz.

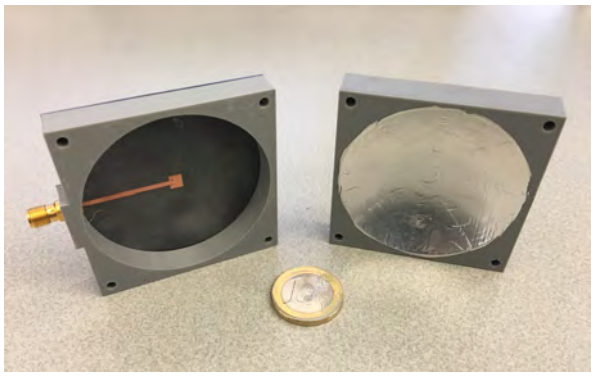

Fig. 9: Prototype of the monoblock antenna.

20 dBi of gain. Therefore, a F/D ratio of 0.35 has been used to best match the parabolic shape to the microstrip feeding antenna, conferring to the design a theoretical focal distance of 19.6 mm. The F/D ratio was estimated through eq. (2) (and Fig. 3b), considering the experimental θ_{max} for the azimuth plane of 72° (obtained in the previous section), and validated in a preliminary simulation (8) using the proposed feeding antenna. From the simulation results it is possible to observe that the maximum gain of the arrangement is obtained for an F/D of 0.35, ensuring the best configuration for design feeding antenna.

A paraboloid shape with 56 mm of diameter and 10mm deep, has been embodied in a $60 \times 60 \times 11$ mm^3 solid of PLA material and, further metallized to enable the reflection of the EM waves. Aluminium material was then applied to the paraboloid surface as described in section 3.3. A hollow PLA spacer with dimensions of 60×60 mm^2 and 9.6 mm of thickness, has been used to ensure the desired physical separation between the reflector and the feeding antenna, *i.e.* focal distance. The spacer was trimmed out internally, with the same diameter of the parabola, to remove the excess material. Four holes have been considered at each corner of the antenna to enable stacking of all antenna parts. Nylon screws have been used to fix all the parts together, but not not considered in simulations. The proposed monoblock antenna, which exhibits an overall dimension of $60 \times 60 \times 21.1$ mm^3, was then simulated in CST MWS and prototyped using addictive manufacture techniques, as detailed in section 3.2. The prototype of the monoblock antenna is depicted in Fig. 9.

The simulated and experimental S_{11}-parameters for the monoblock antenna are depicted in Fig. 6b. After the feeding optimization performed in section 4.1, the antenna presents a relatively good impedance matching, with an $S_{11} < -10$ dB within the frequency band defined from 23.5 to 25.6 GHz (BW = 2.1 GHz – 8.5%) in simulation (orange circled curve), and from 23.4 to 25.6 GHz (BW = 2.2 GHz – 8.9%) obtained in the prototype (red fill curve). This represents a substantial improvement over the antenna bandwidth prior to the feeding optimization.

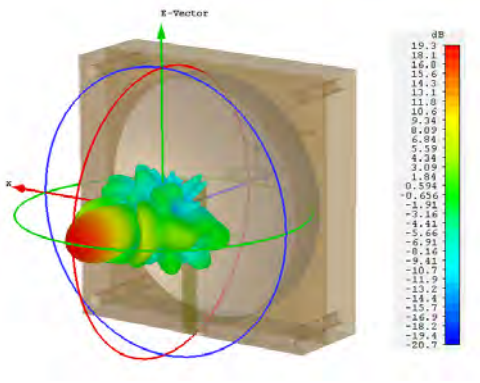

Fig. 10: Simulated 3D radiation pattern of the monoblock antenna.

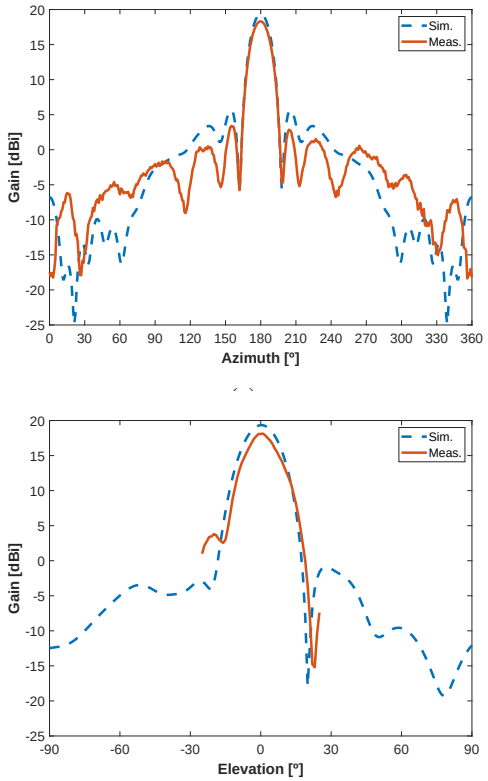

(b)

Fig. 11: Simulated and measured radiation pattern for the monoblock antenna configuration in: (a) azimuth and (b) elevation planes, at 24.125 GHz.

According to the radiation patterns of both Fig. 10 and Fig. 11, a maximum gain of 19.3 dBi and a HPBW of 16°, in both azimuth and elevation planes, is obtained at 24.125GHz. In the prototype, an absolute gain of 18.3 dBi and HPBW of 16° and of 14° in the azimuth and elevation planes, respectively, are measured. Furthermore, the SLL (to the higher side-lobe) is of -13.7 dB in simulation against -14.4 dB obtained with the prototype. The similarity between simulated and experimental results is notorious, validating therefore the proposed antenna model.

Nevertheless, when analysing in detail the radiation pattern in the azimuth plane (Fig. 11a), an unexpected back-lobe with -7 dBi of gain is presented in simulation. Although this back-lobe is attenuated by 26 dB relative to the maximum of the radiation pattern and could be neglected, this may suggest that some energy was still passing through the metallized surface, despite of the fact the thickness of the considered metallic surface exceed by x40 the skin depth of

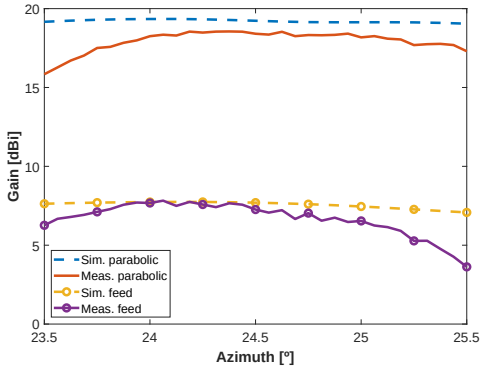

Fig. 12: Comparison of the simulated and experimental gain over the frequency.

Table 2 Main monoblock antenna parameters at the project frequency (24.125 GHz).

Parameter	Target†	Simulated	Measured	Units
Gain	20	19.3	18.3	[dBi]
BW	0.5	2.1	2.2	[GHz]
HPBW in azim.	15.5‡	16	16	[°]
HPBW in elev.	15.5 ‡	16	14	[°]
SLL	-12	-13.7	-14.4	[dB]
App. efficiency (η)	0.5	0.44	0.34	n/a

† - Set by the project specification/ requirements;

‡ - Extracted analytically using eq. (4).

the aluminium, as detailed in section 3.3. This situation is not verified in the measurement results, where the front-to-back ratio is of 35 dB, ensuring that a good metallisation of the parabolic surface was performed.

Over the useful antenna bandwidth (23.5 to 25.5 GHz), that covers the 24 GHz ISM radar band in which the monoblock antenna was designed to operate, the total gain presents a smooth linear response. According to measurements, the gain only decays 2.5 dB relative to the maximum absolute gain of 18.6 dBi found at 24.35 GHz, as observed in Fig.12. This in fact, represents an average gain of around 10 dB when comparing the microstrip patch feeding antenna against the monoblock configuration, clearly demonstrating the potential of the proposed antenna design.

As a summary, the main performance parameters of the monoblock antenna are detailed in Table 2, comparing side-by-side the analytical against simulations and experiments results realized on a physical prototype of the monoblock antenna, at the project frequency (24.125 GHz).

5 Conclusions

This paper presents a compact, high-gain, monoblock antenna, designed to operate in the 24 GHz ISM radar band. The antenna is mostly constructed based on thermoplastic materials produced using addictive manufacturer techniques, configuring a novel approach in antenna design. Firstly, an overview of the main parabolic reflector parameters is performed, yielding to the elaboration of a design guideline to assist with the proposed antenna dimensioning. Subsequently, the main project considerations are specified including the operative parameters of the antenna, supporting material and its characterization, and the techniques used in antenna manufacture. The setup used for the experimental characterization is also described. Finally, the proposed antenna is designed, optimized, constructed and experimentally validated, starting with the feeding antenna, *i.e.* a microstrip patch with reduced ground plane, and concluding with the overall monoblock antenna configuration. Simulation and experimental results, which are in good agreement, are presented side-by-side and critically discussed. The proposed antenna model,

with an overall dimension of $60 \times 60 \times 21$ mm^3, presents according to experiments, 18.3 dBi of gain at 24.125 GHz, a total bandwidth of 2.2 GHz, a HPBW of 16° and 14°, in the azimuth and elevation planes, respectively, and a maximum SLL level of -14 dB. Further work will aim at the study of novel techniques and materials for prototyping improvement, *e.g.* surface metallisation, whilst keeping the unique, compact, and innovative shape that can be easily adaptable to any radar and radio communications system, and employed in systems with limited payload capability.

6 Acknowledgements

This work is partially supported by the European Regional Development Fund (FEDER), PO CENTRO/SI-IDT, Project RADAVANT (03/SI/2017 - Project n.º 033907) and by the Portuguese Government, Foundation for Science and Technology, FCT, through the financial support provided under UIDB/EEA/50008/2020.

7 References

1 Skolnik, M.I.: 'Radar Handbook'. Third edition ed. Electronics electrical engineering. (McGraw-Hill Education, 2008). Available from: https://books.google.pt/books?id=76uF2Xebm-gC
2 Mervin.C..Budge, S.R.G.: 'Basic Radar Analysis'. Artech House Radar. (Artech House Publishers, 2015)
3 Balanis, C.A.: 'Antenna Theory: Analysis and Design, 4th Edition'. (John Wiley & Sons, 2016)
4 Guarnieri, M.: 'The early history of radar [historical]', *IEEE Industrial Electronics Magazine*, 2010, **4**, (3), pp. 36–42
5 Cutler, C.C.: 'Parabolic-antenna design for microwaves', *Proceedings of the IRE*, 1947, **35**, (11), pp. 1284–1294
6 Li, C., Peng, Z., Huang, T., Fan, T., Wang, F., Horng, T., et al.: 'A review on recent progress of portable short-range noncontact microwave radar systems', *IEEE Transactions on Microwave Theory and Techniques*, 2017, **65**, (5), pp. 1692–1706
7 Öztürk, E., Genschow, D., Yodprasit, U., Yilmaz, B., Kissinger, D., Debski, W., et al.: 'A 60-ghz sige bicmos monostatic transceiver for fmcw radar applications', *IEEE Transactions on Microwave Theory and Techniques*, 2017, **65**, (12), pp. 5309–5323
8 Pyo, G., Kim, C., Hong, S.: 'Single-antenna fmcw radar cmos transceiver ic', *IEEE Transactions on Microwave Theory and Techniques*, 2017, **65**, (3), pp. 945–954
9 Peng, Z., Muñoz-Ferreras, J.M., Tang, Y., Liu, C., Gómez-García, R., Ran, L., et al.: 'A portable fmcw interferometry radar with programmable low-if architecture for localization, isar imaging, and vital sign tracking', *IEEE Transactions on Microwave Theory and Techniques*, 2017, **65**, (4), pp. 1334–1344
10 Infineon. 'DEMO DISTANCE2GO - Infineon radar demo board'. (, . Available from: https://www.infineon.com/cms/en/product/evaluation-boards/demo-distance2go/
11 Infineon. 'DEMO SENSE2GOL - Infineon radar demo board'. (, . Available from: https://www.infineon.com/cms/en/product/evaluation-boards/demo-sense2gol/
12 Instruments, T.. 'AWR1642 single-chip 76-GHz to 81-GHz automotive radar sensor'. (, . Available from: https://www.infineon.com/cms/en/product/evaluation-boards/demo-sense2gol/
13 'Automotive radar: Status and trends', 2005
14 Menzel, W., Moebius, A.: 'Antenna Concepts for Millimeter-Wave Automotive Radar Sensors', *Proceedings of the IEEE*, 2012, **100**, (7), pp. 2372–2379
15 Chipengo, U.: 'Full physics simulation study of guardrail radar-returns for 77 ghz automotive radar systems', *IEEE Access*, 2018, **6**, pp. 70053–70060
16 Patel, J.S., Fioranelli, F., Anderson, D.: 'Review of radar classification and RCS characterisation techniques for small UAVs or drones', *IET Radar, Sonar Navigation*, 2018, **12**, (9), pp. 911–919
17 García Fernández, M., Álvarez López, Y., Arboleya Arboleya, A., González Valdés, B., Rodríguez Vaqueiro, Y., Las-Heras Andrés, F., et al.: 'Synthetic aperture radar imaging system for landmine detection using a ground penetrating radar on board a unmanned aerial vehicle', *IEEE Access*, 2018, **6**, pp. 45100–45112
18 Lort, M., Aguasca, A., López-Martínez, C., Marín, T.M.: 'Initial evaluation of sar capabilities in uav multicopter platforms', *IEEE Journal of Selected Topics in Applied Earth Observations and Remote Sensing*, 2018, **11**, (1), pp. 127–140
19 Mehrabani, A., Shafai, L.: 'Compact dual circularly polarized primary feeds for symmetric parabolic reflector antennas', *IEEE Antennas and Wireless Propagation Letters*, 2016, **15**, pp. 922–925
20 Manohar, V., Kovitz, J.M., Rahmat-Samii, Y.: 'Synthesis and analysis of low profile, metal-only stepped parabolic reflector antenna', *IEEE Transactions on Antennas and Propagation*, 2018, **66**, (6), pp. 2788–2798
21 Hosseini, A., De Flaviis, F. '60 ghz wideband printed quasi-parabolic reflector antenna'. In: 2014 IEEE Antennas and Propagation Society International Symposium (APSURSI). (, 2014. pp. 1475–1476
22 Hosseini, A., Kabiri, S., De Flaviis, F.: 'V -Band High-Gain Printed Quasi-Parabolic Reflector Antenna With Beam-Steering', *IEEE Transactions on Antennas and Propagation*, 2017, **65**, (4), pp. 1589–1598
23 Menéndez, L.G., Kim, O.S., Persson, F., Nielsen, M., Breinbjerg, O. '3d printed 20/30-ghz dual-band offset stepped-reflector antenna'. In: 2015 9th European Conference on Antennas and Propagation (EuCAP). (, 2015. pp. 1–2
24 Zhai, Y., Xu, D., Zhang, Y.: 'Ka-Band Lightweight High-Efficiency Wideband 3D Printed Reflector Antenna', *International Journal of Antennas and Propagation*, 2017,
25 Zhang, S., Arya, R.K., Pandey, S., Vardaxoglou, Y., Whittow, W., Mittra, R.: '3d-printed planar graded index lenses', *IET Microwaves, Antennas Propagation*, 2016, **10**, (13), pp. 1411–1419
26 Pourahmadazar, J., Sahebghalam, S., Abazari Aghdam, S., Nouri, M. 'A millimeter-wave fresnel zone plate lens design using perforated 3d printing material'. In: 2018 IEEE MTT-S International Microwave Workshop Series on Advanced Materials and Processes for RF and THz Applications (IMWS-AMP). (, 2018. pp. 1–3
27 Pizarro, F., Salazar, R., Rajo-Iglesias, E., Rodríguez, M., Fingerhuth, S., Hermosilla, G.: 'Parametric study of 3d additive printing parameters using conductive filaments on microwave topologies', *IEEE Access*, 2019, **7**, pp. 106814–106823
28 João.R..Reis, C.R., Caldeirinha, R.F.S. 'Novel parabolic dish antenna for RADAR applications'. In: The IET's Antennas and Propagation Conference - APC 2019, Birmingham, UK. (, 2019.
29 Orfanidis, S.J.: 'Electromagnetic Waves and Antennas'. Orfanidis, S.J., editor. (Rutgers University, 1999-2016). Available from: http://ece web1.rutgers.edu/~orfanidi/ewa/
30 Boussatour, G., Cresson, P.., Genestie, B., Joly, N., Lasri, T.: 'Dielectric characterization of polylactic acid substrate in the frequency band 0.5–67 ghz', *IEEE Microwave and Wireless Components Letters*, 2018, **28**, (5), pp. 374–376
31 BQ. 'PLA filament 1,75mm datasheet'. (, . Available from: https://www.bq.com/pt/support/pla-premium/support-sheet
32 Felício, J.M., Fernandes, C.A., Costa, J.R. 'Complex permittivity and anisotropy measurement of 3D-printed PLA at microwaves and millimeter-waves'. In: 2016 22nd International Conference on Applied Electromagnetics and Communications (ICECOM). (, 2016. pp. 1–6
33 C..Dichtl, P.S., Krohns, S.: 'Dielectric Properties of 3D Printed Polylactic Acid', *Advances in Materials Science and Engineering*, 2017, **2017**, pp. 10
34 Zechmeister, J., Lacik, J. 'Complex relative permittivity measurement of selected 3d-printed materials up to 10 ghz'. In: 2019 Conference on Microwave Techniques (COMITE). (, 2019. pp. 1–4
35 Reyes, N., Casado, F., Tapia, V., Jarufe, C., Finger, R., Bronfman, L.: 'Complex Dielectric Permittivity of Engineering and 3D-Printing Polymers at Q-Band', *Journal of Infrared, Millimeter, and Terahertz Waves*, 2018, **39**, (11), pp. 1140–1147. Available from: https://doi.org/10.1007/s10762-018-0528-9
36 Catarinucci, L., Colella, R., Coppola, P., Tarricone, L.: 'Microwave characterisation of polylactic acid for 3d-printed dielectrically controlled substrates', *IET Microwaves, Antennas Propagation*, 2017, **11**, (14), pp. 1970–1976
37 IEEE: 'IEEE Standard Test Procedures for Antennas', *ANSI/IEEE Std 149-1979*, 1979, p. 01

Annex II - Scientific Conferences Publications

Disruptive Future of Radar Based on All-Digital PN Signal Processing

Rafael F. S. Caldeirinha[1,2], João R. Reis[1,2], André Sardo[1,2], Luis Duarte[1,2], Nuno Leonor[1,2], João Gil[3] and Carlos Ribeiro[1,3]
[1]Polytechnic Institute of Leiria, Leiria, Portugal
[2]Instituto de Telecomunicações - Leiria, Portugal
[3]TWEVO *Lda.*, Coimbra, Portugal

***Abstract*—This paper presents the first results on the design and implementation of a real-time and high resolution monostatic radar at 24 GHz, based on the sliding correlation of pseudo-noise (PN) sequences. The real-time radar, with a high time resolution better than 4ns, is used for moving target identification (MTI) in the presence of highly dense clutter, under harsh environments and severe weather conditions (fog, snow and fire smoke or plume). A radar signal processing based on all-digital PN sequences is proposed, which represents a quantum leap in radar future front-end architecture. Results obtained in a controlled environment, inside an anechoic chamber, are presented and a benchmark with a commercially-of-the-shelf solution is presented.**

***Index Terms*—STDCC, FMCW, Radar, Monostatic, PN sequences, FPGA.**

I. Introduction

Radar sensors have been deployed in the automotive industry and will foresee massive use in autonomous driving and drone based applications. In spatial reconstruction of the environment surrounding the radar becomes an important issue in many applications, including concealed-object detection and identification.

Many radar topologies that have been presented in the literature [1], mostly based on Frequency Modulated Continuous Wave (FMCW), except for some military applications, have limited performance in heavy cluttered environments. In [1], [2], Orthogonal Frequency Division Multiplexing (OFDM) is being proposed to overcome the limitations of FMCW radars, particularly by resolving several different (moving) targets in a highly dense clutter environment and interference from other radars. Quasi real-time processing demands for high computational resources typically in field-programmable gate array (FPGA) based architectures, with physical bandwidths in the order of a few GHz. These may be cumbersome if multiple radar front-ends are to be used, being limited by the analogue-to-digital converters (ADC), which typically have bandwidths below 1 GHz and prohibitive costs for mass production.

Radar signal processing based on all-digital pseudo-noise (PN) sequences represents a quantum leap in radar future front-end architecture, presenting significant advantages in terms of low baseband computational demands, yielding a plethora of opportunities for massive deployment in autonomous driving applications.

In particular, this paper presents the first trails on a Swept Time-Delay Cross-Correlator (STDCC) PN Radar at 24 GHz. The proposed radar architecture follows the STDCC principle well covered in [3]–[5] and it is sought to mitigate incumbent and mutual interference risks and interference mechanisms, given its excellent auto-correlation properties. Besides presenting radar measurement results for several case studies, obtained inside an anechoic chamber, this paper compares the performance of the proposed radar system with a FMCW commercially-of-the-shelf solution.

This paper is organised as follows: section II details the topology of the proposed radar architecture, giving particular emphasis to the radio frequency (RF) and intermediate frequency (IF) stage, including the hardware description of the main parts. Section III describes the baseband signal generation, with particular attention to the generation of the PN sequences within a FPGA environment. In section IV, the practical implementation and performance analysis of the STDCC radar are performed, considering several measurement scenarios. The performance evaluation of the proposed radar with a FMCW commercial solution is also included. Finally, the main conclusions are drawn in section V.

II. Radar Topology

This section thoroughly details the proposed system giving the necessary technical insight about the radar architecture. For instance, Fig. 1 depicts the block diagram of the radar topology. The block diagram is divided in two sub-systems, corresponding to different stages of the system's architecture, namely the RF and IF stages.

In the RF stage, a high precision Voltage Controlled Oscillator (VCO) is used to lock the phase-lock-loop (PLL) configured to output a 12.0 GHz RF signal. After appropriate signal conditioning (filtering and amplification) to suppress undesired spurious signals and adjust the power level, a frequency multiplier is employed to achieve the necessary $f_{LO} = 24$ GHz reference signal. This, in turn, is used to source both the single side band (SSB) up-converter and the IQ down-converter mixers using a 2-way power divider. Thus, the Tx mixer up-converts the base-band signal (f_{IF}) generated by an FPGA (Tx PN Sequence) in the IF stage block into a 24 GHz RF signal. Subsequently, an amplification stage is considered to increase the output power level up to the

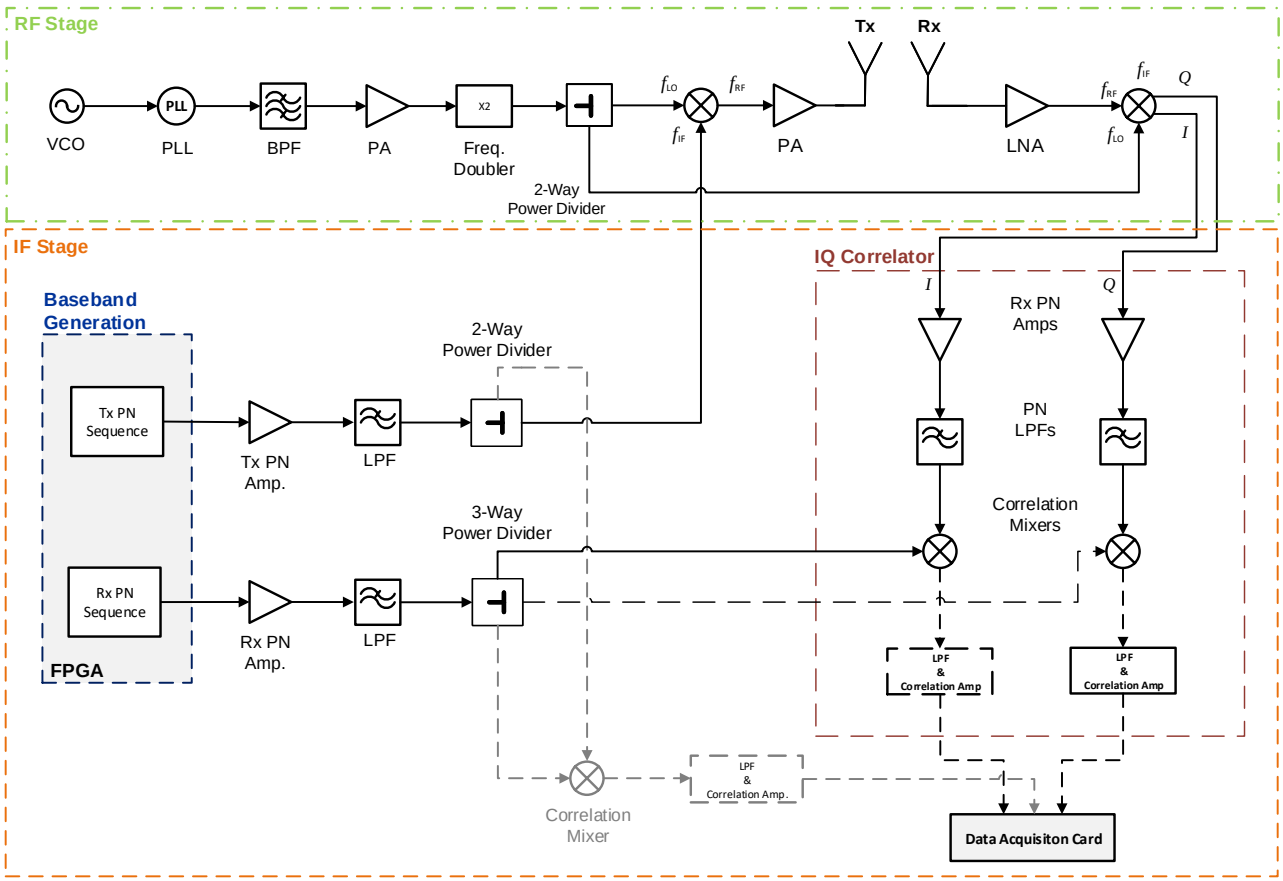

Fig. 1: Block diagram of the STDCC radar architecture.

limits of interest for the radar. On the other hand, the Rx mixer de-modulates the RF signal from the radio channel that contains radar information, into a differential signal with In-phase (I) and In-quadrature (Q) components that inputs the IQ Correlator in the IF block.

The RF stage (Fig. 1) is implemented using *X-Microwave* technology, which is a complete modular building block eco-system for microwave components that allow easy integration of RF components, aiming at fast prototyping. Two identical 20 dBi standard gain horn antennas (*Flann* 22240-20) are used side-by-side, as transmitter and receiver, distanced 1 cm apart.

In the IF Stage, a 511 bits length pseudo-noise sequence of Maximum Length Linear Shift Register (MLSR) type is generated by an FPGA at two different rates. The sequence to be transmitted over-the-air (Tx PN sequence) has a sampling rate of $f_{seqTx} = 250.1$ MHz whereas the one to be correlated in the receiver (Rx PN sequence) is decreased by 100 kHz, resulting in a sliding factor of $k = 2500$ according to (1) [3], [4]. Specifics about the baseband PN sequence generation are detailed in Section III.

$$k = \frac{f_{seqTx}}{\text{slip rate}} = \frac{f_{seqTx}}{f_{seqTx} - f_{seqRx}} = 2500 \qquad (1)$$

The differential signal that is fed into the IQ Correlator block and contains the radar information is amplified and filtered before being correlated with the Rx PN Sequence generated by the FPGA. The I and Q signals are analysed in both independent branches allowing for *Doppler* detection.

After correlation, the resulting signal is amplified and filtered, in order to be properly detected by a data acquisition (DAQ) card. To this extent, specific electronic circuitry was developed, comprising two printed-circuit boards for the amplifier and filter components, respectively. A 12-pole switch was included so that pre-defined gains can be adjusted according the specific dynamic range envisaged for a specific geometry/measurement. The gain of the post-correlation IQ signals can vary from 14 up to 19 dB, providing an appropriate level for the DAQ card input ports. As per the low-pass filter, a 7^{th} order *Chebyshev* filter, with maximum theoretical ripple of 0.01 dB, and a cut-off frequency of 200 kHz (twice the slip-rate), was implemented. This type of filter was chosen due to its steep roll-off, while minimising the pass-band ripple.

The acquisition of the correlation signals is done using a ordinary DAQ, i.e. *Picoscope* 3406-D MSO, with 4 analogue inputs of 250 MHz bandwidth, and a maximum sampling frequency of 1 GS/s and 8 bits of resolution.

In order to obtain a clear temporal reference, an optional auto-correlation stage could be included (as marked in grey

colour in Fig. 1), at the expense of using one extra correlation mixer, amplifier and filter. This is currently used in the system to reference the temporal instants and to trigger the data acquisition card for signal measurement.

III. All-Digital Baseband

The baseband block, marked with blue-dashed line in Fig. 1, is the radar sub-system responsible for generating the receiver and transmitter PN sequences. This implementation adopts 511 points maximum length real-valued bipolar PN binary sequences. The real-valued bipolar PN binary sequences open way to the use of the FPGA's unipolar digital output pins, followed by a DC removing block, to generate the analogue baseband signal, thus eliminating the need to use expensive high-speed Digital-to-Analogue (DAC) converters. The block diagram of this sub-system is depicted with more detail in Fig. 2. The baseband is composed of 3 main blocks: Clock generation, Transmitter Sequence Generation and Receiver Sequence Generation. Its outputs feed both IF stage PN amplifiers identified in Fig. 1.

The clock generation block outputs 2 digital clock signals with frequencies of 250.1 MHz and 250 MHz that feed, respectively, the transmitter sequence generation and receiver sequence generation blocks. The different frequencies fed to the transmitter and receiver sequence generation blocks are responsible for the previously identified sliding factor, crucial for the operation of the STDCC [3]–[5] algorithm. To generate two clock signals at close but different frequencies, from a single reference clock signal with a frequency of 125 MHz, two reconfigurable PLL blocks (RX Clk Generator and TX Clk Generator in Fig. 2) must be used inside the FPGA. Because this circuit was implemented in a Xilinx Kintex-7 FPGA KC705 Evaluation Kit [6], the PLL blocks are implemented with 2 Xilinx's mixed-mode clock managers (MMCM) [7]. The receiver MMCM receives the 125 MHz clock signal and is configured to output 2 clock signals with different frequencies: the 250 MHz clock signal that will drive the receiver sequence generation block, and a 13.864818 MHz clock signal that will drive the transmitter MMCM. The transmitter MMCM is configured to output the 250.1 MHz clock signal that will drive the transmitter sequence generation block.

The transmitter and receiver sequence generation blocks are identical. The only difference is the frequency of the clock signal that drives them. Each sequence generation block is composed of a binary counter and a ROM. The 9-bit binary counter counts from 0 to 510, sequentially addressing the 512-words, single bit-depth ROM. The ROM holds the unipolar version of PN binary sequence adopted in the implementation. The outputs of both ROMs are routed to 2 digital output pins, configured with the highest slew rate and drive strength.

IV. Practical Implementation and Performance Analysis

A. Experimental Setup

In order to assess the performance of the proposed radar, the setup of Fig. 3 was assembled inside the anechoic chamber

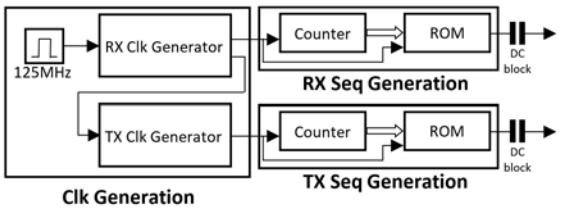

Fig. 2: STDCC radar baseband.

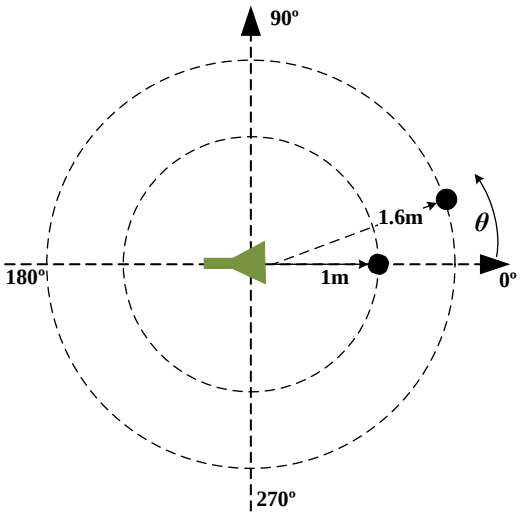

Fig. 3: Radar benchmark setup.

to reduce the multipath effects and avoid possible external RF interferences. The radar prototype was placed, according to Fig. 4a, at the centre of the 6 m by 5 m chamber, on top of a motorised turntable, that enables $360°$ rotation in the azimuth plane (represented herein by θ) with $0.5°$ resolution. Several case studies have been considered by placing metallic poles with 6 cm of diameter and 2 meters height, at the vicinity of the radar. The poles were distributed inside the anechoic chamber according to geometry depicted in Fig. 3. Radar measurements for distance and angular dependences, using both STDCC and FMCW radars, have been performed in the following order:

1) A single metallic pole, placed 1 m apart of the proposed radar aperture, at boresight direction ($\theta = 0°$);
2) Two metallic poles, one placed at 1 m at boresight direction and the other at 1.6m steered off $10°$ from the boresight direction ($\theta = 10°$).

For both geometries, the radar system under test was made to rotate $360°$ with a $0.5°$ steps increment. It is also important to mention that for every step taken, 20 radar acquisitions have been measured and then averaged (Power Delay Profile) to obtain a plan position indicator (PPI) and assess the target identification performance. As stated, the STDCC radar target identification performance was assessed with one and two metallic poles and later compared with an off-the-shelf FMCW

commercial solution (Distance2Go, from Infineon).

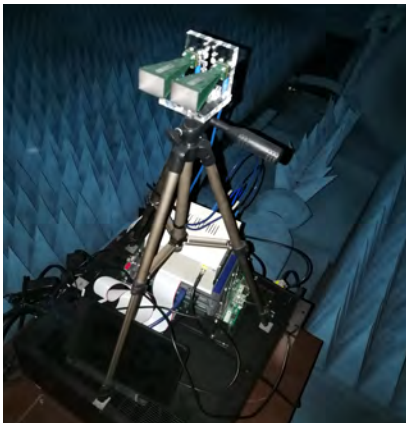

(a)

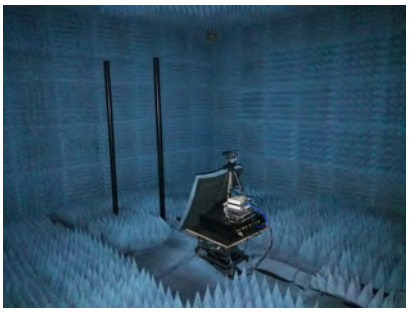

(b)

Fig. 4: (a) Photography of the STDCC radar prototype, (b) Two-pole experimental setup assembled inside the anechoic chamber.

In the first scenario, the proposed radar was placed in the middle of an anechoic chamber on top of the turntable with one pole 1m apart and at bore-sight (0°). As explained in the previous section, both I and Q signals were considered for correlation and their results have been squared and summed together which, when plotted, yield the PDP result per angle. To better illustrate the radar performance, such values are plotted in two graph types: waterfall and polar plots, as depicted in Figs. 5a and 5b, respectively. While the waterfall graph presents the measured averaged PDP, for every angular step in the azimuth plane, displaying the radar distance in the y-axis and the azimuth angle in the x-axis, the polar plot shows the detected peaks, at each scanned angle, after running a simple peak-detection algorithm.

B. Experimental Results

To evaluate the performance of both STDCC and FMCW radars, several measurements have been considered. The respective results are presented and discussed in this section side-by-side for a more convenient analysis. From Fig. 5a, it can be concluded that the STDCC radar is accurately detecting a peak at 1 m distance at 0°, corresponding to the correct pole location inside the anechoic chamber. In fact, this can be confirmed in the plot of Fig. 5b, that clearly identifies an object at 1m away from the radar at boresight direction to the object. However, it is worth to mention that the gradient variation of colours around the detected object, in Fig. 5a, is associated to the antennae radiation pattern discrimination that exhibits an half-power beam-width of around 23°, in both azimuth and elevation planes, at the considered frequency.

On the other hand, with the commercially available radar, it is also possible to detect the same pole, as depicted in the plan position indicator of Fig. 5c. From the experimental data, an object is detected at 0° and a peak value at 1.1 m. Interestingly, several artefacts, albeit being 5-10 dB below the main contribution, are also observed almost in any direction. Due to this fact, the polar plot of Fig. 5d depicts false positives, since other peaks rather than the main contribution have also been detected by the peak-detection algorithm.

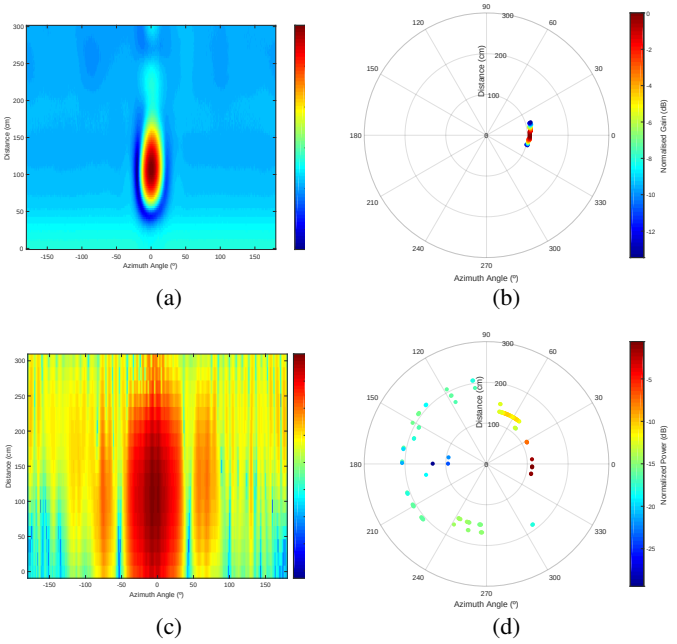

(a) (b)

(c) (d)

Fig. 5: Experimental results for one-pole scenario: (a, c) waterfall PPI plots and (b, d) polar PPI plots for, the STDCC and FMCW radars, respectively.

Furthermore, when conducting the second set of experiments, i.e. maintaining the 1 m distance pole and adding a second pole at 1.6 m deviated 10° in azimuth (according to the diagram of Fig. 3), it is possible to observe that both radars are detecting the artificial targets. From the experimental results of Fig. 6, both STDCC and FMCW radars are still able to detect the metallic pole placed 1 m distance, with the STDCC radar (Fig. 6a) presenting a slight advantage with a greater measurement accuracy, when compared with the FMCW one (Fig. 6c). However, when the second pole is added to the scenario, it can be seen from Fig. 6c that the commercial solution fails to resolve such object. Although a slight increase in power at the region of $\theta = 10°, d = 1.5$ m is noticed, it is not possible to clearly distinguish between the two objects. In fact, it seems the second pole is masked by the effect caused by the pole placed

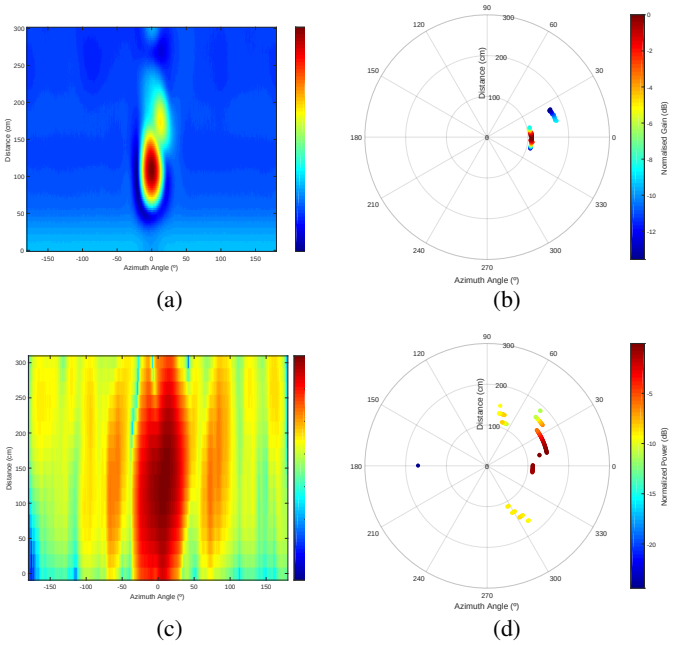

(a) (b) (c) (d)

Fig. 6: Experimental results for two-pole scenario: (a, c) waterfall PPI plots and (b, d) polar PPI plots, for the STDCC and FMCW radars, respectively.

at 1 m apart. Similarly to the first measurement (Fig. 5c), many artefacts are also observed in the 360° scan with amplitudes 5-10 dB below the main reflections.

In this particular case, the STDCC radar really show its merits and stands out from its counterpart, since it is able to clearly detect and distinguish both metallic poles (Figs. 6a and 6b), at the correct locations, *i.e.* first pole at $\theta = 0°, d = 1$m and second pole at $\theta = 10°, d = 1.6m$. In fact, these results have been consistent throughout a series of repeated measurements, and a maximum range discrepancy of only 9 cm have been detected between experimental radar data and effective physical distance. This error is acceptable, as it falls within the spatial precision associated with the bandwidth used in the proposed radar. The signal level difference of about 7-9 dB observed in Fig. 6a is due to the excess path loss corresponding to distance of flight between poles (i.e. 1.2 m), in addition reflection loss introduced by the second pole (i.e around 2 dB).

From the results above, it is possible to state that the proposed system is capable to detect closely space objects in the limit of the radar spatial resolution and thus presenting a remarkable performance over the tested commercial solution.

V. Conclusions

Understanding of existing and emerging radar waveforms based on STDCC and their limit factors on both time/spatial resolutions and range have been consolidated and validated against measurements. A radar signal processing based on all-digital PN sequences has been proposed, representing a quantum leap in radar future front-end architecture. The future radar technology, and hence the disruptive future, should be capable to operate in multi-user operation in several deployment environments using orthogonalisation signals between different radars (users). This is sought to be accomplished by taking advantages of the orthogonality of the proposed technique based on STDCC, as in typical radio channel sounders, in which the implementation and acquisition of baseband signals (PN) is assumed to be all-digital. And thus, to reduce production costs and make it a good candidate for mass-production. Finally, the potential of multi-PN transmission for direction-of-arrival estimation and radar imaging, is well underway.

Acknowledgements

This work is partially funded by Research and Technological Development Incentive Scheme CO-PROMOTION - Centro2020 - P2020 - European Regional Development Funds, under project RADAVANT - Radar for Detection and Avoidance in Unmanned Aerial Vehicles (PI nr. 033907).

References

[1] W.Wiesbeck and L. Sit, "Radar 2020: The future of radar systems," *International Radar Conference*, pp. 1–6, Oct. 2014.

[2] J. S. A. Gameiro, D. Castanheira and P. P. Monteiro, "Research Challenges, Trends and Applications for Future Joint Radar Communications Systems," *Wireless Personal Communications*, vol. 100, no. 1, pp. 81–96, May 2018.

[3] R. J. Pirkl and G. D. Durgin, "Optimal Sliding Correlator Channel Sounder Design," *IEEE Transactions on Wireless Communications*, vol. 7, no. 9, pp. 3488–3497, Sep. 2008.

[4] D. Ferreira, R. F. S. Caldeirinha, and N. Leonor, "Real-time High-resolution Radio Frequency Channel Sounder Based on the Sliding Correlation Principle," *IET Microwaves, Antennas Propagation*, vol. 9, no. 8, pp. 837–846, 2015.

[5] R. Feger, H. Haderer, H. Jalli Ng, and A. Stelzer, "Realization of a Sliding-Correlator-Based Continuous-Wave Pseudorandom Binary Phase-Coded Radar Operating in W-Band," *IEEE Transactions on Microwave Theory and Techniques*, vol. 64, no. 10, pp. 3302–3318, Oct 2016.

[6] X. Corporation, "Xilinx Kintex-7 FPGA KC705 Evaluation Kit," 2019. [Online]. Available: https://www.xilinx.com/products/boards-and-kits/ek-k7-kc705-g.html

[7] ——, "7 Series FPGAs Clocking Resources – User Guide," Jul. 2018.

Novel parabolic dish antenna for RADAR applications

***João R. Reis*[1,2*], *Carlos Ribeiro*[2,3] and *Rafael F. S. Caldeirinha*[1,2]**

[1]*Instituto de Telecomunicações, Leiria, Portugal*
[2]*Polytechnic of Leiria, Leiria, Portugal*
[3]*Twevo, Lda.,Coimbra, Portugal*
[*] *Email: joao.reis@ipleiria.pt*

Keywords: antenna design, microstrip antenna, parabolic reflector, RADAR;

Abstract

In this paper, a novel parabolic dish antenna design, aiming radar applications at 24GHz, is presented. Firstly, a dedicated analysis on the theorectical formulation of reflector dish antennae is conducted, in order to evaluate the main design parameters against antenna performance. This study is used as design guideline for the antenna being proposed in this paper. Subsquently, the design of the novel parabolic dish antenna is described and validated by the means of electromagnitc simulations performed in CST Microwave Studio (CST MWS). The proposed antenna is composed of 4 parts: a paraboloid shape imprinted in a PETG material, a metalic coating layer to enable the shaped paraboloid with EM reflecting properties, a PTFE spacer layer to ensure the focal distance and, finaly, a microstrip feeding source designed on a double side substrate. The final antenna design has a bandwith of 500 MHz centered at 24.125 GHz and 21.1 dBi of gain, meeting with initial project speficiations. The half power beamwidth (HPBW) is of 13° and 14°, in the azimuth and elevation planes, respectively, while the side-lobe levels are of -16° and -18°, for the same antenna planes.

1 Introduction

Radio Detection And Ranging (radar) [1–3] technology has been extensively used through the years, since its appearance in early 1970's [4, 5]. Long range radar has been generically used for target detection and recognition, ranging and air/space surveillance, particularly applied to the military context, civil aviation and space sensing [1]. However, with the continuous evolution of the digital era and chip integration, radar technology becomes rapidly available for small scale applications [6–9]. Mid- and short- range radars are nowadays widely available in the market, through commercially-of-the-shelf (COTS) and system-on-chip (SoC) kits [10–12], facilitating radar deployment. Such RADARs are being particularly used in the automotive [13–15] and UAV markets [16–18], where systems at millimetre wave frequencies, (*e.g.* 24 and 77 GHz frequency bands) have been used for object detection and collision avoidance and to assist with autonomous safe driving.

From a practical point-of-view, radar systems benefit from having high antenna gain to increase the overall system dynamic range, and consequently the range of the radar [1, 2]. Hence, typical antenna designs for radar application comprise either the use of antenna array or reflector antennae. Both antenna topologies are well known for achieving high gains [2, 3]. An antenna array consists of a number of identical antenna elements physically arranged in a certain manner, usually in the same plane, forming a physical array of antennae. Depending on the number of elements (among other factors), the electric fields produced by each radiated element interfere constructively in some directions and, interfere destructively in others, leading to high directivity and gains [2, 3]. On the other hand, reflector antennae are typically composed by a feed source radiating towards a reflecting surface, much larger relative to a wavelength, in order to increase the effective aperture and, thus, the gain [1, 2]. In particular, the parabolic dish is one of the most used forms in reflector antenna designs, since the geometrical properties of the parabola ensures that all the rays originating from its focus get reflected in a direction parallel to the parabola's axis, improving the efficiency of the reflector.

However, the aforementioned designs will ultimately be used depending on the application. For example, reflector antennae are commonly employed in long range Radars, where very high gains and large scanning volumes are required. The gain of a parabolic dish reflector is just a physical constrains and depends on the dish diameter, while large field-of-view (FOV) scanning is achieved by mechanical rotating the arrangement. These characteristics are challenging to mimic with antenna array limited by the feeding network, which complexity and cost increases with the size of the array, yet providing much limited FOV scanning than the previous solution. Nevertheless, antenna arrays are employed in short- and mid-range high frequency radars (>24GHz) in detriment of reflector antennae, due to the easiness of integration in microstrip technology, granting compact and lightweight form factors. For example, many Frequency-Modulated Continuous Wave (FMCW) radar kits [10–12] employ simple linear arrays of microstrip patch antennae to provide enhanced gains, while phase-control to enable beamsteering (and thus larger FOV) is performed on-

the-chip.

To this extent, this paper presents a novel parabolic dish antenna design for radar operating in the 24 GHz radar frequency bands. The antenna being proposed herein is seen as an alternative to antenna array, presenting equivalent gain for the same effective aperture, but less complexity in design. The proposed antenna is composed of 4 layers: i) a PETG (or plastic) layer that shapes the paraboloid format, ii) a coating layer with metallic properties, to enable the shaped paraboloid with EM reflecting properties, iii) a PTFE layer to ensure the focal distance between the parabolic reflector dish and the feeding source, and finally, iv) a microstrip dipole for feeding built on a double sided Rogers RT5880 substrate. A thorough analysis on the parabolic antenna equations is carried out in order to and validated against electromagnetic simulations performed in CST MWS.

This paper is organized as follows: Section 2 reports on the theoretical formulation associated to parabolic reflector antennae, analysing in detail the trade-offs between the main design parameters, *i.e* dish diameter, depth and focal distance. In Section 3, it is presented in detail the design for the proposed parabolic antenna. A set of simulation carried out on CST Microwave Studio is presented to validated the proposed concept. Finally, the main conclusions are drawn in Section 4.

2 Overview of parabolic reflector antenna

The background of parabolic reflector antennae is well documented in many textbooks [1–3]. However, in this section, it is proposed to cover main design parameters such as dish diameter, depth and focal distance, analysing in details the relation that dictates the radiating performance, as Gain and half power beam-width (HPBW). Such study will provide useful insight on the physical parameters to be applied in the antenna design proposed in section 3.

2.1 Main design parameters

The underlying principle of a parabolic dish reflector is depicted in Fig. 1. A feed source distanced at a focal distance F, illuminates a parabolic reflector with diameter D and depth C, which in turn redirects (reflects) the incident spherical wave (near-field interaction) to yield far-field distance immediately off the reflector, thus improving the antenna effective aperture and consequently gain. In fact, these are the main parameters necessary to define the shape of a parabolic dish reflector.

According to [3], the gain (in dB) of parabolic dish antenna, in closed form, is expressed by (1),

$$G = 10\,log_{10}\left[\eta.\left(\frac{\pi.D}{\lambda}\right)^2\right], \quad where \quad \eta = \eta_s.\eta_t.\eta_p.\eta_b, \tag{1}$$

where D is the diameter of the dish, λ the operating wavelength, and η is the aperture efficiency. The aperture efficiency

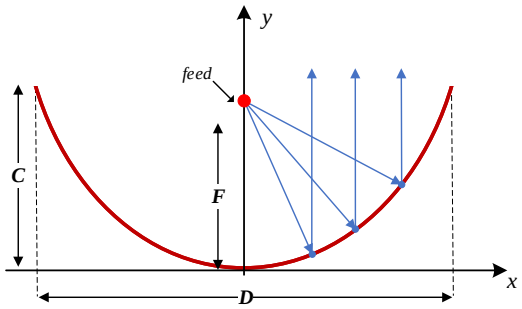

Fig. 1: Generic block diagram of a parabolic dish reflector antenna.

can be defined as the relation of the actual gain to the maximum theoretical gain achievable for the same aperture area. Thus, it is a measure that can relates [2]:

- η_s - splitover efficiency - the total power that is radiated by the feed and intercepted by the reflecting surface;
- η_t - taper or illumination efficiency - the uniformity of the amplitude distribution of the feed pattern over the entire reflector surface;
- η_p - phase efficiency - the phase uniformity of the field over the aperture plane;
- η_b - feed blockage efficiency.

Each of the factors introduced above have significant effect on the total efficiency η and thus, in gain. Typical values for aperture efficiency vary between 0.3 and 0.7 [2], for the antenna configuration of Fig. 1. In fact, this can be seen in Fig. 2a, where the gain of a parabolic reflector antenna is plotted against the reflector diameter (considering λ at 24.125GHz), for several aperture efficiencies η. From the figure (Fig. 2a), it is possible to conclude that the overall efficiency η has considerable impact in the gain specially for larger dish diameters. For example, the gain for a $D = 100$ mm at 24 GHz vary from 27 to 23 dBi, when total aperture efficiency decreases from 0.7 to 0.3. However, not all the efficiency parameters presented above have the same weight in global aperture efficiency η. According to several textbooks [1–3], the ones that contribute the most are splitover (η_s) and taper efficiencies (η_t) which are associated to the radiation pattern of the feeding antenna and how well it is matched to the dish. Hence, the reflector design problem consist mostly of matching the feed antenna pattern to the reflector shape and a compromise between spillover and taper efficiency must exist. For example, very high spillover efficiency can be achieved by a narrow beam pattern with low minor lobes at the expense of a very low taper efficiency [2]. Nevertheless, the traditional rule of thumb for this trade-off is that best efficiency occurs when the illumination at the edge of the parabolic dish is 10 to 11 dB down relative to the one at the centre [1]. However, the -10 dB rule is just a practical consideration that ultimately will depend on the directivity of the feeding source which many not be respected. For example,

a dipole antenna used as feed may not be respect the suggested rule of thumb since exhibit an omnidirectional pattern in one of its planes.

Notwithstanding, equation (2) estimates the edge direction θ_{max} in which the feed pattern is suggested to be attenuated, as mentioned. In Fig. 2b it is represented the edge direction for several focal-length-to-diameter (F/D) ratios, a measure that gives the curvature rate of the parabola.

$$\theta_{max} = 2.tan^{-1}\left(\frac{1}{4.(F/D)}\right) \tag{2}$$

According to Fig. 2b, as the F/D ratio approach to infinity the dish becomes planar ($\theta_{max} = +\infty$). If the F/D is set to 0.25, the focal point is in the same plane of the dish rim ($\theta_{max} = 90°$). Furthermore, it is worth to mention that F/D ratio also defines the physical position of the feed and the dish depth, as it can been seen from figures 3a and 3b, respectively. While Fig. 3a traces the relation between reflector diameter and focal distance, for several F/D ratio, Fig. 3a diameter depth for the same diameter range, also for several F/D ratio using the expression (3):

$$C = \frac{D^2}{16.F} = \frac{D}{16.(F/D)} \tag{3}$$

Finally, another parameter that can be estimated from the physical properties of the reflector is the HPBW. According to [3], an approximation the HPBW can be obtained using (4):

$$HPBW = 70°.\frac{\lambda}{D}. \tag{4}$$

2.2 Design guideline

According to the considerations specified in the previous section, this paper follows the subsequent guideline, which is will assist with the antenna designs being presented in this paper.

1. Obtain the dish diameter using (1) and/ or Fig. 2a, for a desired gain. Since the efficiency is not known at this point, an initial efficiency of $\eta = 0.5$ can be considered;
2. Analyse the radiation pattern of the feeding antenna. Obtain the direction in degrees, in which its gain is 10 to 11 dB lower than at boresight. Use the angle to find the F/D ratio through (2) and/ or Fig. 2b;
3. Calculate the focal distance F through the F/D ratio (depicted in Fig. 3a) and the dish depth C, using (3) and/ or Fig. 3b;
4. Optimise the design to achieve the best efficiency η.

3 Proposed Antenna design and simulation

The antenna proposed in the paper takes into consideration the following project specifications/requirements: i) the frequency

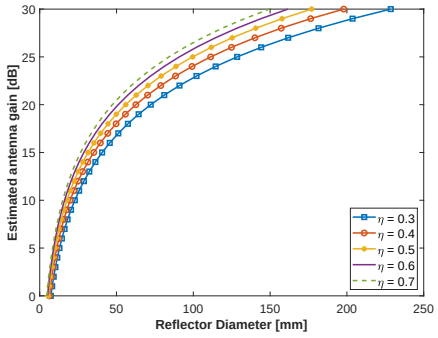

(a)

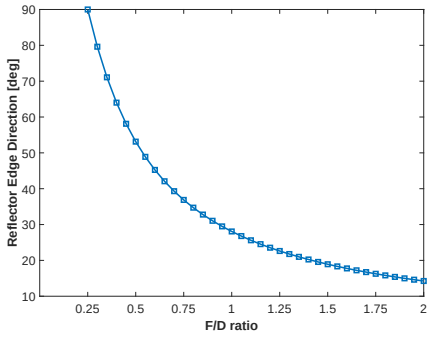

(b)

Fig. 2: Parabolic reflector main parameters: (a) dish diameter *vs.* total gain and, (b) F/D ratio *vs.* edge direction (θ_{max}).

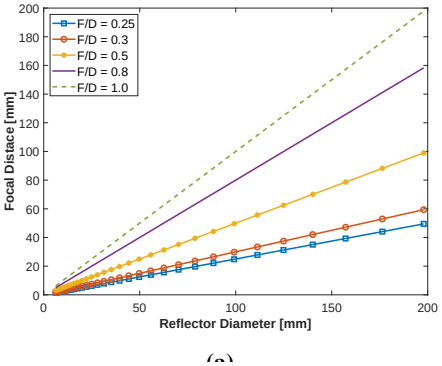

(a)

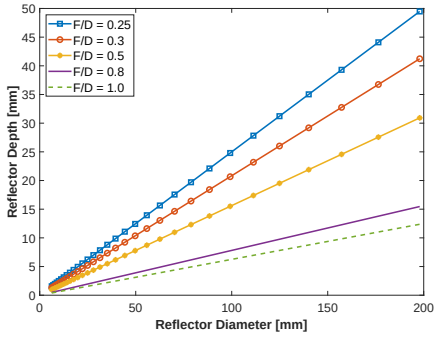

(b)

Fig. 3: Parabolic reflector main parameters: (a) Focal distance and (b) reflector depth *vs.* reflector diameter, for several F/D ratio.

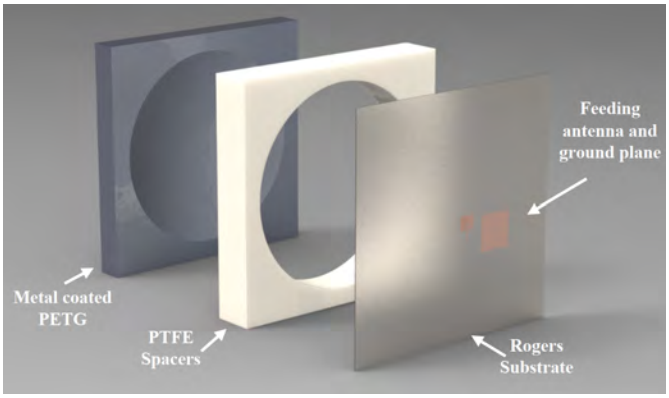

Fig. 4: Block diagram of the proposed 24GHz mono-block radar antenna.

of operation is at 24.125 GHz, corresponding to central frequency of the 24 GHz ISM radar band; ii) a bandwidth of 500 MHz should be achieved, to cover entirely the ISM band and, iii) a total gain of 20dBi should be reached, while keeping the side-lobe level below -12 dB. In order to keep the design compact and lightweight, the mono-block configuration of Fig. 4 has been considered. The reflector antenna is then composed of 4 layers: i) a PETG layer that shapes the paraboloid format, easily produced using 3D printing techniques, ii) a metallic coating to enable the surface of the paraboloid with EM reflecting properties, iii) a PTFE layer to ensure the focal distance between the parabolic reflector dish and the feeding source, and finally, iv) a microstrip feeding antenna as radiating source. This section details the design and simulation of each antenna part, following the design guideline presented in section 3.

3.1 Feed design

As a feeding source, the microstrip patch antenna with reduced ground plane represented in Fig. 5, has been considered. This particular antenna layout was selected due to its radiating properties which can be easily manipulated by slightly changing/optimizing the layout (and thus adapted to the reflector if necessary), and due to the simple and low-cost manufacturer process.

The microstrip patch antenna, implemented following the design recommendations of [2], is designed on double side Rogers RT5880 substrate, with $\epsilon_r = 2.2$, $tan\delta = 0.0009$ and a thickness of 0.254mm. Accordingly, the layout of Fig. 5a has been etched in one of the sides of the substrate, while on the other side, a trimmed ground plane with the shape of Fig. 5b has been considered. The ground plane is trimmed in comparison with typical patch designs, in order to reduce the overall feed blockage. Both top and bottom layer patches, defined by $T_w \times T_l$ and $B_w \times B_l$ respectively, are aligned each other and centred with the substrate. Moreover, in the top plane, a 50Ω feed line, with length F_l and width F_w, insets the patch by I_l connecting it to a feeding port (waveguide port in CST MWS)

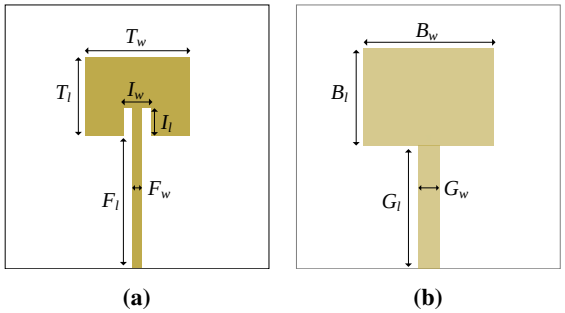

Fig. 5: (a) Top and (b) bottom layer of the feeding microstrip patch antenna (dimensions represented out of scale).

at the edge of the substrate. Similarly, on the bottom plane, a metallic line with dimensions G_l and G_w are placed over the 50Ω feed line.

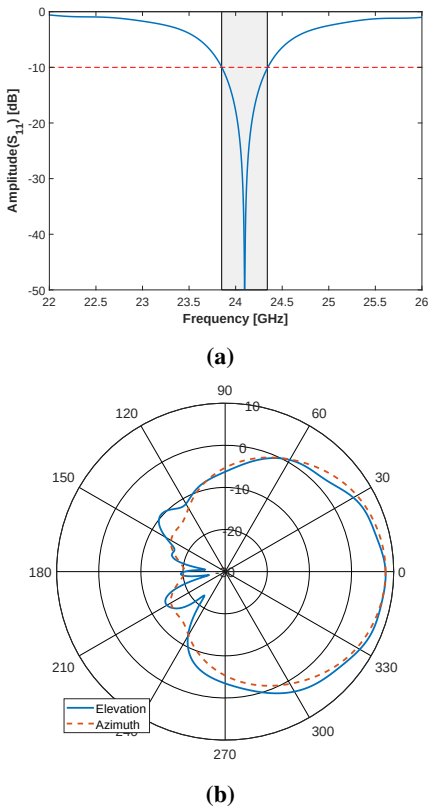

Fig. 6: Simulated results for the optimized feed antenna: (a) S_{11}-parameter and (b) radiation pattern in the two main antenna planes.

After optimisation in CST MWS environment, an antenna with dimensions of: $T_w = 4.9$ mm, $T_l = 4.05$ mm, $I_w = 1.27$ mm, $I_l = 1.3$ mm, $F_w = 0.77$ mm, $F_l = 27.97$ mm, $B_w = 10$ mm, $B_l = 10$ mm, $G_w = 3$ mm, $G_l = 25$ mm and a substrate with 60×60 mm^2, exhibits the S_{11}-parameter depicted Fig. 6. According to the result, the antenna is resonating at 24.125 GHz, presenting a relatively good impedance matching for the frequency range defined between 23.850 GHz and

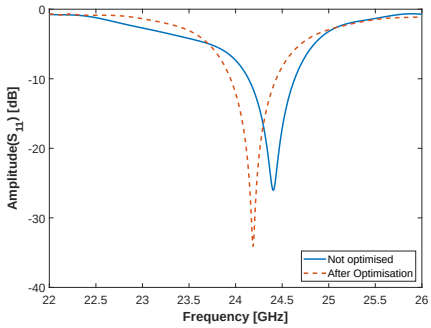

Fig. 7: Simulated S_{11}-parameter of the reflector antenna.

24.350 GHz, *i.e.* $S_{11} < -10$ dB, conferring a bandwidth of 500 MHz. At the design frequency, it exhibits a gain of 7.85 dBi with -0.26 dB of radiation efficiency. As demonstrated in Fig. 6b, the radiation pattern in the azimuth and elevation planes present a relatively good symmetry, with a respective HPBW of 74° and 72°. The direction θ_{max} for this particular feed, *i.e.* direction in which the total gain decays in around 10 to 11 dB relative to max gain direction, is considered to be at $\pm 70°$, in both main antenna planes.

3.2 Overall assembly

To compose the configuration represented in Fig. 4, a parabolic of revolution with 56 mm of diameter and 10 mm deep, has been considered. The diameter has selected according to equation (1) (and Fig. 2a), with $\eta = 0.5$, in order to provide a $G = 20$ dBi and, to comply with the project specifications.

The paraboloid is imprinted on PETG material ($\epsilon_r = 2.6$, $tan\delta = 0.02$), with dimensions of $60 \times 60 \times 22$ mm^3. In order to enable reflection of the EM waves, the PETG block is coated with a 0.2 mm thick copper layer. Perfect electric conductor (PEC) is considered in MWS for simulation purposes.

A F/D of 0.35 is used to meet with the design specifications indicated in point (2) of the guideline (Section 2.2), *i.e.* for a $\theta_{max} = 70°$ the recommended F/D ratio is of 0.35, according to (2b). This confers to the design a focal distance of 21 mm (and dish depth 10 mm). Due to this fact, a PTFE layer ($\epsilon_r = 2.1$, $tan\delta = 0.0002$) with dimensions of 60×60 mm^2 and 11 mm of thickness, is applied between the reflector dish rim and the microstrip patch feeding antenna.

According to simulations, the overall antenna design also presents a relatively good S_{11} impedance matching, as depicted in Fig. 7. However, in a first instance, an offset of the resonance frequency in $+290$ MHz was observed, when comparing to the one for the feeding antenna only (Fig. 6a). Yet, after optimisation, the resonant value was set back to 24.125 GHz (Fig. 7) by fine tuning the parameter I_w, presenting a bandwidth of 500 MHz.

The optimised version of the antenna, exbibits now a total gain of 21.1 dBi with an HPBW of 13° and 14°, in azimuth and elevation planes respectively, as depicted in Fig. 8a. The side-

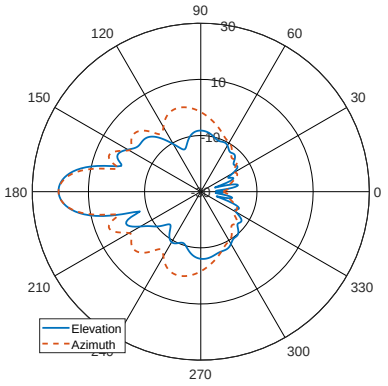

(a)

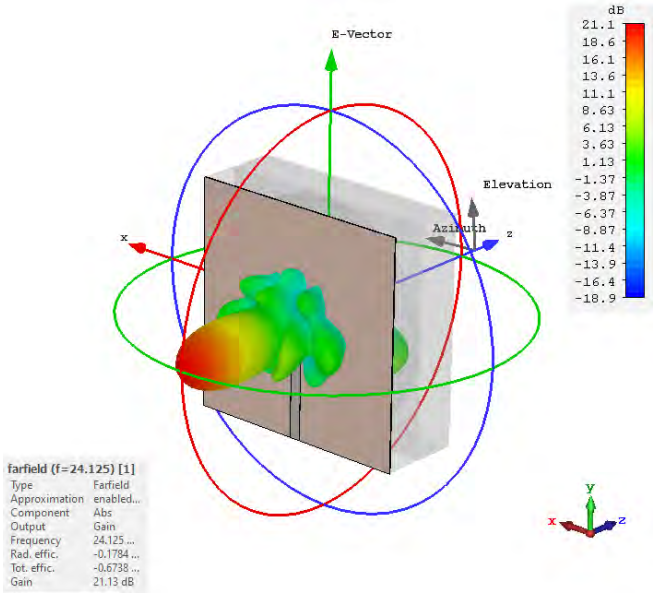

(b)

Fig. 8: Simulated radiation patterns: (a) radiation pattern cut in the two main antenna planes and, (b) snapshot of 3D radiation pattern plus final structure in CST MWS.

lobe levels are of $-16°$ in azimuth and $-18°$ in the elevation planes.

4 Conclusions

This paper presents a novel and compact design of a high gain parabolic antenna. Firstly, an overview on the main reflector antenna parameters are performed. This yield to the elaboration of a antenna design guideline. Subsequently, simulation results a mono-block, high gain, parabolic antenna are presented. The design of a microstrip patch with reduced ground plane, is introduced. Such design is intentionally implemented to be used as feeding source and improve feed blockage. The feeding antenna is designed and optimised to operate at 24.125 GHz, *i.e.* the centre of the 24GHz radar ISM band. The final antenna model exhibits, according to simulations, 21.1 dBi of gain, 500 MHz of bandwidth, a HPBW of

13° and 14°, in the elevation planes, respectively, and side-lobe levels of -16° and -18°, for the same antenna planes. Further work will aim at production and characterisation of the proposed antenna design.

Acknowledgements

This work is partially supported the European Regional Development Fund (FEDER), PO CENTRO/SI-IDT, Project RADAVANT (03/SI/2017 - Project n.º 033907) and by the Portuguese Government, Foundation for Science and Technology, FCT, through the financial support provided under UID/EEA/50008/2019.

References

[1] M. Skolnik, *Radar Handbook*, third edition ed., ser. Electronics electrical engineering. McGraw-Hill Education, 2008. [Online]. Available: https://books.google.pt/books?id=76uF2Xebm-gC

[2] C. A. Balanis, *Antenna Theory: Analysis and Design, 4th Edition*. John Wiley & Sons, 2016.

[3] S. J. Orfanidis, *Electromagnetic Waves and Antennas*, S. J. Orfanidis, Ed. Rutgers University, 1999-2016. [Online]. Available: http://ece web1.rutgers.edu/ orfanidi/ewa/

[4] L. Brennan, "Angular Accuracy of a Phased Array Radar," *IRE Transactions on Antennas and Propagation*, vol. 9, no. 3, pp. 268–275, May 1961.

[5] K. Molz, "The AN/FPS-85 Satellite Tracking Phased Array Radar," *IEEE Transactions on Aerospace*, vol. 2, no. 2, pp. 135–138, April 1964.

[6] C. Li, Z. Peng, T. Huang, T. Fan, F. Wang, T. Horng, J. Muñoz-Ferreras, R. Gómez-García, L. Ran, and J. Lin, "A review on recent progress of portable short-range noncontact microwave radar systems," *IEEE Transactions on Microwave Theory and Techniques*, vol. 65, no. 5, pp. 1692–1706, May 2017.

[7] E. Öztürk, D. Genschow, U. Yodprasit, B. Yilmaz, D. Kissinger, W. Debski, and W. Winkler, "A 60-ghz sige bicmos monostatic transceiver for fmcw radar applications," *IEEE Transactions on Microwave Theory and Techniques*, vol. 65, no. 12, pp. 5309–5323, Dec 2017.

[8] G. Pyo, C. Kim, and S. Hong, "Single-antenna fmcw radar cmos transceiver ic," *IEEE Transactions on Microwave Theory and Techniques*, vol. 65, no. 3, pp. 945–954, March 2017.

[9] Z. Peng, J. M. Muñoz-Ferreras, Y. Tang, C. Liu, R. Gómez-García, L. Ran, and C. Li, "A portable fmcw interferometry radar with programmable low-if architecture for localization, isar imaging, and vital sign tracking," *IEEE Transactions on Microwave Theory and Techniques*, vol. 65, no. 4, pp. 1334–1344, April 2017.

[10] Infineon, "DEMO DISTANCE2GO - Infineon radar demo board." [Online]. Available: https://www.infineon.com/cms/en/product/evaluation-boards/demo-distance2go/

[11] ——, "DEMO SENSE2GOL - Infineon radar demo board." [Online]. Available: https://www.infineon.com/cms/en/product/evaluation-boards/demo-sense2gol/

[12] T. Instruments, "AWR1642 single-chip 76-GHz to 81-GHz automotive radar sensor." [Online]. Available: https://www.infineon.com/cms/en/product/evaluation-boards/demo-sense2gol/

[13] *Automotive radar: Status and trends*, 2005.

[14] W. Menzel and A. Moebius, "Antenna Concepts for Millimeter-Wave Automotive Radar Sensors," *Proceedings of the IEEE*, vol. 100, no. 7, pp. 2372–2379, July 2012.

[15] U. Chipengo, "Full physics simulation study of guardrail radar-returns for 77 ghz automotive radar systems," *IEEE Access*, vol. 6, pp. 70 053–70 060, 2018.

[16] J. S. Patel, F. Fioranelli, and D. Anderson, "Review of radar classification and RCS characterisation techniques for small UAVs or drones," *IET Radar, Sonar Navigation*, vol. 12, no. 9, pp. 911–919, 2018.

[17] M. García Fernández, Y. Álvarez López, A. Arboleya Arboleya, B. González Valdés, Y. Rodríguez Vaqueiro, F. Las-Heras Andrés, and A. Pino García, "Synthetic aperture radar imaging system for landmine detection using a ground penetrating radar on board a unmanned aerial vehicle," *IEEE Access*, vol. 6, pp. 45 100–45 112, 2018.

[18] M. Lort, A. Aguasca, C. López-Martínez, and T. M. Marín, "Initial evaluation of sar capabilities in uav multicopter platforms," *IEEE Journal of Selected Topics in Applied Earth Observations and Remote Sensing*, vol. 11, no. 1, pp. 127–140, Jan 2018.

URSI GASS 2020, Rome, Italy, 29 August - 5 September 2020

STDCC radar at 24 GHz: first measurement trials

André Sardo[(1)(2)], João R. Reis[(1)(2)], Luis Duarte[(1)(2)], Nuno Leonor[(1)(2)], Carlos Ribeiro[(1)(3)] and Rafael F. S. Caldeirinha[(1)(2)].
(1) Polytechnic Institute of Leiria, Leiria, Portugal
(2) Instituto de Telecomunicações - Leiria, Portugal
(3) TWEVO *Lda.*, Coimbra, Portugal

Abstract

This paper presents the first measurement trials for performance assessment of a real-time and high resolution monostatic radar operating at 24 GHz. The proposed real-time radar, which operates based on the sliding correlation of pseudo-noise (PN) sequences, provides a high time resolution better than 4 ns, useful for moving target identification (MTI) in the presence of highly dense clutter, under harsh environments and severe weather conditions (fog, snow and fire smoke or plume). The STDCC radar target detection capability is demonstrated in this paper, by measuring and identifying the radar data for 4 distinct scenarios, composed of multiple targets (up to 8), inside an anechoic chamber, demonstrating the potential of the proposed radar architecture.

1 Introduction

Radar technology has been used for many years, but its constant evolution is a demand due to the intensive interest of automotive and drone industry, to assist in autonomous driving and collision avoidance. To date, many radar topologies have been presented in the literature [1], but mostly are based on Frequency Modulated Continuous Wave (FMCW) technique. This technique, however, shows limited performance in heavy cluttered environments, where interference from other radars or communications may significantly degrade the radar's detection capability. Alternatively, Orthogonal Frequency Division Multiplexing (OFDM) is being proposed in [1, 2], to overcome the FMCW limitations. Nevertheless, the OFDM-based radars require high computational resources typically available in Field-Programmable Gate Array (FPGA) based architectures, in addition to expensive analogue-to-digital converters (ADC), making its implementation both inefficient and cost prohibitive for mass production. On the other hand, radar signal processing based on all-digital pseudo-noise (PN) sequences represents a quantum leap in future radar front-end architecture, presenting significant advantages in terms of low baseband computational demands and yielding a plethora of opportunities for massive deployment applications, *e.g.* autonomous driving scenario.

With this mindset, it is presented in this paper the first trails on a Swept Time-Delay Cross-Correlator (STDCC) PN Radar at 24 GHz. The proposed radar architecture, being described in this paper, follows the STDCC principle well covered in [3–6] and it is sought to mitigate incumbent and mutual interference risks, given its excellent autocorrelation properties. The experimental results included in this paper, demonstrate the potential of the proposed technique by clearly detecting and identifying 8 distinct metallic targets at 24GHz.

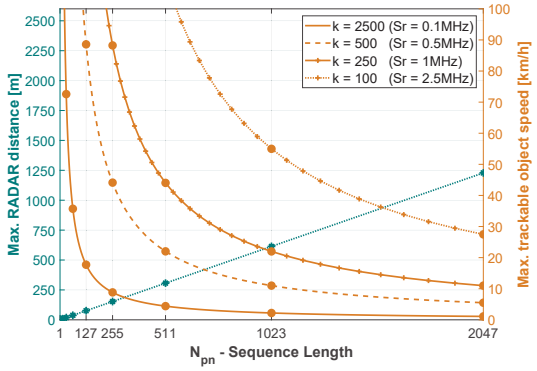

Figure 1. STDCC radar: maximum unambiguous distance and trackable object speed *vs.* N_{pn} sequence length, for a F_{tx} = 250MHz.

This paper is organised as follows: section 2 gives details about the proposed STDCC radar architecture, including a brief summary of the STDCC principle, the baseband signal generation in the digital domain, and finally, the radar architecture, including RF and IF stages. In section 3, the practical setup and the measurements scenarios are being described followed by a critical analysis of the experimental results. Finally, the main conclusions are drawn in section 4.

2 STDCC radar architecture

2.1 Radar principle

The STDCC PN radar proposed herein, explores the autocorrelation properties of PN sequences [3–6], particularly those of the type of maximal length. In this monostatic

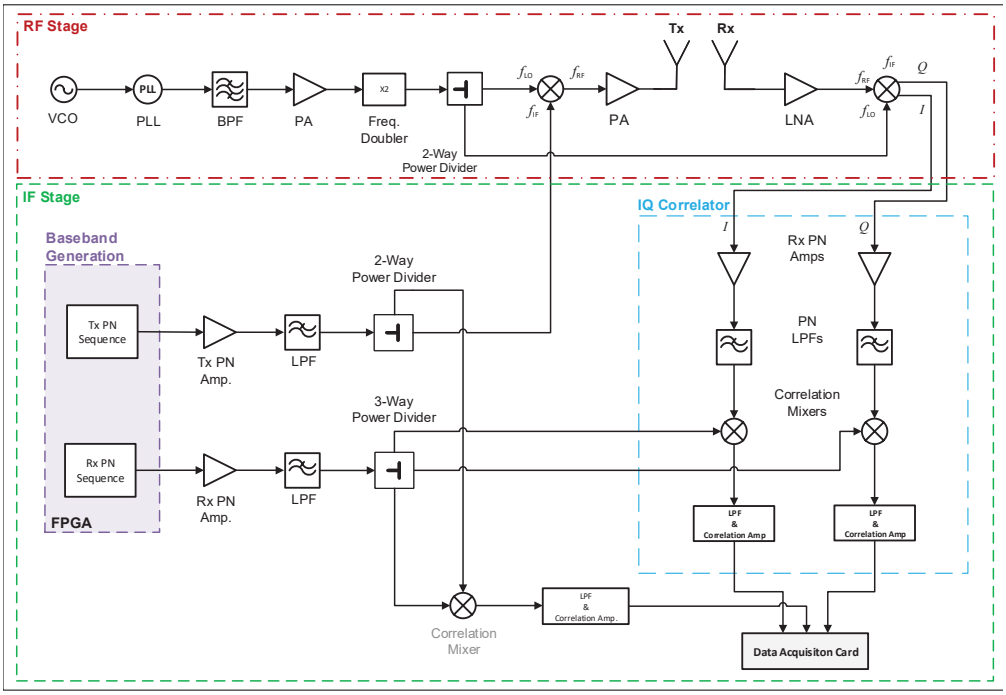

Figure 2. Block diagram of the STDCC radar architecture.

configuration (Fig. 2), two similar PN sequences are generated in the baseband of which, one is transmitted through the radio channel and the other shared directly with the receiver. At the receiver end, both PN sequences are correlated against each other to extract the radar channel information. Since both PN sequences are generated at two different rates, they 'slide' against each other in the time domain, effectively spreading (time-dilating) the multipath (or several target echoes) components out in time, at the output of the correlator. Thus, the maximum theoretical unambiguous distance for a target object to be detected, in metres, only depends on the PN sequence length (N_{pn}) and on the chip frequency (F_{tx}), while the maximum trackable object speed is set by frequency difference between the two generated sequences, denominated of slip-rate (Sr). In Fig. 1 it is presented the maximum theoretical unambiguous distance for the STDCC radar, for various N_{pn} sequences length and slip-rate settings. This is sought to provide the radar with high agility to adapt itself to different application scenarios, *e.g.* short and long range.

2.2 Baseband generation

The radar baseband generation, where PN sequences are being generated, is a subpart of the IF stage of the proposed radar architecture depicted in Fig. 2. In particular, a Xilinx Kintex-7 KC705 FPGA [7] has been used to generate the receiver and transmitter PN sequences. Real-valued bipolar maximum length PN binary sequences with $N_{pn} = 511$ points are generated in the FPGA and then outputted in its unipolar digital pins, with 250.1 MHz and 250 MHz clocks (Sr = 100 kHz), for the transmitter (Tx) and receiver (Rx), respectively. This technique allows the creation of an analogue baseband signal and eliminates the need for expensive high-speed Digital-to-Analogue Converters (DAC) daughter boards. The physical implantation baseband generation in algorithm and is explained with more detail in [6].

2.3 RF and IF architectures

The RF stage initiates in a high precision Voltage Controlled Oscillator (VCO) controlling a Phase-Locked Loop (PLL) to output the necessary 24 GHz. This, in turn is divided to source both mixers to up-convert and down-convert the baseband signal (IF). At the Tx mixer, the resulting signal is amplified to appropriate output power levels up to the limits of interest for the radar. At receiving end, the Rx mixer demodulates the channel radio signal into a differential signal with In-phase (I) and In-quadrature (Q) components, feeding into the IQ correlator block in the IF stage. *X-Microwave* technology was employed to achieve the mentioned RF stage (front-end) of the radar, allowing fast prototyping with their modular building block ecosystem for microwave components. The antennas used for this system were two identical 20 dB gain horn antennas (*Flann* 22240-20), located side-by-side.

In the IF stage, both I and Q received components are amplified and filtered before being fed into the correlation mixers, where the correlation is performed with the Rx PN sequence as previously mentioned in section 2.2. Further signal conditioning is performed in order to be properly captured by an ordinary data acquisition card (*Picoscope* 3406-D MSO). Besides the I and Q acquisition of the received signal, the correlation result between a copy of both

receiver and transmitter sequences is also acquired, in order to obtain clear temporal reference. These signals were then processed in real-time to estimate the targets distance and obtain a plan-position-indication (PPI), as it will be discussed next section.

3 Radar performance evaluation

3.1 Experimental setup

In order to assess the performance of the proposed radar, four distinct scenarios were assembled inside an anechoic chamber, in a 1-pole, 2-pole, 7-pole and 8-pole configuration, respectively. These scenarios were prepared to assess the radar's ability to detect targets in close proximity. The poles are composed of metal with 6 cm of diameter and 2 m of height, and are disposed inside a 6x5x2 m anechoic chamber, as indicated Fig. 3a. The radar was placed on top on a motorised rotating table, in the centre of the chamber, and it was made to rotate around its vertical axis. For all geometries, the radar system under test was made to rotate 360° with a 0.5° steps increment. For every angular step, 20 radar acquisitions have been measured, averaged (Power Delay Profile) and processed to obtain a PPI and assess the target identification performance. After processing, the results are then displayed in two different graph types: waterfall and polar plot, as depicted in Figs. 4 and 5, respectively. The waterfall plots represent the measured average PDP, where the x-axis corresponds to each measured azimuth angle and the y-axis corresponds to the detected radar distance. The polar plot depicts all detected peaks, at every angle, after applying a simple peak-detection algorithm.

3.2 Experimental results

The first measurement scenario considered a single metallic pole placed 1 m apart of the proposed radar aperture at boresight direction, where $\theta = 0°$ (Fig. 3a). According to the results, depicted in Fig. 4a and Fig. 5a, it is possible to observe the single target to be accurately detected by the STDCC radar. The target peak is correctly being identified inside the anechoic chamber at 1 m distance and at 0° in the boresight direction of the radar aperture, which is clearly visible in Fig. 5a. The colour variation gradient visible in the result occurs due to the radiation pattern of the antennae, which exhibits a half-power beam-width of around 23°, in both azimuth and elevation planes, at the considered frequency.

The second set of measurements was performed by adding an extra pole at a distance of 1.6 m and steered off 10° from the boresight direction ($\theta = 10°$), to the previous scenario. As depicted in Fig. 4b, both targets are also being detected and, in fact, they can be easily distinguished from each other. The estimated distances of both poles are confirmed by the polar plot of Fig. 5b, at $\theta = 0°, d = 1$m for the first target and at $\theta = 10°, d = 1.6m$, for the second target, corresponding to their real physical position inside the chamber.

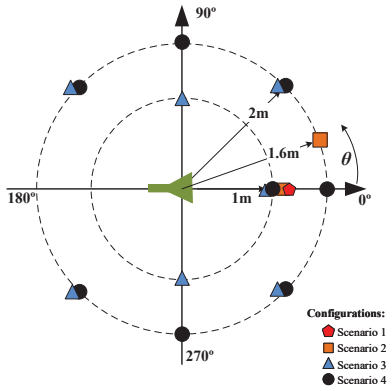

(a)

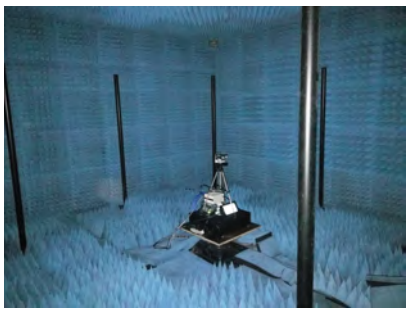

(b)

Figure 3. Experimental setup: (a) scenario setup for benchmarking and, (b) photography inside anechoic chamber.

For the third scenario, 7 poles were placed in an alternating fashion, at 1 m and 2 m apart of the radar with 45° increments starting from $\theta = -135°$. The proper detection of all 7 targets is visible in Fig. 4c. The correct angles of detection can be seen in Fig. 5c, as each pole is detected at the angles of $\theta = -135°, -90°, -45°, 0°, 45°, 90°$ and 135°. Although a few artefacts can be observed in the vicinity of the poles located at 1 m apart from the radar, these are still located well within the the spacial resolution of the radar.

As for the last scenario, Fig. 4d clearly shows the correct detection of all targets, where the 7 poles are located at 2 m apart at the same angles as the previous scenario and a single pole placed at 1 m apart at the angle $\theta = 0°$, including the same artifacts as the previous scenario. Most notably, the target placed at $\theta = 0°$ and 2 m further away is also being detected, despite of the fact it is masked by the first pole (no direct line of sight). Although the angle of this pole is being detected as being at around 7° in Fig. 5d, due to the *shadowing* of the pole at 1 m, the remaining poles detection was performed successfully.

For all the results presented, a maximum range error of only 9 cm between the reported distance and the effective physical distance have been detected. This error is acceptable, as it falls within the spacial precision associated with the used radar bandwidth. The signal level difference of around 7-9 dB between the poles depicted in Fig. 4b occurs due to the excess path loss corresponding to the travel distance

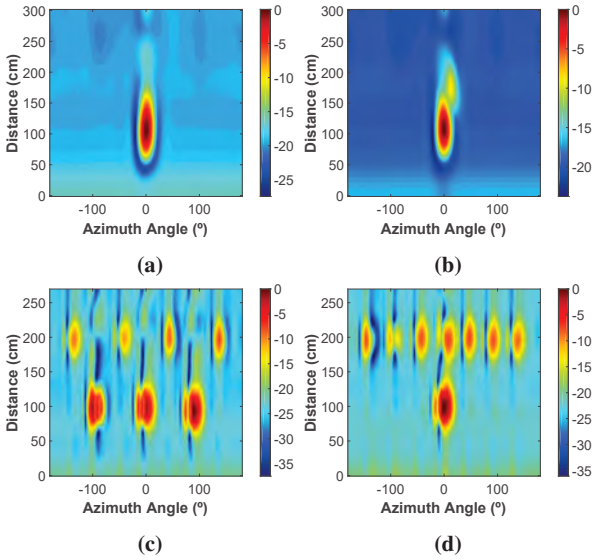

Figure 4. Waterfall PPI - normalised gain (in dB) *vs.* scanning angle, for: (a) 1-pole (b) 2-pole (c) 7-pole and (d) 8-pole, scenario.

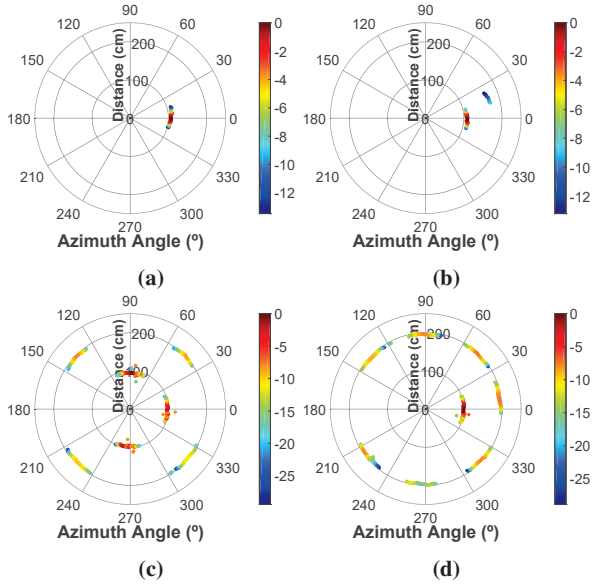

Figure 5. Polar PPI: Normalised gain (in dB) *vs.* scanning angle, for each experimental scenario: (a) 1-pole (b) 2-pole (c) 7-pole (d) 8-pole.

between the poles (i.e. 1.2 m), in addition reflection loss introduced by the second pole (i.e around 2 dB).

4 Conclusions

This paper presents the first results on STDCC radar based on PN sequences. The radar architecture including baseband generation, RF front-end and IF stage are detailed in this manuscript. Subsequently, experimental results performed inside an anechoic chamber are presented and discussed. Four distinct scenarios have been considered by disposing multiple artificial targets at different locations around the radar sensor. The proposed radar not only successfully detected and the targets on multi-clutter environment but also accurately identified the absolute position (distance and angle from boresight) of each target, with a range error of only 9 cm, which falls within the radar resolution. This results prove and validate the usefulness of the STDCC technique applied in radar, representing a quantum leap in radar future front-end architecture.

5 Acknowledgements

This work is partially funded by Research and Technological Development Incentive Scheme CO-PROMOTION - Centro2020 - P2020 - European Regional Development Funds, under project RADAVANT - Radar for Detection and Avoidance in Unmanned Aerial Vehicles (PI nr. 033907) and by FCT/MCTES UIDB/EEA/50008/2020.

References

[1] W.Wiesbeck and L. Sit, "Radar 2020: The future of radar systems," *International Radar Conference*, pp. 1–6, Oct. 2014.

[2] J. S. A. Gameiro, D. Castanheira and P. P. Monteiro, "Research Challenges, Trends and Applications for Future Joint Radar Communications Systems," *Wireless Personal Communications*, vol. 100, no. 1, pp. 81–96, May 2018.

[3] R. J. Pirkl and G. D. Durgin, "Optimal Sliding Correlator Channel Sounder Design," *IEEE Transactions on Wireless Communications*, vol. 7, no. 9, pp. 3488–3497, Sep. 2008.

[4] D. Ferreira, R. F. S. Caldeirinha, and N. Leonor, "Real-time High-resolution Radio Frequency Channel Sounder Based on the Sliding Correlation Principle," *IET Microwaves, Antennas Propagation*, vol. 9, no. 8, pp. 837–846, 2015.

[5] R. Feger, H. Haderer, H. Jalli Ng, and A. Stelzer, "Realization of a Sliding-Correlator-Based Continuous-Wave Pseudorandom Binary Phase-Coded Radar Operating in W-Band," *IEEE Transactions on Microwave Theory and Techniques*, vol. 64, no. 10, pp. 3302–3318, Oct 2016.

[6] R. F. S. Caldeirinha, J. R. Reis, A. Sardo, L. Duarte, N. Leonor, J. Gil, and C. Ribeiro, "Disruptive future of radar based on all-digital PN signal processing," in *2019 IEEE-APS Topical Conference on Antennas and Propagation in Wireless Communications (APWC)*. IEEE, sep 2019.

[7] X. Corporation, "Xilinx Kintex-7 FPGA KC705 Evaluation Kit," 2019. [Online]. Available: https://www.xilinx.com/products/boards-and-kits/ek-k7-kc705-g.html

All-digital reconfigurable STDCC radar baseband implementation in FPGA

Luís Duarte[1,2,3], Carlos Ribeiro[1,4], Luís N. Alves[3] and Rafael F.S. Caldeirinha[1,2]
[1]Polytechnic of Leiria, Leiria, Portugal
[2]Instituto de Telecomunicações - Leiria, Portugal
[3]Universidade de Aveiro, Aveiro, Portugal
[4]TWEVO, Coimbra, Portugal

***Abstract*—This paper reports the architecture of an all-digital Swept Time-Delay Cross-Correlator (STDCC) baseband. Until recently, the sliding correlator technique has been mainly employed for sounding the radio propagation channel. However, recent benchmarks have shown promising results in target detection context when compared to commercially available solutions. STDCC takes advantage of the sliding correlation properties of Pseudo-Noise (PN) sequences. Therefore, this paper presents the baseband generation for this new radar technique with on-the-fly sequence tuning using a Field-Programmable Gate Array (FPGA). The reconfigurable STDCC radar baseband generates both PN sequences digitally and requires a low-cost ADC to acquire the time dilated result. At the end, the proposed architecture is evaluated regarding resource usage efficiency and then the radar performance will be discussed in terms of the all-digital PN sequence spectrum and the real-time slide correlation. Our analysis confirmed a strong correlation between both sequence length and sampling frequency with radar detectable distance.**

***Index Terms*—RADAR, STDCC, PN sequences, FPGA.**

I. Introduction

RAdio Detection And Ranging (RADAR) has been in existence for nearly a century with an initial interest towards military applications. In the last decade, radar has been extensively studied for many other applications, but it is foreseen that, in the near-future, drone and automotive industries will massively deploy such technology. Consequently, such a continuously growing trend encourages the development of novel radar technologies with sophisticated algorithms and with new waveforms able to mitigate radar interference.

Until recently, the radar waveform commonly employed for drone and automotive sectors was called Frequency-Modulated Continuous Waveform (FMCW) [1]. Such technique transmits a continuous wave that varies the frequency with respect to time, which achieves a saw-tooth frequency modulation sweep. However, with the envisioned number of radars skyrocketing, the FMCW will soon fall victim of its own success, as radar interference will degrade the target detection capability [2].

That said, new waveforms started to be proposed in order to mitigate the multiple radar interference. There have been many proposals in the literature using noise radar waveform resorting to Pseudo-Noise (PN) sequences. Besides good interference immunity, the PN radar technology has good auto correlation properties, leading to high range resolution, but it also provides low probability of interception [3]. However, since PN sequences are generated digitally resorting to powerful devices

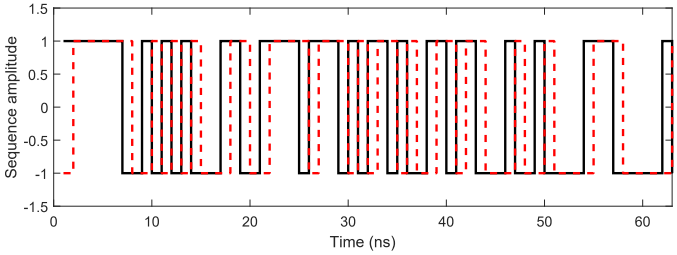

Fig. 1: Sliding correlation principle.

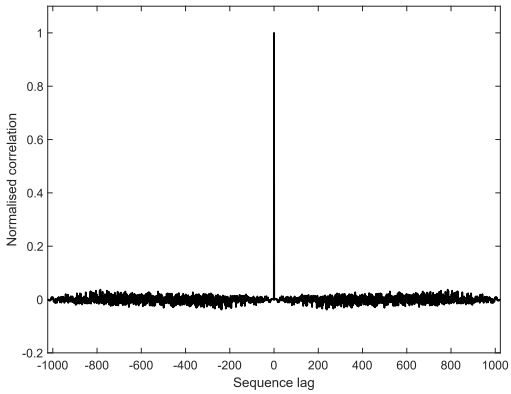

Fig. 2: Autocorrelation result for an m-sequence, m=10.

with DSP capabilities (FPGAs), it then requires high-speed converters to do their conversion to the analogue domain. This latter characteristic is not ideal due to the added costs associated with ADC and DAC acquisition.

The baseband radar architecture herein proposed is based on the Swept Time-Delay Cross-Correlator (STDCC) technique, which is well explained in the literature [4]–[6]. This technique uses the sliding correlation of PN sequences (Fig. 1 and 2), which were implemented without using a DAC (all-digital). In [6], such STDCC radar operating at 24 GHz is benchmarked with a commercially available of-the-shelf FMCW solution. Considering that STDCC radar performance showed promising results, it is this work ambition to propose an improved STDCC baseband architecture to tune on-the-fly the radar parameters according to user needs.

This paper is organised as follows: section II details briefly the STDCC principle. Section III describes the proposed reconfigurable STDCC baseband architecture, giving emphasis on the sequence generation, as well as, their sampling fre-

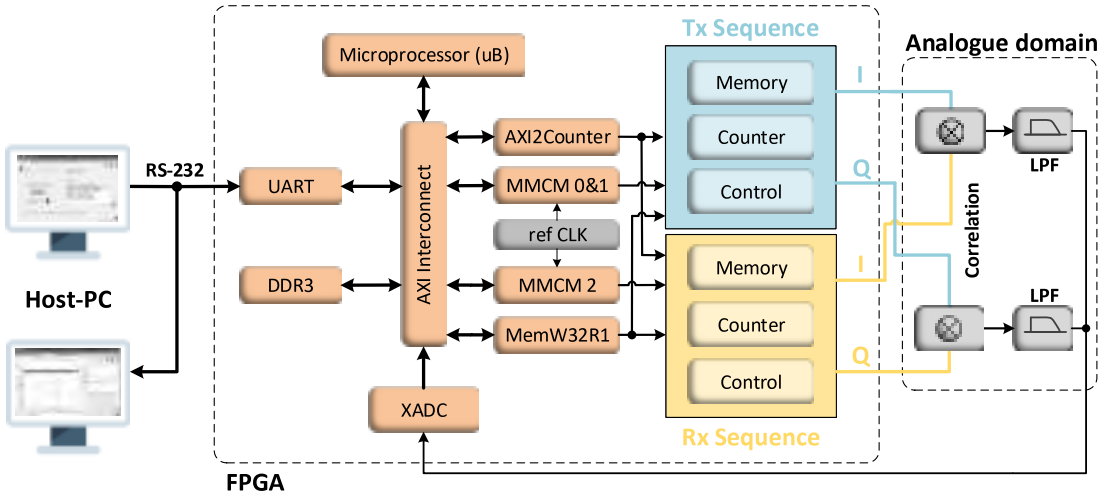

Fig. 3: Block diagram of reconfigurable STDCC radar architecture.

quency clock generation. In section IV, the radar baseband performance is assessed in terms of resource usage, followed by the digitally generated sequence quality and culminating in their correlation results. Finally, the main conclusions are addressed in section V.

II. STDCC PRINCIPLE

As previously stated, the STDCC PN radar explores the auto-correlation properties of PN sequences. Such radar generates two identical PN sequences that are sampled at slightly different rates. As is depicted in Fig. 1, by adjusting the receiver PN sequence with a slightly slower clock, both sequences will slide with one another. When the receiver sequence (slower rate) has a perfect alignment with its counterpart, a peak value appears in the correlation output. Fig. 2 shows the correlation result, simulated in MatLab, where two PN sequences with a length of 1023 bits were correlated with the cross-correlation function. Note that the peak correlation value appears with zero sequence lag, which is when both sequences are perfectly aligned.

The sliding correlation is time dilated by a sliding factor of k, and is given by (1) [7]. The amount by which the correlation peaks are dilated is given by the transmitter PN frequency ratio with both PN sequences chip frequencies. Hence, when considering a transmitter PN sequence clocked at 500.1MHz and a receiver replica at 500MHz, we have a slide factor of 5001, therefore reducing the bandwidth requirement in the baseband data collection within the same order.

$$k = \frac{f_{seqTx}}{slip\ rate} = \frac{f_{seqTx}}{f_{seqTx} - f_{seqRx}} \tag{1}$$

According to [4], the transmitted PN places an upper bound on the radar maximum distance, proportional to the sequence length and the transmitted chirp period.

Fig. 4: MatLab app for FPGA reconfiguration.

Following this, the next chapter will discuss a reconfigurable real-time STDCC baseband capable of tuning both parameters on-the-fly.

III. RECONFIGURABLE RADAR ARCHITECTURE

The radar baseband is responsible for controlling and generating the radar signals to be transmitted, as well as linking these with those received. The proposed architecture, depicted in Fig. 3, uses a Xilinx Kintex 7 FPGA to change, on-the-fly, the utilised PN sequences and their output sampling frequency.

This architecture uses a soft-core microprocessor called microblaze (uB) responsible for routing the data inside FPGA to the required Xilinx blocks [8]. Such microprocessor receives the user parameters inserted in a MatLab GUI (Fig. 4) through a serial communication port (UART). Then, it routes the required control signals to custom made VHDL blocks called Axi2Counter and MemW32R1, which dictates the sequence length and its output sampling clock.

The all-digital sequence block design is depicted in Fig. 5 with greater detail. Such figure is a subset of Fig. 3 and it shows the control of two block memories that contain both the transmitted and receiver PN sequences.

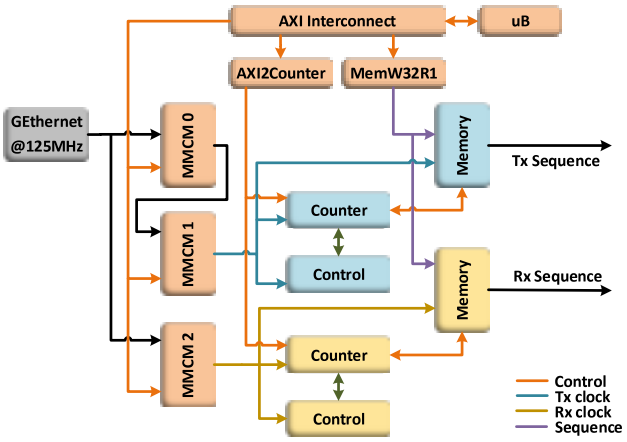

Fig. 5: Detailed overview of reconfigurable radar architecture.

Following the explained STDCC principle, the two PN sequences with a slight clock frequency offset are correlated in the analogue domain using a Mini-circuits ZFM-2-S+ mixer. The correlation mixer has a RF/LO range from 1 to 1000 MHz, necessary to output the correlation result which is in the order of few kHz. However, as stated in [4], the correlation operation performed by the mixer introduces high order intermodulation distortion (IMD). Thus, a low-pass filter is important to produce a clean time-dilated correlation product. Therefore, a 10th order low-pass filter (LPF) with a cut-off frequency at $2 \times sliprate$ was employed after the mixer and before the correlation acquisition.

In the end, a 12-bit 1 Mega sample per second ADC already present in the KC705 development board (XADC), acquires the correlation result for post-processing and plot within the same MatLab GUI.

A. Sequence generation

The proposed STDCC radar baseband uses PN sequences that are MLSR type (Maximal Length Linear Shift Register). The MLSR, also known as m-sequences, are a type of spreading sequences that present good auto-correlation properties. The m-sequence has an odd length of $N = 2^m - 1$ and a similar statistical distribution of ones and zeros (always has an extra value of one) and thus a constant power envelop.

The m-sequence generation is accomplished with a series of shift registers with feedback taps and modulo-2 adders. By varying the feedback taps according to the Table in [9], different sequences lengths are generated.

To increase the system flexibility and allow a future study of several sequence types (Gold, Kasami, Walsh, Zadoff-Chu), the sequence generation is performed in MatLab and downloaded to FPGA block memories. This work uses a 4-tap linear feedback shift register script that together with the tabular values given in [9] generates m-sequences of various lengths.

A microprocessor in FPGA (microblaze) is necessary for controlling the sequential memory write, as well as to process all the user selected STDCC parameters into FPGA native signals. Thus, the MatLab script groups the generated m-sequence into words of 32 bits to match the microblaze 32-bit architecture. Then, the MatLab app (Fig. 4) transmits them through serial communication (RS-232) to the FPGA microprocessor registers. After this, the sequence is routed via AXI protocol to the MemW32R1 custom-made VHDL IP block. Lastly, the MemW32R1 is responsible for decoding the AXI signals back into the original 32-bit sequence data while also generating the memory write address of the dual-port RAM storage.

A dual-port RAM is a memory type that allows multiple reads and writes to occur at the same time with different clock frequencies. That allows the sequence configuration to operate at microprocessor speed (memory write), while the sequence output can operate at the desired sampling frequency described in next Section (memory read).

The proposed architecture (Fig. 5) uses a reconfigurable counter to produce the read address for the dual-port RAM containing the sequence. Similar to the memory configuration, the counter control receives the sequence length value from the microblaze via a custom-made AXI2Counter block. This value will be compared against the last read address and will trigger the counter reset if memory length has been achieved. It should be noted that clock cross-domain techniques are required to intertwine the signals in the control block, since the sequence configuration operates at microprocessor clock (200 MHz) and sequence output operates at the desired sampling frequency (up to 500 MHz). In the end, we have two fully controlled dual-port RAM memories storing the two sequences that are each outputted in a KC705 SMA pin. Therefore, creating an all-digital m-sequence output with controlled sampling clock and without requiring an analogue converter board (DAC).

B. Sampling frequency algorithm

The possibility to tune the sequence output sampling frequency on-the-fly is another important characteristic envisioned for the reconfigurable STDCC baseband. By changing both the transmitter and receiver output frequencies, the user can vary the output bandwidth and the sliding factor, that, in the end, will adjust both the radar maximum detectable distance and speed.

The STDCC slip rate is usually within the hundreds of kHz, meaning that the difference between both transmitter and receiver sampling frequencies is quite small. To achieve such precise frequency values inside FPGA can be quite cumbersome using low-quality clock references. Hence, the proposed architecture uses a low-jitter 125 MHz clock chip present in the KC705 development kit, which is normally employed for gigabit ethernet (GbE) clock generation (ICS844021I) [10].

As can be seen in Fig. 5, such GEthernet clock is used by two clock generating blocks (MMCM) as input reference, that synthesise the transmitter and receiver sampling frequencies.

The Mixed-Mode Clock Manager (MMCM) are used within the Xilinx Vivado environment to implement a clocking network matched to the designer requirements. Such blocks were connected to the microprocessor via AXI bus to allow a

dynamic reconfiguration of their clocking primitives [11] and achieve the user's selected sequences sampling frequencies.

As stated in [12], each MMCM can synthesise up to 7 different frequencies with the following relationship:

$$CLK_{out_N} = CLK_{in} \times \frac{Mult}{Div \times Div_N} \ , \tag{2}$$

where N is the output number, CLK_{in} is the mentioned reference clock, $Mult$ is the MMCM fractional multiplication, Div is the MMCM integer division and Div_N the fractional multiplication for a given output clock.

Since the chosen KC705 development board has a Kintex7 FPGA with a -2 speed grade that has a VCO_{max} of 1440 MHz [13], the ideal $Mult$ value is given by:

$$Mult_{ideal} = \frac{Div_{min} \times VCOmax_{KC705}}{CLK_{in}} = 2.88 \ . \tag{3}$$

The MatLab script calculates the MMCM multiplication and division configuration parameters to best match the desired clock frequency. Considering the fractional operations step of 0.125 and respecting the given FPGA model limitations, the algorithm computes both Eqs. 4 and 5 to achieve the desired bandwidth and slip rate given its 125MHz input clock.

$$CLK_{Tx} = CLK_{in} \times \frac{Mult_{MMCM0}}{Div_{MMCM0} \times Div_{CLK0}} \times \times \frac{Mult_{MMCM1}}{Div_{MMCM1} \times Div_{CLK0}} \tag{4}$$

$$CLK_{Rx} = CLK_{in} \times \frac{Mult_{MMCM2}}{Div_{MMCM2} \times Div_{CLK0}} \tag{5}$$

It should be noted that both sampling frequencies are quite close, meaning that an architecture with a single clock generation block cannot synthesise a clock with few hundreds of kHz of precision. Thus, two MMCM (0 and 1) connected in cascade mode will operate together to fulfil the required sampling frequencies for the transmitter. For instance, to obtain the transmitter sampling frequency of 500.1 MHz, the MMCM0 outputs a clock of 33.866359 MHz that is converted to the desired 500.1 MHz by the MMCM1 (closest match of 500.100180 MHz).

With the reconfigurable architecture fully detailed, a set of performance evaluation indicators were taken that are discussed in next section.

IV. Experimental results and discussion

In this section, the proposed reconfigurable radar is assessed in terms of its resource usage efficiency. Then, the all-digitally generated sequences are evaluated according to their power spectrum and their autocorrelation properties in back-to-back (B2B) configuration mode (Figs. 6 and 7) will be discussed.

A. Hardware resources

The implementation of such architecture, besides reconfigurability, also aimed at the minimisation of hardware resource utilisation. Currently, in terms of memory usage, the design uses 4096-bit memories to allocate each sequence, while also providing space for processor data/instructions and for the temporarily XADC captured data. Despite all this, according to Table I, the Block RAM (BRAM) utilisation is still quite low ($< 7\%$), leaving room for future design increments if care is taken to keep the current timing constraints that achieve a 500 MHz output sequence.

On the other hand, in terms of clock resources for the microprocessor, DDR3, UART and reconfigurable clock architecture, 6 of the available 10 MMCMs are used. Looking at the remaining resource usage values, we can see a low utilisation of both Flip-Flops (FF) and Look up Table (LUT) of Kintex7 FPGA.

TABLE I: Reconfigurable architecture resource usage.

Resources	Utilisation	Available	Utilisation %
FF	22594	407600	5.54
LUT	24311	203800	11.93
BRAM	29.5	445	6.63
BUFG	13	32	40.62
MMCM	6	10	60.00

B. FPGA sequence output

The Agilent E4408B spectrum analyser was used to assess the all-digital sequence generation by measuring the channel power for various sequence lengths and sampling frequencies. For instance, Fig. 8 shows the frequency spectrum generated using a all-digital 9bit sequence with a sampling frequency of 500 MHz. The PN output spectrum depicted in Fig. 8 confirms the signal spectrum that follow a $\left(\frac{sin(x)}{x}\right)^2$ behaviour, with nulls occurring at multiple integers of the PN clock frequency, as expected [7].

Table II summarises the measured channel power, as well as, the power at f_s and $2\times f_s$ across multiple sequences (from 9 up to 12) and different sampling frequencies ($50, 250, 500$ MHz). Table II shows that the channel power stays relatively constant around 12.89 dBm/500MHz for different sequence lengths. However, by decreasing the sequences sampling frequencies a slight performance degradation appears.

C. Back-to-back performance

As can be seen in Fig. 9, two FPGA pins are responsible for outputting the sequences selected in MatLab App, requiring three input parameters that are the sequence length, Tx and Rx sampling frequencies. As mentioned, the Tx and Rx sequences have a slight frequency offset that performs the sliding correlation when connected to the RF and LO ports of the mixer. For simplicity purposes the result discussion will be for the I component only and with a fixed sliding factor of 100 kHz. The correlation result present at mixer's IF port

is connected to a LPF with a 200 kHz cut-off frequency and then captured by the FPGA XADC pins.

Figs. 6 and 7 show the STDCC baseband result, in B2B configuration, using a PN sequence length of 511 (m=9) and 1023 (m=10) respectively. In those figures, for each sequence length, the receiver sampling frequency was tuned to $[50, 250, 500]$ MHz that together with the fixed 100 kHz slip rate form a Tx=$[50.1, 250.1, 500.1]$ MHz. Table II compiles all the sequence lengths benchmarked with three sets of sample frequencies, showing the proposed reconfigurable STDCC radar performance (SNR).

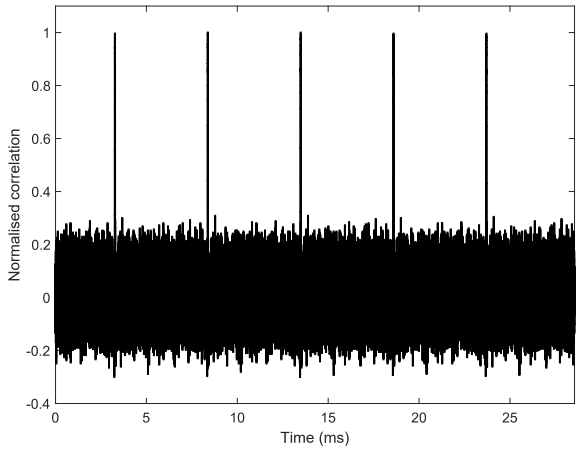

(a)

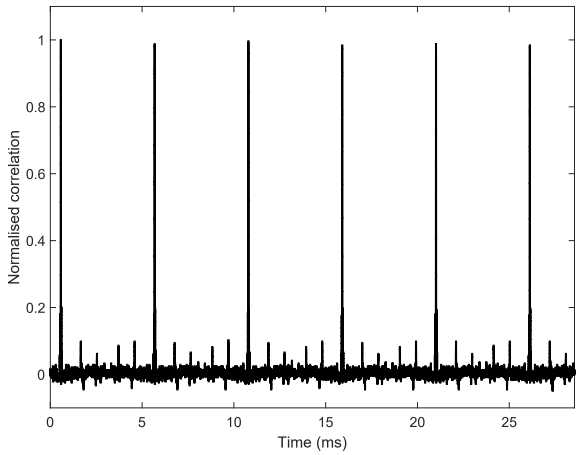

(b)

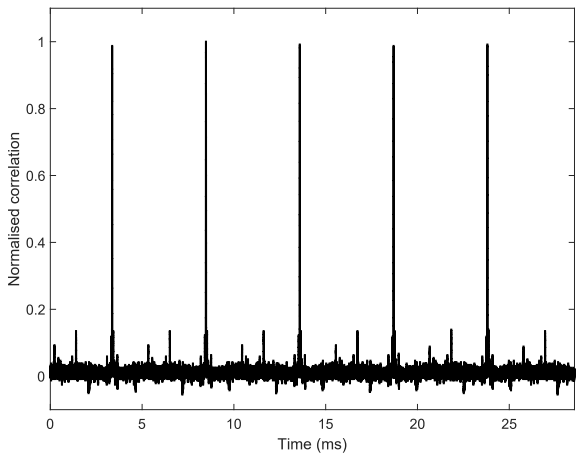

(c)

Fig. 6: Normalised captured CCF for an m-sequence, m = 9 with a) 50 b) 250 and c) 500 MHz output sampling frequency.

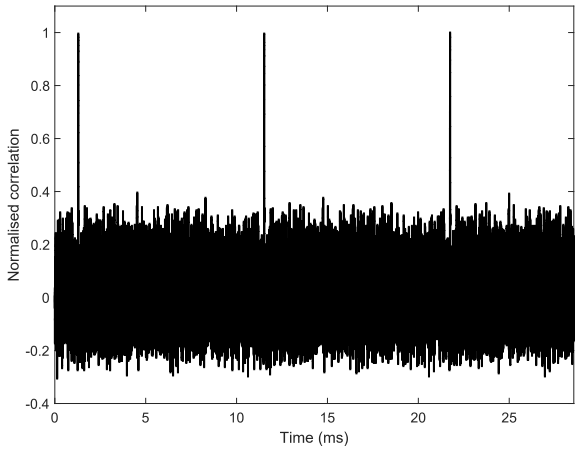

(a)

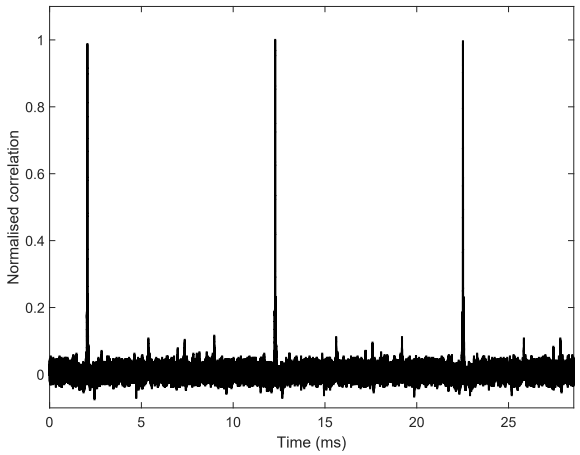

(b)

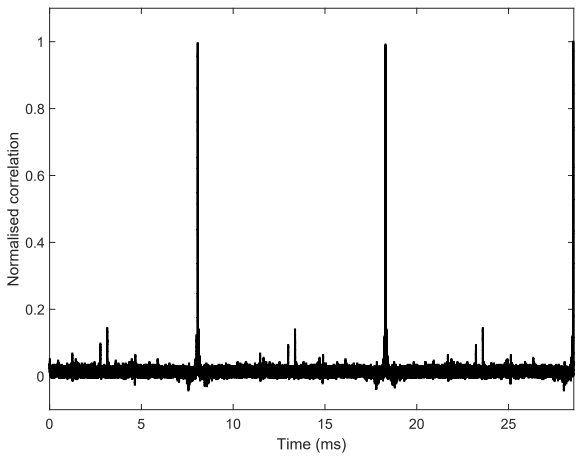

(c)

Fig. 7: Normalised captured CCF for an m-sequence, m = 10 with a) 50 b) 250 and c) 500 MHz output sampling frequency.

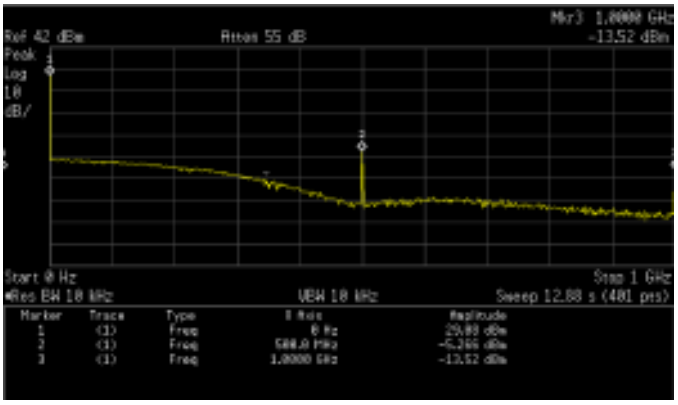

Fig. 8: Output spectrum of all-digital m=9 sequence.

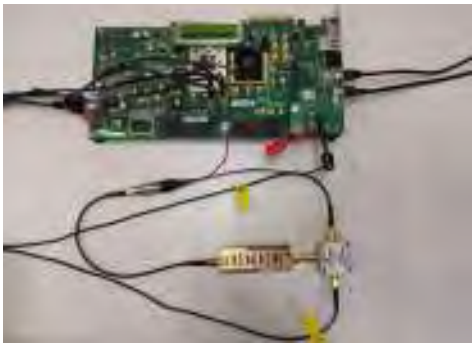

Fig. 9: KC705 FPGA with correlation and filtering.

The theoretical normalised auto-correlation result of a PN sequence, is represented by a triangular shape with apex set at value 1 and the base with a width of $N \times Tc$ set at $-1/N$ value, as can be seen in [5]. Thus, by increasing sequence length, the calculated SNR is expected to decrease since the noise floor will approximate zero value.

Looking at the measured correlation results presented in Table II, a strong relation between f_s/L and the SNR was observed, thus being closely associated with radar maximum detectable distance. It is shown that the normalised correlation peak to noise ratio (SNR) decreases with higher length sequences and lower output sampling frequencies (Table II), as expected.

V. Conclusions

This paper presented a reconfigurable architecture suitable for STDCC performance evaluation. The proposed architecture allows a on-the-fly sequence length tuning together with output sampling frequency adjustment. It has shown benefits with its all-digital architecture that does not require a DAC usage, and with its sliding correlation principle that requires a low-cost ADC acquisition board (XADC). Finally, this work shows a strong dependency between STDCC parameters and the radar detection performance. As expected, with shorter sequences and higher sequence sampling frequencies, the normalised correlation peak to noise ratio is increased, thus improving the radar maximum detectable distance.

TABLE II: Summary of the power measurements and SNR for various m-sequence lengths and sampling frequencies.

Measurement [dBm]	**Sequence (bits)**	**Sample frequency (f_s)**		
		50 MHz	**250 MHz**	**500 MHz**
Power @ f_s [dBm]	9	-24.68	-10.30	-6.48
	10	-24.71	-10.34	-6.59
	11	-24.75	-10.37	-6.62
	12	-24.82	-10.37	-6.67
Power @ $2 \times f_s$ [dBm]	9	-24.90	-13.28	-15.19
	10	-24.93	-13.32	-15.23
	11	-24.97	-13.35	-15.26
	12	-24.97	-13.35	-15.30
Channel Power [dBm/f_s]	9	13.45	13.17	12.89
	10	13.41	13.18	12.87
	11	13.40	13.15	12.85
	12	13.40	13.13	12.82
Normalised correlation peak to noise ratio (SNR)	9	0.531	0.794	0.834
	10	0.469	0.727	0.821
	11	0.457	0.723	0.816
	12	0.413	0.678	0.783

Acknowledgment

This work is partially funded by Research and Technological Development Incentive Scheme CO-PROMOTION - Centro2020 - P2020 - European Regional Development Funds, under project RADAVANT - Radar for Detection and Avoidance in Unmanned Aerial Vehicles (PI nr. 033907).

References

[1] A. C. J. Samarasekera, R. Feger, W. Scheiblhofer, and A. Stelzer, "Iterative minimum-entropy based algorithm for phase noise removal in fmcw radars," in *2019 16th European Radar Conference (EuRAD)*, Oct 2019, pp. 85–88.

[2] Y. Makino, T. Nozawa, M. Umehira, X. Wang, S. Takeda, and H. Kuroda, "Inter-radar interference analysis of fmcw radars with different chirp rates," *The Journal of Engineering*, vol. 2019, no. 19, pp. 5634–5638, 2019.

[3] R. G. M. Massaro, Davide; Ardoino, "An Efficient Processing Architecture for Range Profiling Using Noise Radar Technology," *MDPI aerospace*, 2018.

[4] R. J. Pirkl and G. D. Durgin, "Optimal Sliding Correlator Channel Sounder Design," *IEEE Transactions on Wireless Communications*, vol. 7, no. 9, pp. 3488–3497, Sep. 2008.

[5] D. Ferreira, R. F. S. Caldeirinha, and N. Leonor, "Real-time high-resolution radio frequency channel sounder based on the sliding correlation principle," *IET Microwaves, Antennas Propagation*, 2015.

[6] R. F. S. Caldeirinha, J. R. Reis, A. Sardo, L. Duarte, N. Leonor, J. Gil, and C. Ribeiro, "Disruptive future of radar based on all-digital pn signal processing," in *2019 IEEE-APS Topical Conference on Antennas and Propagation in Wireless Communications (APWC)*, Sep. 2019.

[7] C. R. Anderson, "Design and Implementation of an Ultrabroadband Millimeter-Wavelength Vector Sliding Correlator Channel Sounder and In-Building Multipath Measurements at 2.5 & 60 GHz," Master's thesis, Faculty of the Virginia Polytechnic Institute, 2002.

[8] UG940, "Vivado Design Suite Tutorial: Embedded Processor Hardware Design," Xilinx, Tech. Rep., Jun. 2019.

[9] R. Ward and T. Molteno, "Table of Linear Feedback Shift Registers," University of Otago, Tech. Rep., 2007.

[10] Renesas, "FemtoClock Crystal-to-LVDS Clock Generator (ICS844021-01)," Renesas, Tech. Rep., Aug. 2017.

[11] Jim Tatsukawa, "MMCM and PLL Dynamic Reconfiguration," Xilinx, Tech. Rep., Aug. 2019.

[12] PG605, "Clocking Wizard v5.1," Xilinx, Tech. Rep., Apr. 2015.

[13] "Calculation, Specification and settings for MMCM/PLL," Xilinx, Tech. Rep., Oct. 2018.